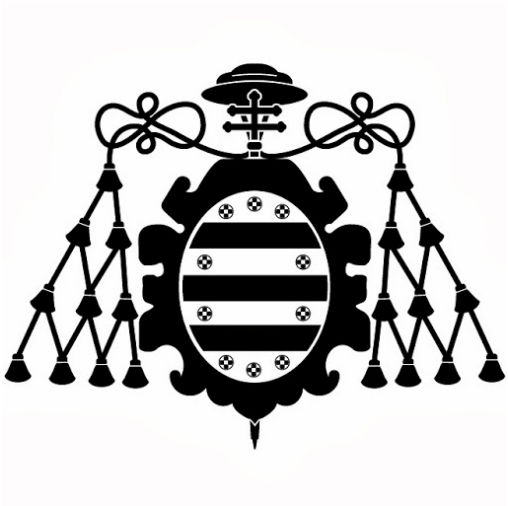

UNIVERSIDAD DE OVIEDO
Departamento de Física

Doctoral Thesis

Multipoles, Magnetic Charges and Chiral Properties in Antiferromagnetic Materials Inferred from Resonant X-Ray Diffraction

Ángel Rodríguez Fernández

2014

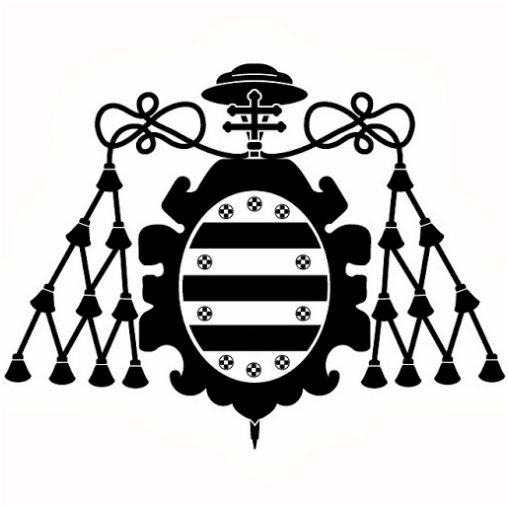

UNIVERSIDAD DE OVIEDO
Departamento de Física

Doctoral Thesis

Multipoles, Magnetic Charges and Chiral Properties in Antiferromagnetic Materials Inferred from Resonant X-Ray Diffraction

Ángel Rodríguez Fernández

2014

Acknowledgments

This thesis is the result of a long and hard work that started ten years ago when I first entered the Faculty of Science at the University of Oviedo. During this time, especially in the last four years of PhD, many people and institutions have helped me along this path. Therefore I would like to thank:

My supervisor Jesus A. Blanco Rodriguez who has been a father to me sharing his knowledge and wisdom, taking care of me not only in the work level but also in the day-to-day problems of my private life. He has always supported me to attend different conferences and schools, where I could improve my knowledge in Neutron and X-ray techniques.

My collaborator Dr. Kenneth D. Finkelstein, who spent much time discussing with me during my stages at Cornell University, teaching me all the physics under the reflectivity and diffraction processes. He also invited me to share with his family two wonderful Thanksgiving days for which I will always be grateful.

Stephen Lovesey, from whom I have learned all I know about the Resonant Elastic X-ray Scattering theory and who has also taught me to enjoy the great pleasures of the high cuisine and enjoying the best wine around the world together with his wife Margaret.

Steve, Gareth, Valerio, Dinesh, Helen and Jörg, who helped me to clarify my ideas during the long days at the synchrotron sources, Diamond Light Source and Petra III.

Camino, David, Eva, Laura Torre and Laura Roces that spent time trying to convert me in a Chemist showing me the synthesis and characterization of materials.

Pablo, Pedro, Mª Paz, Natalia, Marco, Jaime, Rebeca, Paola, Yusuke, Eoin, Alessandro, Jorge and Johannes whom have spend hours and hours suffering with me at the office.

Joel, Ernie, Don, Jacob, Katie, Kathy, Araceli, Zak, Matt, Margaret, David, Tabatha, Rohit, Howard, Eva, Tess and the rest of Cornell High Energy Synchrotron Source Staff who welcomed me with open arms during my stages.

My parents (Honorino and Mª Jose) and my brother (Daniel), for their patience that has always helped them to answer all my questions when I was a child and still continue to help them satisfy my huge curiosity. My grand-parents, Angel, Paulino, Maria Nelia del Carmen and Maria Fernanda Patrocinio who took care of me in my childhood. My uncles and aunts that taught me to love Nature (Mabel, Angel, Juan, Pedro and Nelia). My cousins (especially Ignacio, Mario, Irene and Raquel) and the rest of the members of my family.

Estela and Verónica that followed all my steps since the Kindergarten and who graduated with me in the promotion of 2009 of the "Licenciatura en Fisica" from the University of Oviedo.

To all the previously mentioned I want to wish a long and successful life.

Also to FICyT and the Principality of Asturias, which have funded my fellowship, the University of Oviedo, where the main part of my research was done, and the Spanish Education and Science Department for supporting the research projects in which I have participated. Also the Cornell High Energy Synchrotron Source for inviting me to carry out the two stages and the European Council for funding my experiments at Petra III and Diamond Light Source.

I am among those who think that science has great beauty. A scientist in his laboratory is not only a technician but also a child placed before natural phenomena which impress him like a fairy tale.

—**Marie Curie.**

A toda mi familia,
y en especial a aquel por el que llevo mi nombre.

ABSTRACT

In the last decades, the interesting features behind the exotic orderings of materials have attracted the attention of many scientists. This new physics can be related to the magnetic and charge multipoles defined by a few electrons around the atomic core in the valence states.

The uses of x-rays and neutrons techniques, due to the huge development of large facilities as synchrotrons and spallation sources, have revealed many of these behaviours. In the case of synchrotron sources, photon beams have high brightness, high tunability and good degree of polarization, which together with the development of new experimental techniques have been helpful in the characterization of new functional materials making valuable observations.

Resonant Elastic x-ray Scattering (REXS), in particular using polarization analysis, has shown to be an extremely sensitive tool for determining the charge and magnetic degrees of freedom of multiferroic, superconducting or other kind of strongly correlated materials; helping whereas other techniques such as neutron probes or non-resonant x-rays scattering are not able to obtain relevant information.

Conventionally, REXS experiments are performed at space group forbidden reflections, where high order contributions as Thomson scattering are not allowed. The data gathered at these weak Bragg reflections, due to space group symmetry rules, can be treated using an atomic model, which has the virtue of being used as a common platform for the analysis of x-ray and neutron diffraction experiments.

In this PhD work, three different antiferromagnetic materials with magnetic ions located in threefold symmetry (3) positions have been investigated in detail by means of REXS.

- Neptunium Dioxide (NpO_2), where an enigmatic low-temperature ordering state shows interesting physical features, similar to the one observed in UO_2, that relates its crystal field, the super-exchange interactions and electron–phonon coupling. Previous works from different groups have not been able to explain the resonant x-ray diffraction data collected at the neptunium M_4-edge. But new information, related to a change in the symmetry of the neptunium sites ($\bar{3}m$) due to the delocalization of the oxygen atoms, has helped to analyse and redefine the wave function that has successfully confirmed the reorganization of the oxygen sites and has estimated the value of hexadecapoles, which can not be observed by other techniques, confirming the antiferromagnetic ordering.

- Hematite (α-Fe_2O_3) in its antiferromagnetic phase and above the Morin temperature, due to an anisotropic exchange interaction that force the spins of the ions to assume a canted configuration, shows a small ferromagnetic contribution also known as Dzyaloshinskii-Moriya interaction. Previous studies performed to hematite using REXS near the iron K-edge did not explain properly the behaviour under this structure for both the collinear and canted antiferromagnetic phases. The application of the formalism presented in this work, which incorporate all magnetic contributions, successful explains the behaviour by the presence of a mixture between two processes electric-dipole (E1)-electric-quadrupole (E2) and E2E2, obtaining good estimated values for the different multipoles behind these processes. A circular polarized REXS experiment was modelled, which showed the possibility of distinguishing between these two processes while doing the experiment under this kind of polarization. The collected data ratifies the coupling between this kind of polarization and the chiral properties of the compound, showing a fully characterization of the high-temperature phase by the Magnetoelectric multipoles.

- Bismuth Ferrite ($BiFeO_3$), the only material from the multiferroic family that shows a magnetoelectric coupling above room temperature, is also an example of the Dzyaloshinskii-Moriya interaction. The results presented in this work supports a new chiral phase above the Néel temperature, in the ferroelectric phase, have been obtained by a REXS experiment, with the incoming x-ray beam tuned near the iron K-edge. The R3c forbidden reflection $(0,0,9)_H$ was studied as a function of the rotation of the crystal about the Bragg wave-vector in both phases, paramagnetic (700 K) and antiferromagnetic (300 K). The data gathered is consistent with a chiral structure formed by a circular cycloid propagating along $(1,1,0)_H$. Templeton and Templeton (T&T) scattering at 700 K is attributed in part to charge-like quadrupoles absent in a standard model of a cycloid in which a material vector generates all electronic states of the resonant ion. Extensive sets of azimuthal-angle data are used to infer values of three atomic multipoles in a satisfactory minimal model of the iron electronic structure, with a quadrupole (E1E1 event) and a hexadecapole (E2E2 event) contributing T&T scattering, plus a magnetic dipole (E1E1) for the antiferromagnetic phase.

RESUMEN

En las últimas décadas las interesantes características detrás de los órdenes exóticos de materiales han atraído la atención de muchos científicos. Esta nueva física puede ser relacionada con los multipolos eléctricos y magnéticos definidos por unos pocos electrones alrededor del núcleo atómico en los estados de valencia.

El uso de técnicas de rayos x y neutrones, debidas al gran desarrollo de grandes instalaciones como fuentes sincrotrones o espalación, han revelado muchas de estos comportamientos. En el caso de las fuentes sincrotrón, los haces de fotones han incrementado su brillo, tienen una capacidad de sintonización más alta y un buen grado de polarización, que junto con la mejora de las técnicas experimentales han sido de gran ayuda en la caracterización de los nuevos materiales.

La dispersión elástica resonante de rayos x (REXS, su sigla en inglés), en particular utilizando análisis de polarización, ha mostrado ser una herramienta de extremada sensibilidad para la determinación de los grados de libertad de carga y magnéticos en el caso de los materiales multiferroicos, superconductores u otros tipos de materiales fuertemente correlacionados; ayudando donde otras técnicas como las dispersiones mediante sondas de neutrones o rayos x no resonantes, no han podido proporcionar información relevante.

Convencionalmente, los experimentos REXS son realizados en reflexiones prohibidas por el espacio de grupo, donde las contribuciones de alto orden como la dispersión Thomson no están permitidas. Los datos experimentales obtenidos en estas reflexiones de Bragg débiles, debidas a las reglas de simetría de los

grupos de espacios, pueden ser tratados usando un modelo atómico, que tiene la virtud de poder explicar tanto los experimentos de difracción de rayos x como de neutrones.

En este trabajo de doctorado, se han estudiado tres materiales antiferromagnéticos en los que los iones magnéticos están localizados en posiciones de simetría trigonal (3) mediante el uso de REXS.

- El Dióxido de Neptunio (NpO_2), donde un estado de ordenamiento a baja temperatura presenta unas propiedades físicas interesantes, similares a los observados en UO_2, que relacionan su campo cristalino, la interacción de súper-cambio y el acoplamiento electrón-fonón. Previos trabajos de diferentes grupos no han sido capaces de rendir cuenta de los datos experimentales obtenidos mediante difracción resonante de rayos en el borde de absorción M_4 del neptunio. Pero nuevos información, relacionada con cambio en la simetría en las posiciones de los iones de neptunio ($\bar{3}m$) debidas a la deslocalización de los átomos de oxígeno, ha ayudado a analizar y redefinir la función de onda que ha confirmado la reorganización de los átomos de oxígeno, estimado los valores para los hexadecapolos no posibles mediante el uso de otras técnicas y confirmado el ordenamiento antiferromagnético.
- La hematita (α-Fe_2O_3) en su fase antiferromagnética y por encima de la temperatura de Morin, debido a una interacción de intercambio anisotrópico que fuerza a los espines de los iones a asumir una configuración canteada, presenta una pequeña contribución ferromagnética, también conocida como interacción Dzyaloshinskii-Moriya. Estudios previos realizados usando REXS cerca del borde de absorción K del hierro no explicaron adecuadamente el comportamiento detrás de esta estructura para las dos fases antiferromagnéticas, colinear y canteada. La aplicación del formalismo presentado en el que se incorporan todas las contribuciones magnéticas ha sido exitosa explicando el comportamiento con la presencia de una mezcla entre dos procesos dipolar-eléctrico (E1)-cuadripolar-eléctrico (E2) y E2E2, obteniendo buenos valores estimados para los diferentes valores de los multipolos detrás de estos procesos. Un experimento REXS con rayos x circularmente polarizada fue propuesto

para poner de manifiesto la posibilidad de distinguir entre los dos procesos cuando se realizaba el experimento bajo este tipo de polarización. Para confirmarlo, se recogieron datos experimentales que ratificaron el acoplamiento entre este tipo de polarización y las propiedades quirales del compuesto, mostrando una completa caracterización de la fase de alta temperatura mediante multipolos de tipo magnetoeléctricos.

- La ferrita de bismuto ($BiFeO_3$), único material de esta familia que presenta el acoplamiento magnetoeléctrico por encima de temperatura ambiente, es ejemplo también de la interacción Dzyaloshinskii-Moriya. La interpretación de medidas de REXS evidencia la presencia de una nueva fase quiral por encima de la temperatura de Néel, cerca del borde de absorción K del hierro. La reflexión prohibida del espacio de grupo R3c $(0,0,9)_H$ fue estudiada en función de la rotación del cristal alrededor del vector de onda de Bragg para dos fases, paramagnética (700 K) y antiferromagnética (300 K). Los datos obtenidos son consistentes con una estructura quiral formada por una cicloide circular propagándose a lo largo de la dirección $(1,1,0)_H$. Los barridos angulares acimutales de tipo Templeton and Templeton (T&T) a 700 K son atribuidos en parte a cargas de tipo cuadripolar no presentes en el modelo estándar de una cicloide en la que un vector material genera todas los estados electrónicos del ión resonante. Datos obtenidos de barridos acimutales extensos han sido utilizados para inferir los valores de tres multipolos atómicos en un modelo minimal satisfactorio de la estructura electrónica del hierro, con una contribución de tipo cuadripolar (proceso E1E1) y hexadecapolar (E2E2) a la dispersión T&T, junto con un dipolo magnético (E1E1) para la fase antiferromagnética.

Contents

Abstract ..... **i**

1. Introduction **1**

1.1. Overview 1

1.2. X-ray and its Production 3

1.3. Resonant X-ray Diffraction 5

1.4. Application to Materials 7

1.4.1. Motivation for the study of Neptunium Oxide, NpO_2 8

1.4.2. Motivation for the study of Hematite, α-Fe_2O_3 8

1.4.3. Motivation for the study of Bismuth Ferrite, $BiFeO_3$ 9

1.5. Organization and Structure 10

2. Theoretical Fundaments of Diffraction. **13**

2.1. Principles of scattering 13

2.1.1. Electron in an electromagnetic field 13

2.1.2. Diffraction by two electrons 14

2.1.3. Diffraction by an atom 18

2.1.4. Crystal structure 15

2.2. Non Resonant X-ray Diffraction (Thomson Diffraction) 18

2.3. Non Resonant Magnetic X-ray Diffraction 19

2.4. Resonant X-ray Diffraction 22

2.4.1. Resonant diffraction length 23

2.4.2. Even transitions under spatial inversion, E1-E1 & E2-E2 26

2.4.3. Odd transitions under spatial inversion, E1-E2 & E1-M1 29

2.4.4. Chiral structure 34

3. Resonant X-ray Scattering Experiments 37
3.1. REXS Beamlines 37
3.2. Azimuthal Scans 42
3.3. Polarization Analysis 45
3.4. Multiple Diffraction 46

4. Neptunium Oxide, NpO_2 51
4.1. Results & Summary 52
4.2. Article I 57

5. Hematite α-Fe_2O_3 69
5.1. Results & Summary 70
5.2. Article II 75
5.3. Article III 85

6. **Bismuth Ferrite, $BiFeO_3$** 95
6.1. Results & Summary 96
6.2. Article IV 103

7. Conclusions **113**

A Dzyaloshinskii-Moriya interaction **121**

B Parity-even Tensors, T_Q^K **125**

C Parity-odd Tensors, G_Q^K and U_Q^K **129**

D Principal Axes **133**

E Stokes Parameters **135**

F Cr_2O_3, Magnetoelectricity in R$\bar{3}$c Compounds **139**

G Intermediate States **143**

References **147**

CHAPTER 1

Introduction

1.1 Overview

Since the beginning of humanity our ancestors used the Sun as light source. The evolution of our specie has been always related to the discovery and govern of new irradiation sources as first happened with fire and later on with electricity (whose control opens to us the whole spectrum of radiation from the infrared to the x-rays regime, through the visible spectrum). These sources have been always behind the big steps in human evolution leading us to observe more deeply the universe and with this comprehension improve our quality of life by modelling the world around us.

One of these huge discoveries was performed by the German Nobel laureate in Physics, Wilhelm Conrad Röntgen. Who in November 1895 detected the first electromagnetic radiation with a wavelength in the range of the x-rays. After him, in 1912 Max von Laue performed an experiment that first showed how x-rays are diffracted by ordered materials, such as crystals, following his steps William and Lawrence Bragg in 1913 demonstrated that this diffraction can be used to determine the positions of the different atoms in the unit cell of a crystal. Since then, for over a century, thousands of scientists have been cooperating in the evolution and understanding of this type of radiation. The new world that has been opened to our eyes with the information available due to the different techniques based in x-rays, which have expand the knowledge in several scientific

fields; such as Biochemistry, Nano-technology, Drug development and other areas from the Material Science, among others.

Information provided by diffraction while doing crystallographic research is linked to the structure of the compound under study, which is related at all dimensions to the functionalities and properties of materials and molecules, being currently used even for the study of non-crystalline materials. This technique gives structural information at the molecular level across the different fields of science such as physics, biology, chemistry, mineralogy, archaeology and geology.

As an example, the chiral properties of an enantiomer material, i.e. materials which are non-superimposable mirror images of each other, can be related to the different degrees of freedom using Neumann's principle. The action of circular polarized x-rays, which present an electric field rotating along the beam giving chiral behaviour to this beam, can interact with the chiral properties of the different degrees of freedom in particular the spin giving information about the self-ordering of the material [1]. As shown in Figure 1.1, It is possible to differentiate between chiral structures as in the work presented by C. Zeng and co-workers [2], where two enantiomers of $Au_{28}(SPh\text{-}t\text{-}Bu)_{20}$ were characterized by circular dichroism spectroscopy.

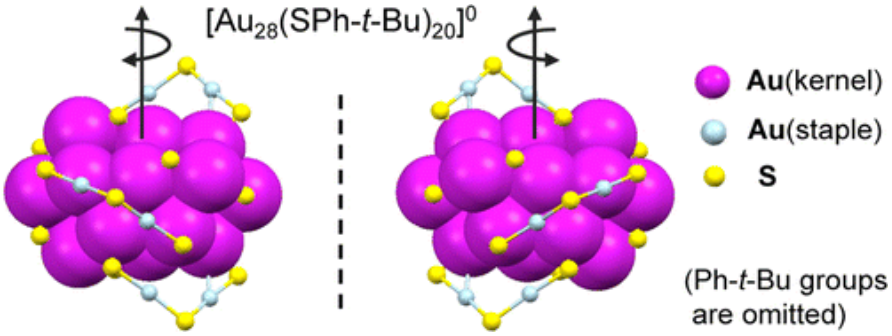

Figure 1.1 Representation of the two enantiomers of $Au_{28}(SPh\text{-}t\text{-}Bu)_{20}$ from the work presented by C. Zeng [2].

One of these crystallographic techniques is Resonant Elastic X-ray Scattering (REXS). This technique is resultant from the combination of the resonant process related to the electrons of each element specie and the process of dispersion of x-rays by the matter [3]. REXS was developed thanks to the high tunability and stability of the x-rays beams in large synchrotron facilities as Diamond Light Source (DLS, UK), PETRA III (Germany), European Synchrotron

Radiation Facility (ESRF, France), Advance Photon Source, (APS, USA) or Cornell High Energy Synchrotron Source, (CHESS, USA). These new sources not only provide a higher brightness (12 orders higher) than the conventional X-rays tubes, but also give a huge polarization control (due to the impressive evolution of the optics) and a high tunability of the energy beam [4], making possible the study of the high orbital degree of freedom of the electrons, i.e., studying the probability of an electron to occupy different degenerated orbitals of an ion.

This thesis describes a mathematical procedure that uses a model of localized electrons able to determine the shape of the orbitals by analysing the diffraction pattern of spatial order materials when studying the contribution from weak reflections due to group symmetry (space-group forbidden reflections). The weak signal being observed in these reflections is caused by the existence of spatial anisotropy in the charge distribution or by a large magnetic order that is not possible to describe by crystal space symmetry. The experimental procedure use in this type of analysis is known as Templeton-Templeton scans (T&T), azimuthal angle, ψ, scans performed keeping the Bragg condition fixed [5, 6]. This technique, also known as Anomalous X-ray Scattering, has played a significant role in the clarification of new properties in materials, as High-T_c superconductivity [7], colossal magnetoresistance [8], multiferroic properties [9, 10, 11, 12] or the well-known Mott gap compound, V_2O_3 [13]. These discoveries of new electronic properties of materials have increased the interest in atomic (charge, spin and orbital) degrees of freedom in systems of highly correlated electrons [14].

1.2 X-rays and its Production

As every electromagnetic wave, the x-rays are defined by its wavelength, λ. For the case of the X-rays this value is of the order of the interatomic distances, one Åmströng (10^{-10} m). The first x-ray detected by W. C. Röntgen use a Lenard tube (he was studying the radiations associated with discharge of electrodes along the vacuum inside this kind of glass tube) covered with an aluminium foil so no visible light was able to exit. This foil became an anode where x-rays were generated due to the Bremsstrahlung process (radiation pattern generated by de

acceleration/deceleration of a charge particle by the action of a electro-magnetic field) produced by the interaction between the electrons displacing along the tube and the field generated by the electronic cloud around the Al cores. Using a cardboard screen painted with barium plantinocyanide, he was able to observe the interaction of this radiation with matter (using different materials as paper, wood, metal and even his hand, which bones was able to photograph) for first time.

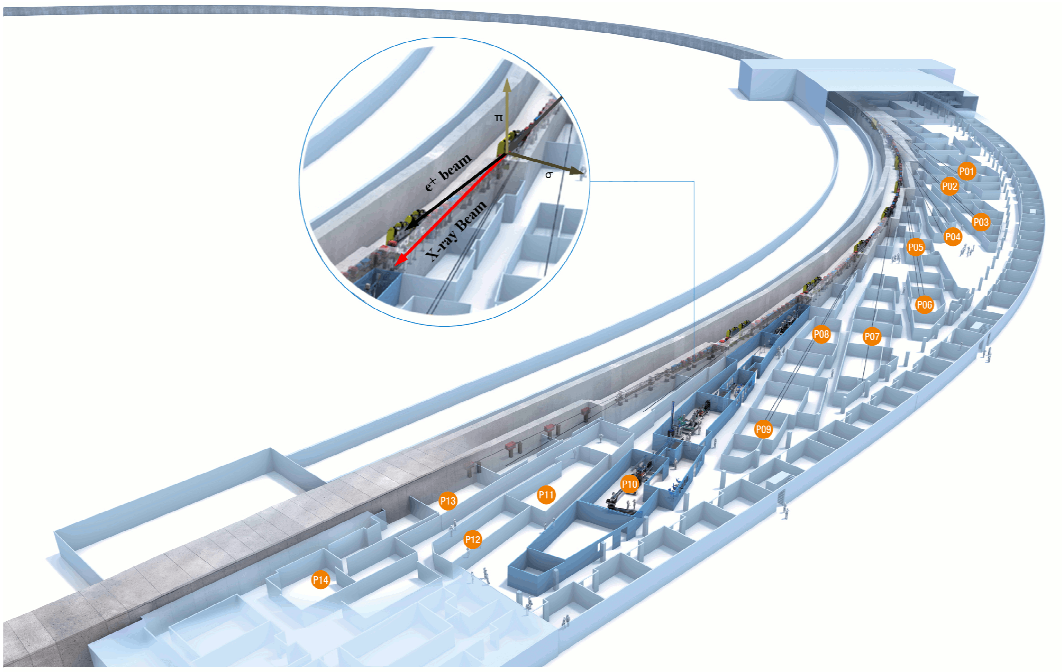

Figure 1.2 Scheme of the ring Petra III in Hamburg, showing the typical features of a third generation synchrotron radiation source.[1]

In 1912 W.D. Coolidge from General Electric developed the first x-ray commercial tube, which allowed the use of x-ray for commercial and research projects. But it was not until the middle 70s when the radiation coming from old accelerator for high energy physics, as CHESS or DESY, were used for the production of x-rays due to the Bremsstrahlung process, in this case, due to the application of a magnetic field that change the trajectory of the charge particle generating a deceleration and with it a radiation pattern that covers all the spectrum of light.

These first synchrotron sources were followed by the construction of other facilities specific for the production x-rays as the cases of DLS, the ESRF or APS, also known as third generation sources. This type of facilities present two main advantages with respect to the first generation ones; the beam has a lower

[1] Figure based in a image taken from http://photon-science.desy.de/facilities/petra_iii/beamlines/index_eng.html.

emittance (the particles are confined to a small distance and have nearly the same momentum), resulting an x-ray beam smaller that produces a higher brightness, and the incorporation of the so called insertion devices, long arrays of magnets that produce a stronger x-rays flux, making use of the straight sections.

The production of this kind of radiation has jumped many orders in terms of brightness from the $10^6 \frac{photons}{s\ mm^2 mr^2}$ of the Aluminium targets via $10^{20} \frac{photons}{s\ mm^2 mr^2}$ from third synchrotron generation sources (Figure 1.2) with undulators as insertion devices to the $10^{26} \frac{photons}{s\ mm^2 mr^2}$ expected for the European Free-Electron Lasers [16, 17].

1.3 Resonant X-ray Diffraction

For many years Neutron probes have been used as conventional techniques for determining the magnetic moment of different materials, in our days these values can be also measured using x-ray due to the interaction between this type of electromagnetic waves and the unpaired electrons that define the magnetic moment [18, 19]. The big disadvantage for the use of x-rays in contraposition to neutrons is related to the big ratio between the amplitude from the magnetic moments in comparison with the charge scattering (Thomson scattering), the magnetic moment contribution is due to a small number of unpaired electrons while in the case of the charge scattering all the electrons from the structure are contributing.

On the other hand, when studying reflections near an absorption edge, as done in the case of resonant x-ray diffraction experiments, the intensity will be amplified by the excitation of a core electron to an empty orbital in the valence state. This energy selection will only affect the elements with a resonance near to the one used, lowering the contribution to intensity of the ions from other elements in the case that the compound had more than one element in its structure (selective technique). Allowing the detection of the magnetic moments of a single element not possible to be done with other techniques such as neutron probes [20, 21]. This magnetic moment detection is performed by Templeton and Templeton

scans, rotation around the azimuthal angle, ψ, fixing the Bragg condition, which gives information about the electronic cloud of the ions under study.

For resonant x-ray diffraction experiments the definition of the wavelength of the x-rays is fixed by the energy of the absorption edge we are interested in working nearby. These atomic resonances are defined in relation to the core level quantum number n = 1, 2, 3, 4, 5 o 6; that are usually denoted by the letters K, L, M, N, O or P. And the spin-orbit dependence from the core level states, that is written using the total angular momentum $J = l \pm 1/2$, where l denotes the orbital angular momentum quantum number and ½ is related to the spin momentum, s. It is conventional in the community to denote the values of the J ($s_{1/2}$, $p_{1/2}$, $p_{3/2}$ and $d_{3/2}$) by numbers (1, 2, 3 and 4, respectively). The nomenclature used for denoting the absorption edges is then defined by a letter that correspond to the core level quantum number and a number coming from the total angular momentum, as an example, for Fe studies K_1 denotes $1s_{1/2}$ and Np studies M_4 denotes de core state $3d_{3/2}$.

In addition, resonant X-ray scattering allows us to perform polarization analysis studies both in the primary and secondary beams. The polarization of the beam from a synchrotron source, as previously note, is nearly σ polarized, but using some optical features it can be turned to be π-lineal polarized, or other kinds of polarization as elliptical or circular polarization. In our days, some insertion devices allow also the control of the beam polarization, due to a especial arrange of the magnetic poles along it, giving also the possibility of obtaining circular or elliptical polarization without optical gadgets along the experimental line.

Due to what has been describe in previous paragraphs, REXS is an appropriate technique for the determination of the orbital ordering of the valence electrons, this type of electrons are able to occupy different degenerates orbitals. Being able to give us information about the ordering of the different multipolar moments: dipoles, quadrupoles, octupoles, hexadecapoles,… when performing measurements of the intensity coming from forbidden reflections.

The formalism presented in this work calculates the amplitudes of the different contribution to diffraction for possible resonant processes in terms of a model of localized atoms based in irreducible spherical tensors. It is possible to

define these electronic transitions as parity-even, if the event do not break the spatial symmetry inside the system (dipolar-dipolar charge, E1E1, and quadrupolar-quadrupolar charge, E2E2), or parity-odd in the other case (dipolar charge-dipolar magnetic, E1M1, and dipolar-quadrupolar charge, E1E2). The structure factor, F, where is included the information of the variables that contribute to the intensity, is described as a sum in which one take into account all the ions that contribute to the interaction inside the unit cell together with a phase that relates to the symmetry between the different ions sites. F is always different from zero for space group allowed reflections, been its value equal to the sum of the phase factor if all the ions are identical. On the other hand, in the case of forbidden reflections the symmetry of the positions of the ions inside the unit cell cancels the intensities of the structure factor. For some of this forbidden reflections, and due to an ordering of the charge, magnetic or chiral moments of one of the elements inside the compound can be observed a small contribution to the intensity. Even this intensity is many orders smaller than an allow reflection, it can be well observed in the case of selecting an energy near to an absorption edge of this element specie under study where the amplitude is incremented due to a resonance process.

1.4 Application to Materials

In the recent past, the condensed matter physical community has been focused on the comprehension of the magnetoelectric, in particular the one present in multiferroic materials, which shows more than one ferroic ordering at the same phase. The interest in these materials rise from their possible implementation in the field of storage information, using them as future materials for spintronics, magnonics,… Bismuth Ferrite is an example of this type of compounds, well known because is the only multiferroic material that present both ferric ordering (ferroelectric and antiferromagnetic) above room temperature, the magnetoelectric effect present in this material is related to the Dzyaloshinskii-Moriya (DM) interaction, presented in Appendix A. The selection of the other two compounds studied, Neptunium Oxide and Hematite (Iron sesquioxide), during this work was done by the similitude that present this compounds with Bismuth Ferrite. Our

motivation was to show how REXS technique can infer information that relates the three materials, which show the same threefold symmetry around the location of the ions that contribute to magnetism.

1.4.1 Motivation for the study of Neptunium Oxide, NpO_2

The family of the actinide oxides, made up of An^{4+} and $2O^{2-}$, due to the 5f electrons from the actinide element, presents conventionally a magnetic ordering below a temperature, as the case of the UO_2 that present an antiferromagnetic behaviour below its Néel temperature ($T_N \approx 30$ K) [22]. Neptunium Dioxide, NpO_2, shows a phase transition at $T_0 = 25{,}5$ K that has not been possible to been explain as a magnetic transition by neutron probes or Mössbauer spectroscopy [23, 24], although appears to be a magnetic signal while performing muon probes experiments [25]. REXS experiments performed to this compound by Paixao et al. [26] use to explain the behaviour the fluorite fluorite structure ($Fm\bar{3}m$, #225) that in recent years due to NMR experiments has seen not to be the right one due to a change of the Oxygen positions to two non-equivalent positions [27], been the symmetry of the Neptunium sites reduced to a local (-3m) from the $Pn\bar{3}m$ (#224) space group. Nevertheless, the two space groups can be distinguished in a diffraction experiment exploiting Templeton–Templeton scans as presented in our work re-analysing the data presented by Paixao et al. [28]. The importance of understanding these materials is related to the interplay between crystal field, super-exchange interactions and electron–phonon coupling that seems to be the relation between its physical properties [29].

1.4.2 Motivation for the study of Hematite, α-Fe_2O_3

The next material under study was Hematite, α-Fe_2O_3. This compound well known to be the paradigm of the DM interaction since 1954 [30, 31] is a good touchstone for this kind of anisotropic exchange interaction due to the interest that presents this behaviour for new functional materials as multiferroics. The DM interaction forces a canted response from the moments of the spin from the

magnetic ions, producing the so called weak ferromagnetism in the case of antiferromagnetic materials as Hematite. Two groups investigated previously this compound using azimuthal dependent scans with linear polarized X-rays near the iron K-edge for different forbidden reflections from the $(0,0,l)_{\mathrm{H}}$ family with l odd [32, 33], we followed their work finding that the analysis of the data was not complete in the case of K. Finkelstein et al [33] and in the case of J. Kokubun et al [32] the approximation used to calculate the amplitudes of scattering were not the correct ones for energies below the edge. We reformulated the wavefunctions following a formalism based in irreducible spherical tensor, that is presented in chapter 2.4, which incorporates all magnetic contributions to Resonant X-ray Diffraction allowed by the established chemical and magnetic structures. In this point we show that there was an ambiguous contribution of the charge-dipolar charge-quadrupolar (E1E2) event together with the pure charge-quadrupolar (E2E2) event, that were possible to be distinguish in the case of using circular polarized x-rays in the primary beam, which motivated our experimental findings in this material as explained in Chapter 5. The comprehension of the chiral structure of the moments of this compound can help in the better understanding of the behaviour shown by the magnetoelectric materials.

1.4.3 Motivation for the study of Bismuth Ferrite, $BiFeO_3$

Bismuth Ferrite is known to be the only multiferroic material which present both ferric phases (ferroelectricity and antiferromagnetism) above room temperature, giving to this material key properties for the application of this kind of materials in future devices [34, 35, 36, 37]. $BiFeO_3$ presents a polarization of $100\ \mu_C/cm^2$ under its Curie temperature ($T_C \approx 1100\ K$), this ferroelectric property coexist below the Néel temperature with a G-type antiferromagnetic ordering $(+-+-)$ together, in the case of bulk material, with a long-period incommensurate magnetic cycloid modulation ($\approx$ 620 Å). The spiral propagates along the vector $(1,1,0)_H$ with the dipole moments rotate in the $(\bar{1},1,0)_H$ plane, defined by the spontaneous electric polarization along $[0,0,1]_H$ and the propagation vector [12]. This interest motivated us to try to synthesis a good quality crystal to study and doped it with other elements that could give interesting properties as the elements

from the lanthanide family, as Gadolinium, which perovskites also present multiferroic behaviour. The use of REXS experiments in this type of chiral structure can reveal the interest of the orbital moments around the bismuth and iron sites which can help in the future designing of new multiferroic materials.

1.5 Organization and Structure

This thesis work is presented on the modality of a compendium of articles already published in scientific journals. In Table 1.1is presented relevant information related to the journals where the articles have been published: year of publications, impact factor and the relevance of the journal on the area(s) where it is ascribed.

The thesis is structured into seven chapters. *Chapter 1* was comprised to a general introduction to the subject of x-ray and with the Resonant Elastic X-ray Scattering, together with the motivation of the different material investigated along this PhD Thesis. In *Chapter 2 presents* the theoretical background for scattering and the formalism based in non-reducible tensor used to describe the processes of scattering is presented. *Chapter 3* is devoted to x-ray synchrotron facilities and the experimental fundaments of the technique that has been used, REXS. The following chapters (*Chapters 4*, *5* and *6*) present the results obtained from the investigation performed to the three antiferromagnetic compounds. To conclude with the final remarks presented in *Chapter 7*.

Table 1.1. Details of the scientific journals where the articles have been published (or submitted) in this PhD Thesis. Information has been taken from the web site ISI Web of Knowledge/ Journal Citation Reports 2012 JCR Science Edition.

Journal	**Year**	**Impact Index**	**Area**	**Nº/area (percentile)**
Phys. Rev. B	2011	3.691	Physics, Condensed Matter	13/69 (Q1)
	2013	3.767	Physics, Condensed Matter	15/68 (Q1)
J. Phys.: Condens. Mat.	2012	2.355	Physics, Condensed Matter	20/68 (Q2)
J. Phys. Soc. Jpn.	2014	2.087	Physics, Multidisciplinary	19/83 (Q1)

CHAPTER 2

Theoretical Fundaments

2.1 Principles of Scattering

From a basic point of view, we can consider X-ray scattering by charge particles as the generation process of an electromagnetic wave by a series of charge particles oscillating in phase due to the action of an electromagnetic field produced by an incoming X-ray wave. This process can be divided in elastic (diffraction) if the energy of the scattered photon is conserved with respect to the photon which excited the particles or inelastic (Compton) if the final energy of the photon scattered is changed, for example, due to an absorption process.

2.1.1 Electron in an electromagnetic field

Let's first consider the interaction between an electromagnetic wave and a free electron. The total energy of a non-relativistic free particle (in our case an electron), in the absence of externals fields, is its kinetic energy, $\varkappa = p^2/2m_e$, where p is the momentum of the particle and m_e the mass of the electron.

If the electron interacts with an electromagnetic field generated by the incident wave, $E_0 e^{i(q\cdot r-\omega t)}$, where q is the incoming wave vector and ω its frequency, the momentum of the electron is change to be $p - \frac{e}{c}A$, denoting A as the vector potential [38]. The energy of the particle will be then

$$\varkappa = \frac{\left[p-\frac{e}{c}A\right]^2}{2m_e} = \frac{p^2}{2m_e} + \frac{e^2}{2m_e c^2}A^2 - \frac{e}{2m_e c}\boldsymbol{p}\cdot\boldsymbol{A}, \qquad (2.1)$$

here, p and A denote two quantum operators that we have assumed to commute. These two terms related to vector potential describe the interaction between the electromagnetic field and the electron. In terms of quantum mechanics, the potential operator vector, $\boldsymbol{A}$, can be described in terms of the creation and annihilation operators and due to this is the one that has the property of creating and destroying the photons.

The first order of perturbation is related to the term A^2, this term is able to create and destroy a photon in one interaction and due to this is the most important contribution for photon scattering (Thomson Scattering). The second term $p \cdot A$ (second order of perturbation) is only linear in the photon operators so it can destroy or create a photon but not both, been related to photon absorption (destruction) and photon emission (creation) causing also a scattering that will need two interactions. One example is the case of resonant or anomalous scattering, when the photon energy matches an excitation in the target and the denominator becomes very small.

The interaction with the magnetic field is done with the spin of the electron been $\varkappa' = -\mu \cdot H$ the energy, where we can define μ as the magnetic moment equal to $-2\,\mu_B S$, where S denotes de spin of the electron and μ_B the Bohr magneton ($e\hbar/2m_e$) . The Magnetic field can be described in terms of the vector potential as $H = \nabla \times A$, this term, known as Zeeman term, is in the same order of perturbation as $p \cdot A$. But it is not the only contribution of the magnetism, also the effect between the spin and the magnetic field generated by the electron itself due to the classical Ampére's law (charge particle moving inside a electric field) must be taking into account inside the magnetic contribution, so in addition we have to include the spin-orbit interaction $S \cdot (A \times E)$.

2.1.2 Diffraction by two electrons

The scattering process needs of unless two particles to happen [17]. For this reason, let's consider the case of the interaction between two electrons inside an electromagnetic wave. Let's first denote G as the difference between the incoming, q, and scatter, q', wave vector as shown in Figure 2.1,

$$G = q - q'. \tag{2.2}$$

The scattering power is usually defined in terms of the Thomson scattering length also known as the classical radius of the electron, $r_e = e^2/mc^2\ (c.g.s) = 2.82\ 10^{-5}$Å. The scattering amplitude can be writing as

$$F(G) = -r_e\left(1 + e^{iG\cdot r}\right). \tag{2.3}$$

where term $G \cdot r$ defines the phase difference between the interaction of the two electrons in relation to the electromagnetic field, describing $F(G)$ the possibility of finding a constructive signal. The intensity for this two particle system is proportional to the square of the absolute value of the amplitude,

$$I \sim |F|^2. \tag{2.4}$$

2.1.3 Diffraction by an atom

For the case of an atom the electromagnetic fields will exert forces on the electrons of the atom producing accelerations, vibration affects, in the entire valence electrons around the core, which can be described by a charge density of the valence electrons, $\rho(r)$. This changes the scattering radiation field to be a superposition of all the contributions from the different volume elements in this distribution [38]. To evaluate this scattering amplitude we must take into account the contribution of the electrons around the atom by summing over all the space, this integration define the atomic form factor $\langle \sum_j e^{iG\cdot R_j} \rangle$, that is equal to the number of electrons in the case of G = 0. The exponential inside the brackets is given by

$$e^{iG\cdot R_j} = 4\pi \sum_{KQ} i^K j_K\left(GR_j\right)\left\{Y_Q^K\left(\hat{G}\right)\right\}^* Y_Q^K\left(\hat{R}_j\right), \tag{2.5}$$

here, $\hat{G} = \mathbf{G}/\mathrm{G}$ and $\hat{R}_j = \boldsymbol{R_j}/R_j$ are the unit vectors, $j_K\left(GR_j\right)$ is a spherical Bessel function of rank K multiply by the radial density of valence function, $\rho(r)$, and $Y_Q^K\left(\hat{k}\right)$ are spherical harmonics with K its rank and Q the projection that satisfy that $K \geq Q \geq -K$ and can take $2K + 1$ values.

Now, it is interesting to introduce the atomic tensor $\langle T_Q^K \rangle$, in function of the spherical harmonics. The definition of these tensors is related to the separation of the angular dependence of G and R_j in (2.5), extra explanation is given in Appendix B.

$$\langle \sum_j e^{iG\cdot R_j} \rangle = (4\pi)^{1/2} \sum_{KQ} i^K \langle j_K \rangle (-1)^Q Y_{-Q}^K(\hat{G}) \langle T_Q^K \rangle, \qquad (2.6)$$

where ($\langle \ldots \rangle$) defines the time-average value. The term $\langle j_K(G) \rangle$ for the case that $G = 0$ and for $K > 0$ is equal to 0.

$$\langle T_Q^K \rangle = (4\pi)^{1/2} \sum_j \langle Y_Q^K(\hat{R}_j) \rangle \qquad (2.7)$$

The atomic tensor $\langle T_Q^K \rangle$ evaluated for $K = Q = 0$ is equal to the number of valence electrons. The atomic tensors are also called multipole moments and they are named by the Greek word for the number 2^K, as present in Table 2.1.

Table 2.1 Multipole moments.

Rank	Greek Name
K = 1	Dipole
K = 2	Quadrupole
K = 3	Octupole
K = 4	Hexadecapole
K = 5	Triakontadipole
K = 6	Hexacontatetrapole

2.1.4 Crystal Structure

Let's define a crystal as a solid where all the atoms occupy fixed position inside a periodic structure with translational symmetry. The smallest fraction of crystal where can be defined all the symmetry is known as unit cell. All the possible crystalline structures for 3D were classified by Aguste Bravais in 14 lattices; these lattices together with the symmetries of the different sites that can occupy the atoms inside the unit cell define the 230 space groups, tabulated in the international tables of crystallography [39].

The unit cell can be described by the lattice vectors, also known as cell parameters (a, b, c), and a motif. The position of any atom inside the crystal can be defined giving the distance to the origin of the cell, as $R_n = x_1 a + x_2 b + x_3 c$, where $n_{i=1,2,3}$ are integers values.

$$G = \tau(hkl) \tag{2.8}$$

The condition of diffraction or Laue condition (2.8), see Figure 2.1(b), inside a crystal is defined as a constructive signal result of the different atoms that satisfy the same interaction with the incident X-ray radiation. $\tau(\mathrm{hkl}) = \mathrm{ha}^* + \mathrm{hb}^* + \mathrm{lc}^*$ describes the group of planes that satisfy the same condition, where (a^*, b^*, c^*) is base of the reciprocal space, that is derivate from the base of vectors from the real space as (2.9), where (h, k, l) are a series of integers known as the Miller indices,

$$a^* = \frac{2\pi(b\times c)}{V_c},\ b^* = \frac{2\pi(c\times a)}{V_c} \text{ and } c^* = \frac{2\pi(a\times b)}{V_c}, \tag{2.9}$$

here, V_c is the volume of the unit cell. The Laue condition of diffraction can also be described by the use of the Ewald sphere, presented in Figure 2.1(b), when two atoms fall in the sphere of radius q the conditions for scattering are satisfied.

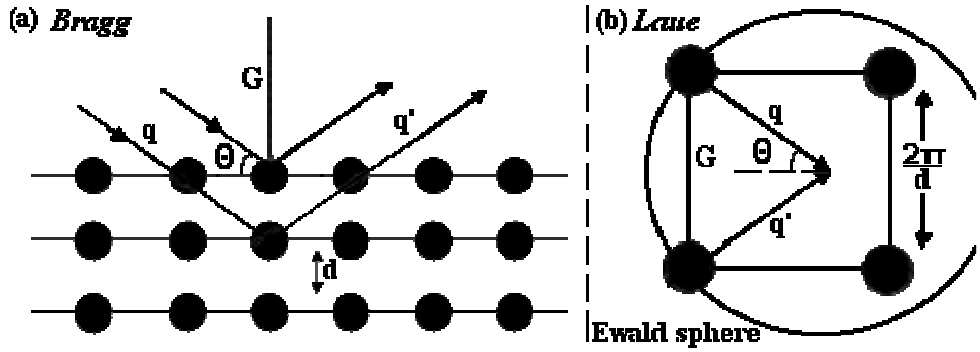

Figure 2.1 Equivalence between Laue and Bragg conditions of X-ray diffraction by a 2D lattice.

The Miller indices are used to label the possible reflections of the system [17]. Usually use to describe the allow reflections due to space symmetry rules, they are also employed to define the weak reflections that may arise due ions in environments in the unit cell not equivalent on account of a lack of translational symmetry. We can now define the distance between the planes that satisfy the same diffraction conditions, d_{hkl}, or lattice spacing as,

$$d_{hkl} = \frac{1}{\sqrt{\left(\frac{h}{a}\right)^2 + \left(\frac{k}{b}\right)^2 + \left(\frac{l}{c}\right)^2}}. \tag{2.10}$$

Ones defined d_{hkl} it is possible to present the Bragg condition to scattering, Figure 2.1(a), that relates the angle of incident of the beam with the lattice spacing and the wavelength of the electromagnetic wave, as

$$n\lambda = 2d_{hkl}sin(\theta), \qquad (2.11)$$

where n is a integer. This condition is equivalent by an easy demonstration to the Laue condition presented in (2.8).

2.2 Non Resonant X-ray Diffraction from Crystal (Thomson Diffraction)

Conventionally, while defining the interaction between radiation and matter using quantum-electrodynamics, the X-ray scattering length is developed in terms of $\gamma = E/m_e c^2$. The first order of this approximation is related to the spatial Fourier transform of the electron charge density and it is responsible for the Thomson scattering of X-rays, $F_c(G)$ [40, 41], the second approximation term $\mathrm{f_{mag}}(G)$ is related to the process of interaction between the spin of the electrons and the electromagnetic wave, while the third term of the approximation is a complex correction known as resonant or anomalous dispersion term, $\Delta f = f' + if''$

$$F(G,\omega) = F_c(G) + f_{mag}(G) + f'(\omega) + if''(\omega). \qquad (2.12)$$

The Thomson contribution to the X-ray scattering length (Figure 2.2) by a crystal is expressed as $-r_e(\varepsilon \cdot \varepsilon')F_c(G)$, where ε and ε' denote the polarization of the incoming and outgoing beam and they are perpendicular to the wave vector of the beam ($q \cdot \varepsilon = q' \cdot \varepsilon' = 0$). $F_c(G)$ is sum over every ion in the unit cell that contributes to scattering as expressed in (2.13), the subscript c is used to denote that for the moment we are just taking into account the charge density contribution.

$$F_c(G) = \sum_d e^{iG\cdot d} \langle \sum_j e^{iG\cdot R_j} \rangle_d, \qquad (2.13)$$

here, we find the atomic form factor for the electrons associated with the ion occupying the d site. The second exponential relates the different positions inside the unit cell. Inserting the value of the form factor we can write the Thomson contribution in terms of the atomic multipolar moments as

$$F_c(G) = \sum_d e^{iG\cdot d} (4\pi)^{1/2} \sum_{KQ} i^K \langle j_K \rangle (-1)^Q Y^K_{-Q}\left(\hat{G}\right) \langle T^K_Q \rangle_d. \qquad (2.14)$$

Note that $F_c(G)$ is a scalar product of a spherical harmonic related to the X-ray and a tensor associated with the electronic cloud around the ions in the d site. Grouping the terms that depend of the site d we can define the cell structure factor, Ψ_Q^K, that will take into account all the symmetry inside the unit cell.

$$\Psi_Q^K = \sum_d e^{iG\cdot d} \langle T_Q^K \rangle_d \qquad (2.15)$$

The atomic tensors encountered in Thomson scattering change to $(-1)^K\langle T_Q^K\rangle_c$ from $\langle T_Q^K\rangle_c$ under inversion of the coordinate system of the electrons, which is also referred to as the parity transformation, and a tensor with this transformation property is called a true (or polar) tensor. If the parity transformation introduces a phase factor $(-1)^{K+1}$ the tensor in question is called a pseudotensor, or an axial tensor, an example of this is the helicity of an X-ray beam.

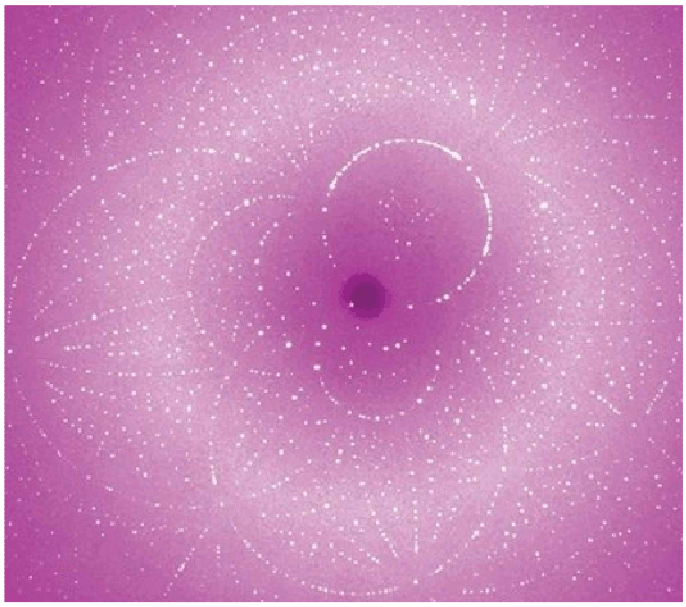

Figure 2.2 Laue diffraction pattern from the photo-active yellow protein. Image taken from J. Als-Nielsen & D. McMorrow [17].

2.3 Non Resonant Magnetic X-ray Diffraction

One of the differences between neutron and X-ray scattering is related to the difference in the spin-orbit interaction. While neutrons are scattered by the magnetization in a material which is created by the spin and orbital moments of unpaired electrons giving a contribution of the spin angular momentum (S) and

the orbital momentum (L) proportional to the value L+2S [18, 42]. In the case of X-ray these two values are not coupled and can be measured separately, using techniques for spin definition as Magnetic Compton X-ray Scattering [43, 44, 45]. Even the spin interaction for neutron scattering is very similar to the spin interaction in X-ray scattering; there is one difference between the two cases related to the dependence of neutron scattering with the deflection of the beam in a double vector product $\boldsymbol{k} \times (s_j \times \boldsymbol{k})/k^2$.

The introduction of the spin from the electrons gives the first term approximation to scattering,

$$F(G) = -r_e[(\varepsilon \cdot \varepsilon')F_c(G) - i\tau F_S(G) \cdot B], \qquad (2.16)$$

where the spin contribution depends of the reciprocal lattice vector, $\tau = \hbar q/mc$, and the scattering wave vector G. The first term in (2.16) is the familiar charge scattering length, while the second is sensitive only to the electron spin orientation due to the product with B,

$$B = (\varepsilon' \times \varepsilon) - (\hat{q}' \times \varepsilon') \times (\hat{q} \times \varepsilon) + (\hat{q}' \cdot \varepsilon)(\hat{q}' \times \varepsilon') - (\hat{q} \cdot \varepsilon')(\hat{q} \times \varepsilon). \qquad (2.17)$$

The most important differences between the spin scattering and the Thomson scattering are the following:

- The spin scattering amplitude is reduced by a factor τ compared with the charge scattering.
- The charge and spin scattering amplitudes for a plane polarized primary beam are 90º out of phase.
- Spin scattering causes a partial rotation of the plane of polarization unlike charge scattering.
- The spin scattering amplitude scales with the net spin polarization, ⟨S⟩, which is general small, even in magnetic systems.

The rather complicated polarization dependence of magnetic scattering is a very valuable property. Apart from being essential for the circular polarization induced interference scattering, the fact that charge scattering does not cause polarization mixing allows the possibility of constructing a sensitive filter for magnetic diffraction. A quantitative analysis of the secondary beam polarization

can give important information about the spin and orbital composition of the magnetization density.

The spin density structure factor, $F_S(G)$, is a vector quantity, which describes both the configuration and the orientation of the spin moments in a unit cell [38]. This factor is well represented by a sum of individual contributions from each ion in the magnetic cell,

$$F_S(G) \simeq \sum_d f_s(G;d)\langle S\rangle_d \, e^{iG\cdot d}, \qquad (2.18)$$

where the term $f_s(G;d)$ denote the atomic spin form factor, that in the case of $G = 0$ is equal to 1. Similar to the Thomson contribution we can define this atomic spin form factor as

$$f_s(G;d)\langle S\rangle_d = \langle \sum_j e^{iG\cdot R_j} s_j \rangle_d \qquad (2.19)$$

here, the subscript j is related to the j_{th} electron associated with the ion in the position d of the unit cell. The calculation of these expected values in terms of the spherical harmonics is done in Appendix B.

The absence of an orbital term in the photon amplitude reflects the fact that we have so far considered scattering from free, stationary electrons. This is not true, because the electrons are in perpetual motion around the atomic nuclei, although the fact that most electrons form pairs of time-reversed orbits means that the net momentum distribution is often very small and may be neglected. In magnetic systems, time-reversal symmetry is broken, and may exist regions where the electrons possess a finite net momentum. The scattering amplitude from these regions becomes slightly modified by the electron motion, and this is the origin of the orbital scattering.

$$F_L(G) \simeq \tfrac{1}{2}\sum_d f_L(G;d)\langle L\rangle_d \, e^{iG\cdot d}, \qquad (2.20)$$

where the atomic orbital form factor is,

$$f_L(G;d)\langle L\rangle_d = \langle \tfrac{1}{(iG^2)} \sum_j e^{iG\cdot R_j}\big(G \times p_j\big)\rangle_d. \qquad (2.21)$$

Leading to a final expression for the magnetic first order approximation $f_{mag}(G)$

$$f_{mag}(G) = -i\tau[\mathrm{F_S}(G)\cdot \mathrm{B} + F_L(G)\cdot \mathrm{B_0}]$$

where $\mathrm{B_0}$is defined as

$$B_0 = (\varepsilon' \times \varepsilon) - \widehat{\boldsymbol{G}}\big[\widehat{\boldsymbol{G}}\cdot(\varepsilon' \times \varepsilon)\big]. \qquad (2.22)$$

Using the definition of the spherical tensors $\langle T_{\mathrm{Q}}^{\mathrm{K}}\rangle$ we can write the cell structure factor

$$\Psi_Q^K(S) = \sum_d e^{iG\cdot d}\langle T_Q^K\rangle_{S,d}, \qquad (2.23)$$

$$\Psi_Q^K(L) = \sum_d e^{iG\cdot d}\langle T_Q^K\rangle_{L,d}, \qquad (2.24)$$

and the amplitudes of scattering as,

$$F_S(G) = \sum_{KQ}\sum_{K'Q'}(4\pi)^{\frac{1}{2}} Y_Q^K(\hat{G})\Psi_{Q'}^{K'}(S)(KQK'Q'|1p), \qquad (2.25)$$

$$F_L(G) = \sum_{Q}\sum_{KQ}(4\pi)^{\frac{1}{2}} Y_Q^{K'-1}(\hat{G})\Psi_{Q'}^{K'}(L)(K'-1QK'Q'|1p). \qquad (2.26)$$

The reduced matrix elements are defined in the appendix B For the calculation of the structure cell factor, $\Psi_{Q'}^{K'}$, the tensors at different sites in the cell are related by the application of the symmetry operators in the space group. To take into account the magnetism it is necessary to introduce the influence caused by reversing the polarity of the local magnetic field apart of the conventional rules related to the symmetries described by the magneticspace group. For example, a fully compensating antiferromagnetic has equal numbers of ions with opposite local fields. The general rule for parity-even tensors is,

$$\langle T_Q^K\rangle_H = (-1)^K\langle T_Q^K\rangle_{-H} \qquad (2.27)$$

here, H denotes an applied field on the direction of the spontaneous moment at the site in question. These general expressions for the magnetic structure factors can include higher–order multipole moments tensors as octupoles.

2.4 Resonant X-ray Diffraction

The next contribution to the scattering intensity, following the approximation in terms of E/m_ec^2, is related to the resonant behaviour that is only relevant in the approximation to a shell absorption edge of the material under study. It was in

1985 when Nanikawa et al. [46] found a small contribution to the magnetic scattering from a ferromagnetic nickel at energies very close to the K-edge. Three years later Gibbs et al. [47] found a resonance-enhancement magnetic diffraction from an antiferromagnet while measuring a holmium sample near the L_3-edge, giving the first clear demonstration that resonant scattering could make magnetic diffraction experiment considerable easier to be performed.

Differently to both non-resonant scattering and neutron diffraction in the case of resonant magnetic scattering does not give direct information about magnetization densities. Resonant diffraction is essentially a probe of local magnetic phenomena, as happens with dichroism, since the excitation involve a highly localized initial core state. This is due to the fact that resonant scattering needs to take place in regions of high core level density, regions close to the nucleus. One of the most important advantages of resonant magnetic scattering is high sensitivity to the directions of the local moments, and from this can be determined the magnetic orbital structure.

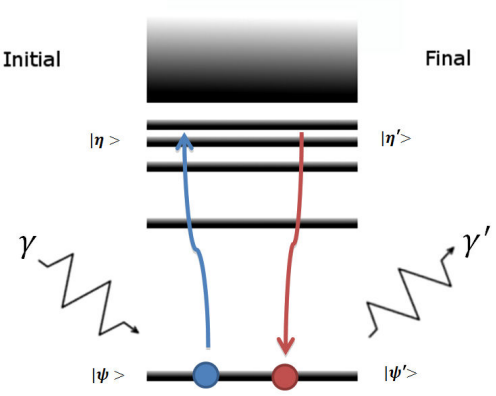

Figure 2.2 Scheme of the resonant x-ray scattering process. An incoming X-ray photon γ excites and electron from the core shell to a valence state generating the state η that decays to the fundamental state by the generation of a second photon γ'.

2.4.1 Resonant diffraction length

The two terms from the approximation in equation (2.12) that will be discussed in the following paragraphs are explicitly depended with the X-ray energy [40, 41].

$$f_{res}(\omega) = f'(\omega) + if''(\omega) \qquad (2.28)$$

As discussed in 2.1.1 these resonant terms depend linearly on the vector potential, $p \cdot A$, and arise from the second level of approximation in the interaction between radiation and matter. It is necessary to include the definition of the current operator, $J(q)$, in terms of the electron linear momentum (p_j), position (R_j) and spin (s_j) operators, $J(q) = \sum(p_j + is_j \times q)e^{iqR_j}$. These two terms together with the Thomson contribution to the scattering length at the limit of small energy produce the Rayleigh limit of the cross-section, while the one term that admits an energy resonance gives in this condition the Kramers-Heisenberg dispersion formula. For the case presented in this thesis work, where we will just study a purely elastic scattering process, we are only interested in the energy resonance and its influence on Bragg diffraction.

For the description of the resonant X-ray scattering process, it is necessary to define intermediate states, $|\eta>$, as done in figure 2.2, these intermediate states are not from the equilibrium configuration of the crystal as happens for the initial and final states, $|\psi>$, and they decay on a timescale $\sim \hbar/\Gamma$, where Γ is the total width of the resonance, to one of these final fundamental states. The contribution to the scattering length from a resonant event can be written as

$$f_{res} = -\left(\frac{r_e}{m_e}\right)\sum_{\eta(\Delta)} \frac{\langle\psi'|\varepsilon'\cdot J(-q')|\eta\rangle\langle\eta|\varepsilon\cdot J(q)|\psi\rangle}{E-\Delta+i\Gamma/2} \qquad (2.29)$$

where the limit of the sum $\eta(\Delta)$ imposes the contribution only from the intermediate states that contribute to the resonance energy, $\Delta = \mathrm{E}_\eta - \mathrm{E}_\psi$. As the energy profile dependence is observed usually like a single oscillator, we can dismiss the weak dependence from Γ and Δ from the intermediate states.

The next step in our presentation of the scattering length is defining the current operators as a sum over the electrons and ions inside the unit cells that participate in the resonant scattering process. The electronic wavefuction is defined with and arbitrary phase factor that is different for each ion, being necessary to include an average over these phases, and all other degenerate variables associated with the equilibrium state of the crystal, inside the mean value denoted by $\langle \ldots \rangle$. The average of the individual phase factor is zero and thus cross-terms in the product of $J(-q')$ and $J(q)$ are zero averaging. Resulting the

numerator in (2.29) a sum over the ions in the unit cells, the electrons associated with the ions. The spatial phase factor from the current operators are e^{idG}.

Now expanding $J(q)$in first order in q [48], we obtain,

$$\langle\eta|\varepsilon\cdot J(q)|\mu\rangle = (im_e\Delta)\sum_j \langle\eta\left|\varepsilon\cdot R_j\left(1+\tfrac{i}{2}q\cdot R_j\right)\right|\mu\rangle + \left(\tfrac{i}{2}\right)\langle\eta|(q\times\varepsilon)\cdot(L+2S)|\mu\rangle \qquad (2.30)$$

where the first term of the sum define the charge-dipolar, E1, and charge-quadrupolar, E2, processes and the second term, which is related to the magnetic moment $(L+2S)$, defines the magnetic-dipolar, M1, process. The order of magnitude of the strength of an $E1$ resonance event is given by an atomic electric dipole ea_0, where a_0 is the Bohr radius, and the strength of an $M1$ event is given by a Bohr magneton $\mu_B = \alpha^2 a_0$, where α is the fine-structure constant $\approx 1/137$. Thus, the relative strengths of $E1$ and $M1$ are expressed by ratio $M1/E1 \approx \alpha/2$. The strength of an $E2$ event depends on the magnitude of the x-ray wavevector $q \approx 0.51\,E\,(keV)$ Å^{-1}, where E is the x-ray energy, and we achieve an estimate $E2/M1 \approx E/(27\,eV)$. From this ratio we can assume that the E1 process will be dominant. Otherwise, the importance between the E2 and the M1 processes can be similar although the experimental evidence is that E2 is more significant for the x-ray regime. In this same style, the contribution related to an E1E2 event is expected to be stronger than the one of a possible E1M1.

In the formalism that will be present in the following subchapters, there is an additional assumption, where the dependence of the numerator in (2.29) with the projection $\bar{M}$ of the angular momentum of the core state $\bar{J}$ is neglected [49, 50]. This assumption is valid just for the case of the approximation of the energy profile to a single oscillator, where there is not interaction between the core state and the photo-ejected electron and there is not presence of an exchange coupling of the core and valence states. On the other hand, if the shape of the peak is not similar to a single Lorentzian it would be necessary to assume the degeneracy with respect to $\bar{M}$ [26, 51, 52].

This assumption, similar to the simplification of fast collision presented by Hannon et al. and Luo et al [53, 54, 55], consists in the omission of the energy of dispersion for the intermediate states, i.e., only is taken into account the $n = 0$ term of the serie,

$$(E - \Delta + i\Gamma/2)^{-1} = (\bar{E}_I - E_0 - \Delta + i\Gamma/2)^{-1} \sum_{n=0}^{\infty} \frac{\bar{E}_I - E_I}{\bar{E}_I - E_0 - \Delta + i\Gamma/2} \qquad (2.31)$$

where $E = \bar{E}_I - E_0$, representing E_I and E_0 the energy of the excited and fundamental states, and defining $\bar{E}_I$ as the mean value of the energy of the excited states. This expression is valid in the case that the denominator is much smaller than the dispersion of the energy of the excited states, $\Delta E_I = \sqrt{\overline{(E_I - \bar{E}_I)^2}}$. This value represents also the frequency at which the changes in the valence level will happen due to the presence of an electron from the core level that leaves a core hole that the electron will try to fill as in Figure 2.2.

2.4.2 Even transitions under spatial inversion, E1E1 & E2E2

E1E1event

The strongest contribution to the cross-section is related to the pure charge-dipolar event, (E1E1), this event will be visible in the energy profile at an energy Δ_1. We can define the scattering length as

$$f_{E1E1} = -\left(\frac{2\pi e}{\lambda}\right)^2 \frac{Z(E1E1)}{E - \Delta + i\Gamma/2}, \qquad (2.32)$$

Here, the pre-factor is obtained by comparing Δ and the X-ray energy $E = 2\pi\hbar/\lambda$. And $Z(E1E1)$ represents a scalar quantity related to the sum over all the d sites of the unit cell that dependent in R_j of the first term in (2.30),

$$Z(E1E1) = \sum_d e^{iG\cdot d} \sum_{\eta(\Delta)} \langle \sum_{j(d)} \{\varepsilon \cdot R_j|\eta\rangle\langle\eta|\varepsilon \cdot R_j\}\rangle. \qquad (2.33)$$

The scalar quantity $Z(E1E1)$ can be written in terms of the amplitude, $F(E1E1)$, that depends on the atomic tensor $\langle T_Q^K \rangle_{E1}$ and a spherical tensor

$$F(E1E1) = \sum_{KQ} (-1)^Q X_{-Q}^K \Psi_Q^K, \qquad (2.34)$$

where X_Q^K is

$$X_Q^K = \sum_{qq'} \varepsilon_q{}' \varepsilon_{q'} (1q1q'|KQ), \qquad (2.35)$$

and we are defining the cell structure factor, Ψ_Q^K, as a sum of all the atomic tensor $\langle T_Q^K \rangle_{E1}$, defined in Appendix B, of the resonant ions at d site

$$\Psi_Q^K = \sum_d e^{iG\cdot d}\,\langle T_Q^K\rangle_{E1,d}. \qquad (2.36)$$

As X_Q^K is define from two vector quantities, the triangular condition gives K=0,1 and 2. In Table 2.2 are specific the values of X_Q^K that are required for the calculation of the amplitudes due to dichroism or Bragg Scattering signals for a E1E1 event.

Table 2.2 Properties of X_Q^K defined in (2.35). The non-zero elements are presented for the different initial and final states.

	$X_{-Q}^K = (-1)^{K+Q}\left(X_Q^K\right)^*$	
	$X^1 = \frac{i}{\sqrt{2}}(\varepsilon' \times \varepsilon)$,	$X_{+2}^2 = (\varepsilon'_{+1}\varepsilon_{+1})$,
(σ' σ)	$X_0^0 = \frac{-1}{\sqrt{3}}$,	$X_0^2 = \left(\frac{2}{3}\right)^{1/2}$,
(σ'π)	$X_{+1}^1 = \frac{1}{2}e^{i\theta}$,	$X_{+1}^2 = -\frac{1}{2}e^{i\theta}$,
(π'σ)	$X_{+1}^1 = -\frac{1}{2}e^{-i\theta}$,	$X_{+1}^2 = -\frac{1}{2}e^{-i\theta}$,
(π'π)	$X_0^0 = \frac{-1}{\sqrt{3}}\cos(2\theta)$,	$X_0^1 = \frac{i}{\sqrt{2}}\sin(2\theta)$,
	$X_0^2 = \frac{-1}{\sqrt{6}}\cos(2\theta)$,	$X_{+2}^2 = \frac{1}{2}$,

Now, let's look a bite more deeply inside the dependence with R_j,

$$\sum_{\eta(\Delta)}\langle\sum_{j(d)}\{\varepsilon\cdot R_j|\eta\rangle\langle\eta|\varepsilon\cdot R_j\}\rangle = \left(l\|C(1)\|\bar{l}\right)\left(\bar{l}\|C(1)\|l\right)\langle l|R|\bar{l}\rangle^2 \times \sum_{KQ}(-1)^Q X_{-Q}^K\langle T_Q^K\rangle_{E1,d}, \qquad (2.37)$$

where we are leaving out the dependence of $\langle T_Q^K\rangle_{E1,d}$ from the radial integral $\{R\}_{sp} = \left(l\|C(1)\|\bar{l}\right)\langle l|R|\bar{l}\rangle$ that may depend on the orbital core and valence states that we denoted as $\bar{l}$ and l, respectively. The reduced matrix element $\left(l\|C(1)\|\bar{l}\right)$ related to the normalized spherical harmonic is [56, 57]

$$\left(l\|C(1)\|\bar{l}\right) = (-1)^l\{(2l+1)(2\bar{l}+1)\}^2\begin{pmatrix} l & t & \bar{l} \\ 0 & 0 & 0\end{pmatrix}, \qquad (2.38)$$

Now we can write $Z(E1E1)$ as

$$Z(E1E1) = \left(\frac{m\Delta a_0{}^2}{\hbar^2}\right)\left(\frac{\{R\}_{sp}}{a_0}\right)^2 F(E1E1), \qquad (2.39)$$

In order to express various contributions to a resonant signal in the same unit, it is necessary to introduce the classical radius of the electron as a dimensionless factor $\left(\frac{m\Delta a_0{}^2}{\hbar^2}\right)$ where Δ is the energy of the photon event.

E2E2 event

The next term in equation (2.30) is quadratic with R_j, defines the energy of a pure quadrupolar (E2E2) event and appears usually at a lower energy Δ_2 in the energy profile. It is possible to define the amplitude of the signal in terms of a scalar value $\mathrm{Z}(E2E2)$

$$Z(E2E2) = \left(\frac{q\{R^2\}_{sd}}{a_0}\right)^2 \left(\frac{m\Delta {a_0}^2}{\hbar^2}\right) F(E2E2), \qquad (2.40)$$

where $\{R^2\}_{sd} = (l\|C(2)\|\bar{l})\langle l|R^2|\bar{l}\rangle$, and the structure factor $\mathrm{F}(E2E2)$ can be defined in terms of a scalar product of H_Q^K, which describes the polarization and directions of the primary and secondary X-ray beam, and the atomic tensors $\langle T_Q^K\rangle_{E2}$ inside the cell structure factor Ψ_Q^K,

$$F(E2E2) = \sum_{KQ}(-1)^{K+Q}\, H_{-Q}^K \Psi_Q^K. \qquad (2.41)$$

For the pure E2 process we can define the cell structure factor

$$\Psi_Q^K = \sum_d e^{iG\cdot d}\, \langle T_Q^K\rangle_{E2,d}, \qquad (2.42)$$

where the mean value $\langle T_Q^K\rangle_{E2}$ is obtained with matrix elements that satisfy the Wigner-Eckart theorem and a reduced matrix element as the one specify in appendix B. The triangular condition give that K= 0,1,2,3 and 4 in this as H_{-Q}^K and Ψ_Q^K are products of tensors of rank 2. The other term in (2.41) is related to the polarization and can be written as

$$H_Q^K = \sum_{qq'} h(q)h'(q')(2q2q'|KQ) \qquad (2.43)$$

with $h(q)$ ($h'(q)$) as the coupling between ε (ε') and $\hat{q}$ ($\hat{q}'$) for giving a tensor of rank 2,

$$h(q) = \sum_{pp'} \varepsilon_p \hat{q}_{p'}(1p1p'|2q), \qquad (2.44)$$

in Table 2.3 is written some of the properties of H_Q^K.

The correspondence between the atomic tensors and the magnetic character is in the case of pure parity-even events, as E1E1 and E2E2, related to the rank of the tensors, i.e., the odd (even) rank tensors are parity-odd (even) processes or related to magnetic (charge) scattering. This correspondence is implicit in relation (2.27) for parity-even tensors, and it says that even rank tensors do not change

sign when the field is reversed, while odd rank tensors change sign when the polarity of the local magnetic field is reversed. This property is inserted in the future calculation of the structure factors in the way that in the absent of an external magnetic field or the presence of a magnetic long-range ordering the odd rank tensors for pure E1 and pure E2 channels will be neglected.

Table 2.3 Properties of H_Q^K defined in (2.43). The non-zero elements are presented for the different initial and final states, supposing an elastic $q = q'$ process.

	$H_{-Q}^K = (-1)^{K+Q}\left(X_Q^K\right)^*$			
	$H^1 = \frac{i}{2\sqrt{10}}(\varepsilon' \times \varepsilon)$,		$H^1 = \frac{1}{2\sqrt{5}}X^1$,	
$(\sigma'\,\sigma)$	$H_0^0 = \frac{1}{2\sqrt{5}}\cos(2\theta)$,	$H_0^1 = \frac{i}{2\sqrt{10}}\sin(2\theta)$,	$H_0^2 = \frac{-1}{2\sqrt{14}}\cos(2\theta)$,	$H_{+2}^2 = \frac{1}{4}\left(\frac{3}{7}\right)^{\frac{1}{2}}$,
		$H_0^3 = \frac{-i}{\sqrt{10}}\sin(2\theta)$,	$H_0^4 = \left(\frac{2}{35}\right)^{\frac{1}{2}}\cos(2\theta)$,	$H_{+2}^4 = -\frac{1}{2\sqrt{7}}$,
$(\pi'\sigma)$		$H_{+1}^1 = -\frac{1}{4\sqrt{5}}e^{-3i\theta}$,	$H_{+1}^2 = \frac{1}{4}\left(\frac{3}{7}\right)^{\frac{1}{2}}e^{-3i\theta}$,	
	$H_{+1}^3 = \left(\frac{3i}{160}\right)^{\frac{1}{2}}e^{-3i\theta}$,	$H_{+3}^3 = \frac{-1}{4\sqrt{2}}e^{-i\theta}$,	$H_{+1}^4 = \frac{1}{4\sqrt{14}}e^{-3i\theta}$,	$H_{+3}^4 = \frac{1}{4\sqrt{2}}e^{-i\theta}$,
$(\sigma'\,\pi)$	$H_Q^K(\sigma'\,\pi) = (-1)^K\left(H_Q^K(\pi'\sigma)\right)^*$,			
$(\pi'\pi)$	$H_0^0 = \frac{1}{2\sqrt{5}}\cos(4\theta)$,	$H_0^1 = \frac{i}{\sqrt{10}}\sin(4\theta)$,	$H_0^2 = \frac{1}{\sqrt{14}}\cos(4\theta)$,	
		$H_0^3 = \frac{i}{\sqrt{40}}\sin(4\theta)$,	$H_0^4 = \frac{1}{2\sqrt{70}}\cos(4\theta)$,	$H_{+4}^4 = -\frac{1}{4}$,

2.4.3 Odd transitions under spatial inversion, E1E2 & E1M1

The odd transitions under spatial inversion are introduced in the formalism by the presence of the mixed terms charge-dipole charge-quadrupole, E1E2, and charge-dipole magnetic-dipole, E1M1. These mix processes are allowed in the cases that the resonant ion under study is not in a centre of inversion symmetry of the system [6]. These kinds of events can be described with a mechanism related to the electric crystal-field potential.

The absence of inversion symmetry in the site of the resonant ion allows the presence of odd-rank components to the potential. This requirement on the resonant site for non-zero contributions to Bragg diffraction from parity-odd events does not mean that the crystal structure must be non-centrosymmetric. From the atomic point of view these components are related to a possible mix between the electronic valence state of the cation state and the different atomic

shell and angular moment [58, 59]. As an example, is the possible overlap (or hybridization) of a d-state of a cation and the p-state of an anion, resulting a final state of an electron $|\psi\rangle = a|ljm\rangle + b|l'j'm'\rangle$, where $l \neq l'$, $j = l \pm 1/2$ and $j' = l' \pm 1/2$.

In the final state of the electron $|\psi\rangle$ usually the mix term ab^* is dismiss, even when ab initio calculations are good for pure E1 events, and not so confident for pure E2 or mix E1E2 processes. As happen for the case of pure E2 events, the E1E2 events are supposed to be several orders of magnitude weaker that the pure E1 contribution [60, 61].

E1E2 event

Let's continue with the definition of the amplitude related to an E1E2 mix event. In this case we have to define the scalar quantity $Z(E1E2)$ that represents a mixture between the dependence R_j and the ${R_j}^2$ of the first term in (2.30),

$$Z(E1E2) = \frac{i}{2}\sum_{\eta(\Delta)} \langle\psi| \left\{ (\varepsilon' \cdot R) \left| \begin{matrix} \eta\rangle\langle\eta|(\varepsilon \cdot R)(q \cdot R) \\ -(\varepsilon' \cdot R)(q' \cdot R)|\eta\rangle\langle\eta| \end{matrix} \right| (\varepsilon \cdot R) \right\} |\psi\rangle, \quad (2.45)$$

here the operator for the electrons changes sign under spatial inversion, i.e., $R \rightarrow -R$, due to this the mean value can be only different from zero for the case of non diagonal and parity-odd matrix elements. As previously done in the case of pure parity even events, it is possible to write $Z(E1E2)$ in terms of reduced matrix as

$$Z(E1E2) = \left(l\|C(1)\|\bar{l}\right)\langle l|R|\bar{l}\rangle q\left(\bar{l}\|C(2)\|l'\right)\langle l|R^2|\bar{l}\rangle \times \sum_{KQ}(-1)^Q \left(\widetilde{N}^K_{-Q}\langle Y^K_{-Q}\rangle + \left(N^K_Q\right)^*\langle Y^K_{-Q}\rangle^*\right), \quad (2.46)$$

that we can write in terms of the structure form factor as

$$Z(E1E2) = \left(\frac{\{R\}_{sp}}{a_0}\right)\left(\frac{q\{R^2\}_{sd}}{a_0}\right)\left(\frac{m\Delta {a_0}^2}{\hbar^2}\right)F(E1E2) \quad (2.47)$$

as happen in the case of pure events the quantities $\widetilde{N}^K_{-Q}$ and N^K_Q are related to the polarization of the incoming and outgoing beams. Because $\widetilde{N}^K_{-Q}$, N^K_Q and the tensors Y^K_Q are all products of tensors of rank 1 and rank 2 the triangular condition

gives as possible ranks K = 1, 2 and 3. The tensors are defined using the relation (2.44) between the exchange of the pairs of variables of ε , $\hat{q}$ and (ε'), $(\hat{q}')$,

$$\widetilde{N}^K_{-Q} = \frac{i}{\sqrt{5}} \sum_{pp'} h(p) \varepsilon'_{p'} (2p1p'|KQ), \qquad (2.48)$$

and

$$N^K_Q = \frac{i}{\sqrt{5}} \sum_{pp'} h'(p) \varepsilon_{p'} (2p1p'|KQ). \qquad (2.49)$$

Table 2.4 Properties of N^K_Q and $\widetilde{N}^K_Q$ defined in (2.47) and (2.48) for a E1-E2 event, and values of $(\widetilde{N}^K_{-Q} + \mathrm{N}^{\mathrm{K}}_{-\mathrm{Q}})$ and $(\widetilde{N}^K_{-Q} - N^K_{-Q})$.

$\widetilde{N}^K_{-Q} = (-1)^{\mathrm{K+Q}} \left(\widetilde{N}^K_Q\right)^*$, $\widetilde{N}^1 = -\frac{\mathrm{i}\sqrt{3}}{10}\{\hat{\mathrm{q}}(\varepsilon' \cdot \varepsilon) + (\varepsilon' \times \varepsilon) \times \hat{\mathrm{q}}\}$,		$N^K_{-Q} = (-1)^{\mathrm{K+Q}} \left(N^K_Q\right)^*$ $\mathrm{N}^1 = -\frac{\mathrm{i}\sqrt{3}}{10}\{\hat{\mathrm{q}}'(\varepsilon' \cdot \varepsilon) + \hat{\mathrm{q}}' \times (\varepsilon' \times \varepsilon)\}$,
	$(\sigma' \sigma)$	
$\widetilde{N}^1_{+1} + N^1_{+1} = \frac{-1}{5}\left(\frac{3}{2}\right)^{\frac{1}{2}} \cos(\theta)$,		$\widetilde{N}^1_{+1} - N^1_{+1} = \frac{-\mathrm{i}}{5}\left(\frac{3}{2}\right)^{\frac{1}{2}} \sin(\theta)$,
$\widetilde{N}^2_{+1} + N^2_{+1} = \left(\frac{1}{30}\right)^{\frac{1}{2}} \cos(\theta)$,		$\widetilde{N}^2_{+1} - N^2_{+1} = \mathrm{i}\left(\frac{1}{30}\right)^{\frac{1}{2}} \sin(\theta)$,
$\widetilde{N}^3_{+1} + N^3_{+1} = \frac{2}{5}\left(\frac{2}{3}\right)^{\frac{1}{2}} \cos(\theta)$,		$\widetilde{N}^3_{+1} - N^3_{+1} = \frac{2\mathrm{i}}{5}\left(\frac{2}{3}\right)^{\frac{1}{2}} \sin(\theta)$,
$\widetilde{N}^1_0 + N^1_0 = \frac{\mathrm{i}}{10}\sqrt{3}\sin(2\theta)$,	$(\pi'\sigma)$	$\widetilde{N}^1_0 - N^1_0 = \frac{\mathrm{i}}{10}\sqrt{3}\sin(2\theta)$,
$\widetilde{N}^2_0 + N^2_0 = \frac{1}{2}\left(\frac{1}{5}\right)^{\frac{1}{2}} \cos(2\theta)$,		$\widetilde{N}^2_0 - N^2_0 = \frac{1}{2}\left(\frac{1}{5}\right)^{\frac{1}{2}} \cos(2\theta)$,
$\widetilde{N}^2_{+2} + N^2_{+2} = \left(\frac{1}{30}\right)^{\frac{1}{2}} \left(\frac{1}{2} - \mathrm{e}^{-2\mathrm{i}\theta}\right)$,		$\widetilde{N}^2_{+2} - N^2_{+2} = \left(\frac{1}{30}\right)^{\frac{1}{2}} \left(\frac{1}{2} + \mathrm{e}^{-2\mathrm{i}\theta}\right)$,
$\widetilde{N}^3_0 + N^3_0 = \frac{\mathrm{i}}{5}\left(\frac{1}{2}\right)^{\frac{1}{2}} \sin(2\theta)$,		$\widetilde{N}^3_0 - N^3_0 = \frac{\mathrm{i}}{5}\left(\frac{1}{2}\right)^{\frac{1}{2}} \sin(2\theta)$,
$\widetilde{N}^3_{+2} + N^3_{+2} = -\frac{1}{2}\left(\frac{1}{15}\right)^{\frac{1}{2}} \left(1 + \mathrm{e}^{-2\mathrm{i}\theta}\right)$,		$\widetilde{N}^3_{+2} - N^3_{+2} = -\frac{1}{2}\left(\frac{1}{15}\right)^{\frac{1}{2}} \left(1 - \mathrm{e}^{-2\mathrm{i}\theta}\right)$,
$\widetilde{N}^K_Q(\sigma' \pi) = \left(N^K_Q(\pi'\sigma)\right)^*$,	$(\sigma' \pi)$	$N^K_Q(\sigma' \pi) = \left(\widetilde{N}^K_Q(\pi'\sigma)\right)^*$,
	$(\pi'\pi)$	
$\widetilde{N}^1_{+1} + N^1_{+1} = \frac{-1}{5}\left(\frac{3}{2}\right)^{\frac{1}{2}} \cos(3\theta)$,		$\widetilde{N}^1_{+1} - N^1_{+1} = \frac{-\mathrm{i}}{5}\left(\frac{3}{2}\right)^{\frac{1}{2}} \sin(3\theta)$,
$\widetilde{N}^2_{+1} + N^2_{+1} = -\left(\frac{1}{30}\right)^{\frac{1}{2}} \cos(3\theta)$,		$\widetilde{N}^2_{+1} - +N^2_{+1} = -\mathrm{i}\left(\frac{1}{30}\right)^{\frac{1}{2}} \sin(3\theta)$,
$\widetilde{N}^3_{+1} + N^3_{+1} = \frac{-1}{5}\left(\frac{1}{6}\right)^{\frac{1}{2}} \cos(3\theta)$,		$\widetilde{N}^3_{+1} - N^3_{+1} = \frac{-\mathrm{i}}{5}\left(\frac{1}{6}\right)^{\frac{1}{2}} \sin(3\theta)$,
$\widetilde{N}^3_{+3} + N^3_{+3} = \left(\frac{1}{10}\right)^{\frac{1}{2}} \cos(\theta)$,		$\widetilde{N}^3_{+3} + N^3_{+3} = \mathrm{i}\left(\frac{1}{10}\right)^{\frac{1}{2}} \sin(\theta)$,

In Table 2.4 are listed some of the properties of $\widetilde{N}^K_{-Q}$ and N^K_Q. And the structure form factor is defined as

$$F(E1E2) = \sum_{KQ} (-1)^Q \sum_d \left(\widetilde{N}^K_{-Q} \langle Y^K_{-Q} \rangle_d + \left(N^K_Q\right)^* \langle Y^K_{-Q} \rangle_d{}^*\right) e^{iG \cdot d}, \qquad (2.50)$$

where the tensors Y^K_Q can be related to other tensors with symmetric and anti-symmetric properties. As an E1E2 event is spatially odd for having a symmetric

property is necessary to use a time-odd and inversion-odd tensor that we will denote by G_Q^K (magnetoelectric), this type of tensors is related to the magnetic structure of the material and will appear as happen in the case of the odd rank tensor in parity even tensors. The anti-symmetric tensor that we will denote by U_Q^K(polar) are in the other hand time-even, the derivation of these tensors in terms of the reduced matrix elements is done in appendix C.

Then the structure factor in terms of these tensors will be written as

$$F(E1-E2)=\sum_K i^K \sum_Q (-1)^Q \begin{Bmatrix} -i\Psi_Q^{K,g}\left(\widetilde{N}_{-Q}^K + N_{-Q}^K\right) \\ +\Psi_Q^{K,u}\left(\widetilde{N}_{-Q}^K - N_{-Q}^K\right) \end{Bmatrix}, \qquad (2.51)$$

where $\Psi_Q^{K,g}$ and $\Psi_Q^{K,u}$ denote the cell structure factor and depend on $G_Q^K$and U_Q^K,

$$\Psi_Q^{K,g}=\sum_d e^{iG\cdot d}\langle G_Q^K\rangle_d, \qquad (2.52)$$

$$\Psi_Q^{K,u}=\sum_d e^{iG\cdot d}\langle U_Q^K\rangle_d. \qquad (2.53)$$

One particular property of interest in future structure factor calculations is their symmetry to the time inversion, where in the presence of a local magnetic field H, the magnetoelectric tensor will change in sign $\langle G_Q^K\rangle_H = -\langle G_Q^K\rangle_{-H}$ and the polar tensors will not change $\langle U_Q^K\rangle_H = \langle U_Q^K\rangle_{-H}$. The rank of these tensors defines them as true-tensors or pseudo-tensors if their rank is odd or even, respectively.

E1M1 event

As happen between E1 and E2, the parity of M1 is also opposite to the one of E1. Thus the E1M1 process result from this type of interaction will be parity-odd and capable of revealing atomic polar and magneto-electric multipoles. The term now under study is related to a coupling of the dependence with R_j from the first term in (2.30) and the magnetic approximation where appears the contribution of the spin-orbit $(2L+S)$. The presence S in the M1 operator allows enhancement at a K-edge, which would otherwise be forbidden on account of zero orbital angular momentum. To engage the M1 event in diffraction, or dichroism, valence and intermediate states have common angular momentum, because matrix element of l

and S are diagonal with respect to orbital angular momentum. Thus RXS at a K-edge can induce E1M1 events when s-like valence states are available [62].

As in the case of the event E1E2 we can define the value of Z(E1M1) as

$$Z(E1M1) = \frac{1}{2}\sum_{\eta(\Delta)}\sum_{jj'}\langle\psi|\left\{\left(\varepsilon'\cdot R_j\right)\left|\begin{matrix}\eta\rangle\langle\eta|(q\times\varepsilon)\cdot\mu_{j'}\\+(q'\times\varepsilon')\cdot\mu_j|\eta\rangle\langle\eta\end{matrix}\right|\left(\varepsilon\cdot R_j{}'\right)\right\}|\psi\rangle, \quad (2.54)$$

where $\mu_j = (L+2S)_j$ and can be written in terms of the structure factor F(E1M1) as follows

$$Z(E1M1) = \left(\frac{\{R\}_{sp}}{a_0}\right)\{1\}_{\gamma\gamma}F(E1M1), \quad (2.55)$$

here, the radial integral, denoted by $\{1\}_{\gamma\gamma}$, is an overlap of two orbitals of the same angular momentum, γ, with components which may be centred on different ions. The magnitude of $\{1\}_{\gamma\gamma}$ is essentially a measure of configuration interactions and bonding, or covalence, of a cation and ligands.

Table 2.5 Properties of M_Q^K and $\widetilde{\mathrm{M}}_Q^K$ defined in (2.57) and (2.58), and values of $(\widetilde{M}_{-Q}^K + \mathrm{M}_{-\mathrm{Q}}^{\mathrm{K}})$ and $(\widetilde{M}_{-Q}^K - M_{-Q}^K)$.

$\widetilde{M}_{-Q}^K = (-1)^{\mathrm{K+Q}}(\widetilde{M}_Q^K)^*$		$M_{-Q}^K = (-1)^{\mathrm{K+Q}}(M_Q^K)^*$
$\widetilde{M}_{+1}^1 + M_{+1}^1 = -\cos(\theta)$,	(σ′ σ)	$\widetilde{M}_{+1}^1 - M_{+1}^1 = -\mathrm{i}\sin(\theta)$,
$\widetilde{M}_{+1}^2 + M_{+1}^2 = -\cos(\theta)$,		$\widetilde{M}_{+1}^2 - M_{+1}^2 = -\mathrm{i}\sin(\theta)$,
$\widetilde{M}_0^0 + \mathrm{M}_0^0 = \frac{2}{\sqrt{3}}\sin^2(2\theta)$,	(π′σ)	$\widetilde{M}_0^0 - \mathrm{M}_0^0 = \frac{-2}{\sqrt{3}}\cos^2(2\theta)$
$\widetilde{M}_0^1 + \mathrm{M}_0^1 = \frac{-\mathrm{i}}{\sqrt{2}}\sin(2\theta)$,		$\widetilde{M}_0^1 - M_0^1 = \frac{-\mathrm{i}}{\sqrt{2}}\sin(2\theta)$,,
$\widetilde{M}_0^2 + M_0^2 = \frac{-1}{\sqrt{6}}\{1+2\cos^2(\theta)\}$,		$\widetilde{M}_0^2 - M_0^2 = \frac{1}{\sqrt{6}}\{1+2\sin^2(\theta)\}$,
$\widetilde{M}_{+2}^2 + M_{+2}^2 = 1/2$,		$\widetilde{M}_{+2}^2 - \mathrm{M}_{+2}^2 = 1/2$,
$\widetilde{M}_Q^K(\sigma'\,\pi) = \left(M_Q^K(\pi'\sigma)\right)^*$,	(σ′ π)	$M_Q^K(\sigma'\,\pi) = \left(\widetilde{M}_Q^K(\pi'\sigma)\right)^*$,
$\widetilde{M}_{+1}^1 + M_{+1}^1 = -\cos(\theta)$,	(π′π)	$\widetilde{M}_{+1}^1 - M_{+1}^1 = \mathrm{i}\sin(\theta)$,
$\widetilde{M}_{+1}^2 + M_{+1}^2 = \cos(\theta)$,		$\widetilde{M}_{+1}^2 - +M_{+1}^2 = -\mathrm{i}\sin(\theta)$,

As done in the case of E1E2, the structure factor is possible to be written in terms of the symmetric and asymmetric tensors G_Q^K and U_Q^K; in this case the polarization of the beam is described by the terms M_Q^K and $\widetilde{M}_Q^K$ that have similar properties as the one of N_Q^K and $\widetilde{N}_Q^K$ for the E1E2 event,

$$F(E1M1) = \sum_K i^K \sum_Q (-1)^Q \begin{Bmatrix} -i\Psi_Q^{K,g}\left(\widetilde{M}_{-Q}^K + M_{-Q}^K\right) \\ +\Psi_Q^{K,u}\left(\widetilde{M}_{-Q}^K - M_{-Q}^K\right)\end{Bmatrix}, \quad (2.56)$$

the cell structure factor are the same as in equations (2.51) and (2.52) and the values $\widetilde{M}^K_{-Q}$ and $\mathrm{M}^{\mathrm{K}}_{-\mathrm{Q}}$ are

$$\widetilde{M}^K_Q = \{(\hat{q} \times \varepsilon) \otimes \varepsilon'\}^K_Q , \tag{2.57}$$

$$M^K_Q = (-1)^K \widetilde{M}^K_Q . \tag{2.58}$$

The properties for these tensors are similar to the ones used in the E1E2 event and are listed in Table 2.5.

2.4.4 Chiral Structure

A chiral structure can be defined as a long ordering in a material due to its magnetic or electric dipolar moments. The amplitude of this type of structures can be described using the formalism base in the tensor T^K_Q, G^K_Q and U^K_Q presented in the previous sections. This long ordering affect many cells that must be take into account in the calculations, being necessary to introduce a super-cell structure factor where all the cells will be well described.

In the work by V. Scagnoly et al. [63] is presented a formalism to reduce the structure factor of multiple cells to a single super-cell structure factor, $L = (2n+1)a$ where a is the lattice parameter and n an integer. Defining the values $\langle C^K_Q \rangle$ as a combination of the tensors T^K_Q (G^K_Q and U^K_Q) for the unit cell, which will be included in the super-cell structure factor for the $(2n+1)$ cells. The integer f measures the wave-vector in units of the fraction $(2p/L) = 2p/\big(L(2n+1)\big)$, while the turn angle is equal to $2p/(2n+1)$. In general, the complex conjugate of C^K_Q do not satisfy the relation $\big(C^K_Q\big)^* = (-1)^Q\big(C^K_{-Q}\big)$. As only rotation proper are used the result for all tensors parity-even and parity-odd are equally described by the values C^K_Q. General properties include:

(a) Multipoles are symmetric under rotation by 180º about the axis normal to the plane of the cycloid.

(b) Using the identity $\mathrm{C}_{2\mathrm{x}}\langle C^K_Q \rangle = (-1)^f \langle C^K_Q \rangle$ one finds the relation $\langle C^K_{-Q} \rangle = (-1)^f (-1)^K \langle C^K_Q \rangle$.

(c) For given f and K all $\langle C_Q^K \rangle$ are proportional to one another. Scaling coefficients are complex and depend on both the magnitude and sign of the projection Q.

(d) $\langle C_Q^K \rangle$ does not depend on n.

(e) $\langle C_Q^K \rangle$ is not Hermitian.

(f) $\langle C_Q^K \rangle = 0$ for $K < f$.

The selection of f and n is done trying to minimize them in a way that the structure described has similar symmetry properties to the real chiral structure. For example, in R3c structure described for $BiFeO_3$ with a wave vector q~0.0045 r.l.u, the value of f=1 and n=2 give an enough good approximation.

Let's define the rotation angle of the chiral structure as $\phi = 2\pi/(2n+1)$. The generic form of our cycloidal structure factor is,

$$C_Q^K = \sum_{m=0}^{2n} \frac{e^{im\phi f}}{2n+1} \langle T_Q^K \rangle_m \qquad (2.59)$$

where $\langle T_Q^K \rangle_m$ stands for $\langle T_Q^K \rangle$ rotated in the plane of the cycloid through an angle $m\phi$.

The cycloid in the case of $BiFeO_3$ is rotating along the x-z plane, applying rotation properties we arrive from Eq. (2.59) to

$$\left(C_Q^K \pm C_{-Q}^K\right) = \frac{1}{2n+1}\left[\langle T_Q^K \rangle \pm (-1)^Q \langle T_Q^K \rangle^*\right] + \sum_q \left[\langle T_q^K \rangle \pm (-1)^Q \langle T_q^K \rangle^*\right]$$

$$\times \sum_m d_{Qq}^K(m\phi)\{\, cos(m\phi f)[1 + (-1)^{Q+q}] + i\, sin(m\phi f)[1 - (-1)^{Q+q}]\} \qquad (2.60)$$

here $d_{Qq}^K(m\phi)$ is a purely real element of the rotation matrix. The sum on m ranges from m=1 to m=n, and $-K \le q \le K$. If the projection Q is restricted to either even or odd integer values, (2.60) are purely real or purely imaginary. Such conditions on the projection might be imposed by the symmetry of the environment in which the reference ion is placed. But in general C_Q^K will be a complex number.

CHAPTER 3

Resonant Elastic X-ray Scattering Experiments

The advantage of new large synchrotron facilities designed for x-ray production has made viable techniques as Resonant Elastic X-ray Scattering (REXS), which use every major property of the radiation coming from these types of sources.

3.1 REXS Beamlines (Synchrotron Sources)

As commented in the section 1.2 from Chapter 1, in our days x-rays are produced by two types of methods; conventional x-rays tubes that use a anode where the x-rays are extracted by the collision between the charge particles and the ions in the material (the wave length of this type of x-rays are strongly related to the material used as anode) and synchrotron facilities, where x-rays are produced by the application of magnetic fields to charge particles moving along a tube (the wave length for this case cover all the electromagnetic range from hard x-rays to the infrared). This last radiation pattern has a strong polarization component in the plane where the electrons are been moving, being parallel to the trajectory of the electrons along the ring and it is denoted as σ while the component perpendicular to the orbit of the electron is π.

- The first step in the production of this type of X-rays was done by the implementation of the **Bending Magnets** (Figure 3.1.a.). Although, they are not the most brilliant way of producing X-ray from a synchrotron source, they have an intense power of radiation when the

electron velocity points directly towards the observer. The typical frequency in the spectrum is γ^3 times the cyclic frequency of the orbiting electron in the storage ring, γ is a relation between the energy of the electrons and its rest mass, 0.511 MeV, (E_e/m_0c^2). This power lies faster when the angle between the direction to the observer and the electron velocity is of order γ^{-1}.The polarization of x-rays due to this kind of magnets is linear in the horizontal plane, whereas it becomes circular out of the orbit plane, with opposite helicity below and above the plane. The radiation is pulsed with a duration related to the length of the bunch of particles.

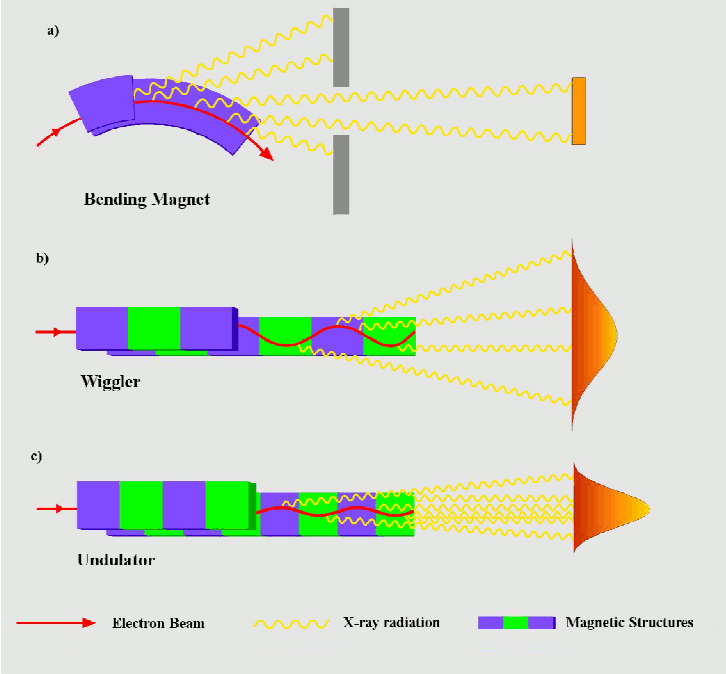

Figure 3.1 a) X-ray print from a Bending Magnet, b) X-ray print from a Wiggler type insertion device and c) X-ray print of an undulator type insertion device.

In third generation sources it is possible to introduce straight sections of small magnets (insertion devices) that produce a brighter signal. There are two types of insertion devices defined by the parameter $K = \alpha \cdot \gamma$, where α is defined as the maximum angle of deviation of the straight trajectory:

- **Wigglers** (K>>1): inside the magnetic field of this kind of insertion device the electrons follow a series of circular arcs as shown in Figure

3.1.b. This leads to incoherent sum of the intensities coming from the different oscillations along the trajectory that produce an increment in the intensity of the radiation observed by a factor of 2N, being N the number of periods. For this kind of devices the spectrum is the same as that from a bending magnet of the same field strength.

❖ **Undulators** (K ≈ 1): they are based in the possibility of making the oscillations of the electrons be in phase along the array of magnets, Figure 3.1.c. This implies that the amplitudes of the radiated waves are first added, and then the sum is squared to obtain the resulting intensity of the order of N^2 as shown in figure 1.2 c. This coherent addition of amplitudes implies a quasi-monochromatic, just one λ_u, spectrum (with the presence of harmonics) due to the finite number of periods. The print of an undulator is defined in the space by a cone with an opening of $1/(\gamma\sqrt{N})$. The λ_u typical from an undulator is defined as in equation (3.1).

$$\lambda_u = \frac{\lambda_0}{2\gamma^2}\left(1 + \frac{K^2}{2}\right) \qquad (3.1)$$

The high intensity, low divergence, high degree of polarization of the beam (mainly linear σ) and the huge control over the energy (tuneability of the beam) are requirements of crucial interest for all these experiments based in X-ray dichroism and X-ray diffraction in our days, and in particular for the case of resonant X-ray diffraction:

- High intensity: working in forbidden reflections reduces the scattered intensities with respect to allowed ones. High-intensity sources provide a larger count rate that improves the signal and also reduces the size of the sample under study.
- High collimation: the low divergence of the X-rays coming from a synchrotron source (in particular in the vertical direction [15]) improves the definition of scattering angles and as a result the reciprocal space resolution.
- Tuneability: as resonant scattering must be done near an edge of an element, is a crucial requisite being able to define with the huge precision

the energy in which the information is collected. A few hundreds meV can change completely the dependence of the signal.

- The high control in the polarization properties of the beam are interesting for the study of new functional materials, being of great interest the signals from the linear $\mu'\nu$, where μ'denote the final state of polarization (σ or π) and ν the one from the primary beam (σ or π), channels or the circular polarized x-rays and matter.

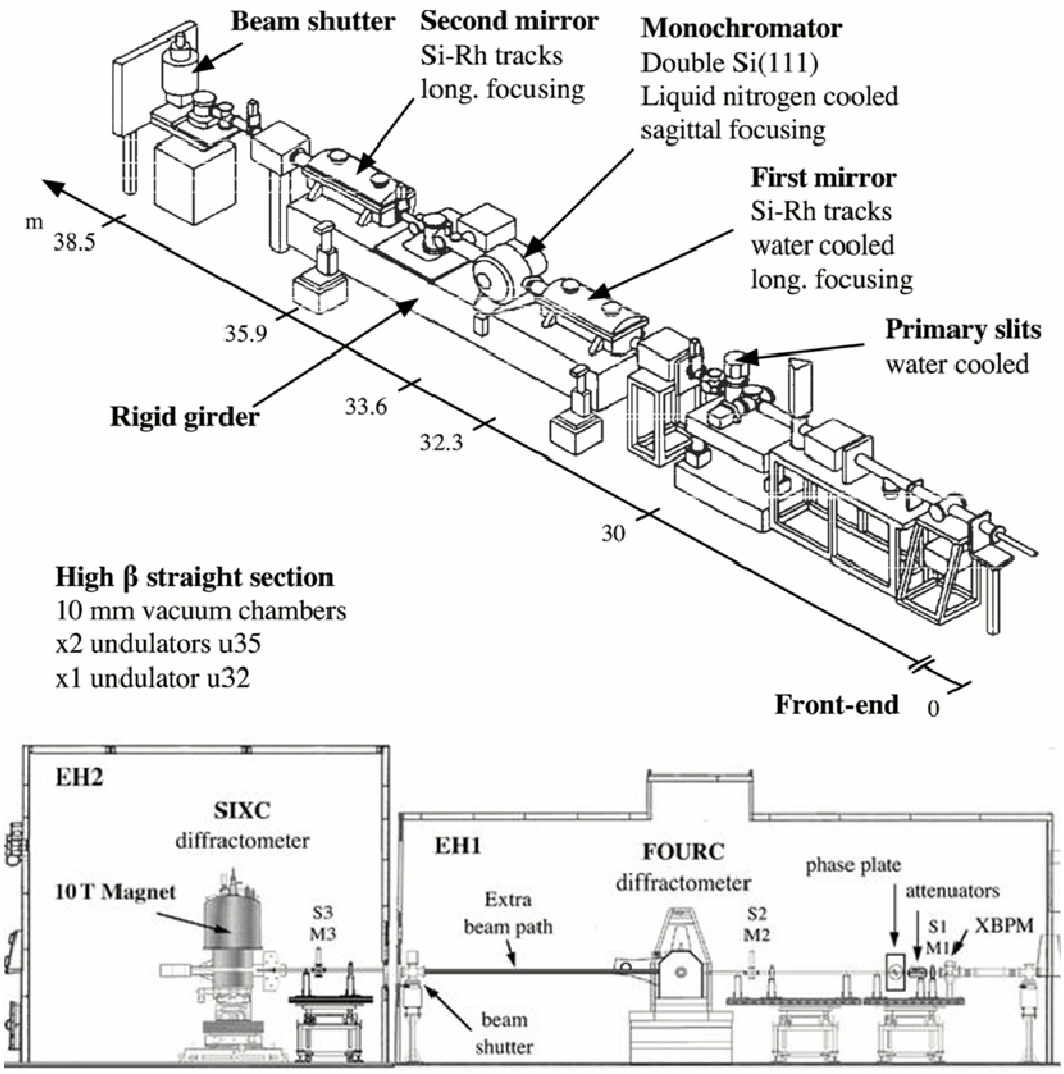

Figure 3.2. Schem of a resonant X-ray diffraction beamline. Information taken from ID20 at the ESRF [64].

The scheme of a Resonant X-ray Scattering beamline is presented in Figure 3.2. After being generated by the oscillations (bending effect) of the charge particle inside the insertion device (bending magnet), usually an undulator, the

photons go throw a series of optical instruments to improve the quality of the beam properties (collimators, monochromators, slits, mirrors and other optical instruments).

Inside the optical hutch the most important instrument for performing resonant X-ray scattering experiments are the monochromator crystals, consisting of a set two perfect crystals (or multilayers) that tune and refine the energy of the X-ray beam to the order of the 0.1 eV, this set of crystals due to the high brightness of the beam in a third generation source coming from an insertion device, and in particular in the case of an undulator, are based in Si cryo-cooled (with liquid nitrogen) or diamond water-cooled single crystals. In some beamlines there are set of more than one pair of monochromator crystals that help to cut out the presence of high harmonic signals (channel cuts). Here, the beam is also collimated to improve the divergence of the beam by the use of special gas collimators, slits and curve mirrors. Apart from these optical instruments and for the control of the beam polarization, initially σ, it is possible to find phase retarder crystals that are able to change the properties of the beam to linear π or circular right or left polarizations. As happens for the monocromators the phase retarder crystals due to the high brightness of the beam are usually based in diamond single crystal working in transition.

After the optical hutch the beam enters in the experimental hutch, where there are set slits and beam monitor positions instruments to define the final path and collimation of the beam near the sample environment at the diffractometer. The position of the sample inside the diffractometer is one of the most important steps one has to take into consideration while performing a resonant X-ray diffraction experiment based in Templeton and Templeton scans (T&T). In these kinds of scans the area of the sample under study must always be in the center of rotation of the diffractometer, to avoid the possible effect of different contributions coming from the possible domains of the sample. New six axis diffractometers as the ones presented in Figure 3.3 help in this kind of aspect giving more degrees of freedom.

The signal coming from the sample is recorded by a detector situated at the end of the arm of the diffractometer, which is moving around one of the axis or circles of the diffractometer as present in Figures 3.3. In resonant x-ray

experiments is of important interest the polarization definition of the scatter beam. For this reason usually before the detector is situated a single crystal, known as crystal analyzer, which will just diffract into the detector one of the polarization components of the scatter beam. The selection of the single crystal analyzer is done according to the material and the edge under study, in the case of Fe K-edge is commonly used Cu (220) as crystal analyzer, but it can be also used other crystals as graphite (006) or Al (331), due to the high polarization selection and the geometry of this reflection.

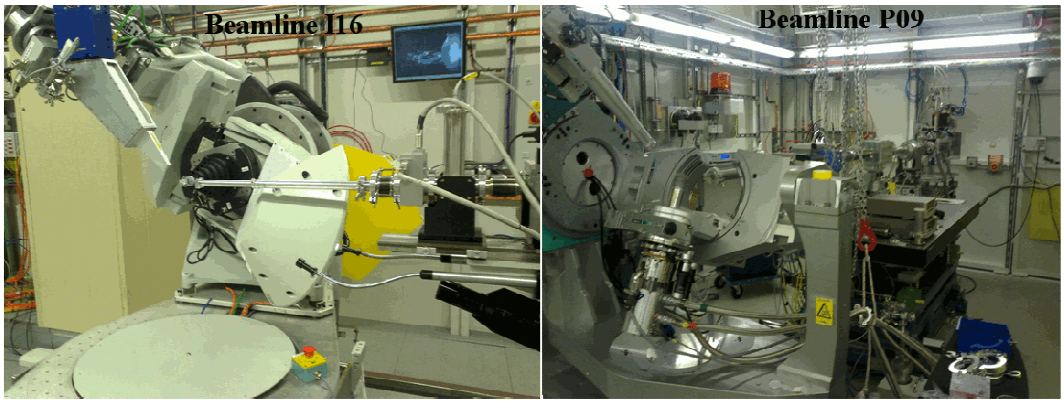

Figure 3.3. Six circles X-ray diffractometer from (left) I16 at DLS and (right) P09 at PETRA III.

Some features one must take into account when getting ready for performing a resonant magnetic x-ray scattering experiments are the following. This kind of experiments must be done in single-crystals; this technique provides the orientation and the magnitude of local moments. The penetration depth of x-rays, of 100 of microns, gives information of near surface atoms, which help in the study of surfaces, thin layers and magnetic multilayer structures definition. The possibility of combining magnetic diffraction and high energy spectroscopy is unique to resonant X-ray scattering, and has some very important potential applications. Most obviously, one can tune to the absorption edges of specific ion species to study the magnetic ordering of individual elements. This could prove particularly valuable in systems where the ions are very weakly polarized.

3.2 Azimuthal Scans

One of the experimental scans used to collect REXS experiments is known as T&T scans, due to the first group that reported information gathered with this

kind of scans [20]. Also known as Azimuthal scans, consists in the rotation of the sample at a fixed reflection $\tau(h,k,l)$ that satisfy the Bragg condition of scattering, and measure the intensity as a function of the angle of rotation, ψ. For this the reciprocal direction $\tau(h,k,l)$is oriented in the $-x$ direction of the experimental diffractometer as shown in Figure 3.4 and the sample is rotated in the y-z plane.

The information obtained from these experiments is strictly related to the angular anisotropy of the electrons in the valence level and provides information about the charge, orbital and magnetic degrees of freedom of the ion [21, 42, 55, 65, 66]. One interesting property, due to the Newman principle, relates the superposition of the rotational periodicity to the dependence in ψ, this happens if the ion is occupying a position in a rotation axis that coincides with the reflection under study [33, 67].

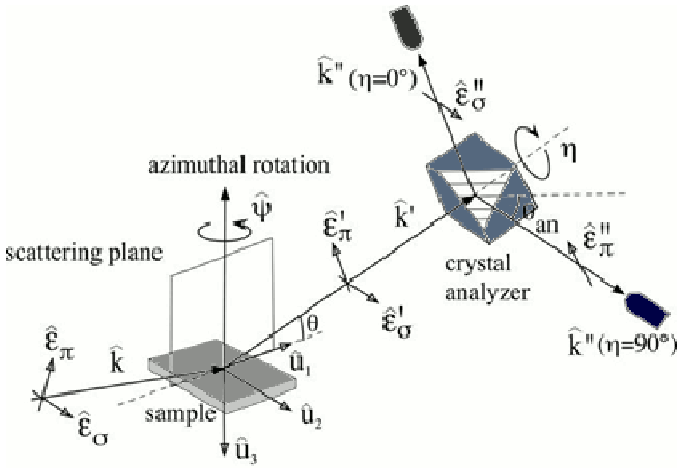

Figure 3.4. Schematic representation of the Templeton-Templeton scan configuration. The vector $\tau(h,k,l)$ is oriented in the $-x$ direction. [64]

This geometry must be taken into account in the definition of the cell structure factors Ψ_Q^K, which conventionally is defined in the basis of vectors (ξ,ψ,ζ) of the crystal, and must be translated to the experimental geometry system (x,y,z) by performing a series of rotation over the tensors to describe the reorientation of the reciprocal direction to experimental $-x$ axis.

The rotation is described by the Wigner functions $D_{QQ'}^K(-\gamma,-\beta,-\alpha)$, where the angles (α,β,γ) describe the Euler angles that define the different rotations necessary to rotate the Bragg reflection to the incoming X-ray direction [68]. The first angle, α, is related to a rotation performed keeping the z axis fixed, β

describe a rotation over y' (the y resulting after the first rotation) and finally a rotation of γ degrees over the new z'', defining the principal axis of the experiment (Appendix D).

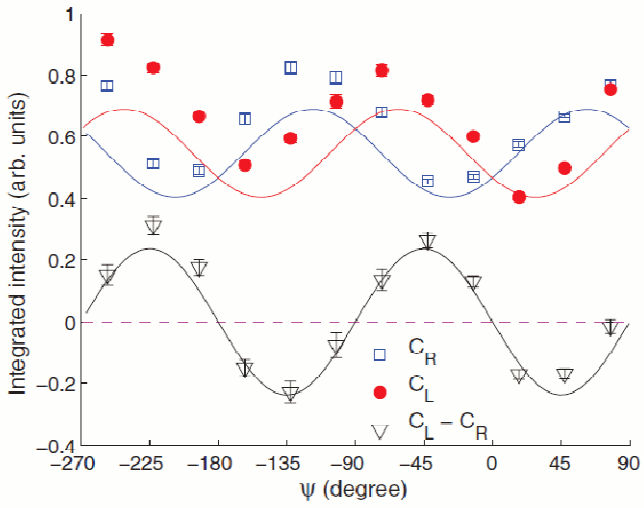

Figure. 3.5 Azimuthal angle dependence of the (1/2,0, –1/2) reflection for a CuO crystal gathered at the Cu L_2-edge for the low phase (100 K). Two different circular polarization are presented (blue open squares) for incident C_R and (red solid circles) C_L X-rays. The difference $\Delta = C_L - C_R$ is represented by open triangles. Figure obtained from Scagnoli et al. [7].

The rotation over the azimuthal angle is described by the Wigner function $D^K_{QQ'}(\frac{\pi}{2}, -\psi, -\frac{\pi}{2})$ that describes a rotation of ψ over the reciprocal direction $\tau(h,k,l)$. Resulting the variation of the diffraction amplitude for a pure E1 event equal to

$$F(E1) = \sum_{KQ}(-1)^Q X^K_{-Q} \sum_{Q'Q''} D^K_{Q''Q} \left(\left(\frac{\pi}{2}, -\psi, -\frac{\pi}{2}\right)\right) D^K_{Q'Q''}(-\gamma, -\beta, -\alpha)\Psi^K_{Q'}. \quad (3.2)$$

Experimentally, azimuthal scans (Figure 3.5) can be obtained by two different procedures. The first one based in straight performing azimuthal scans rotating through ψ trying to keep the Bragg condition [69], in this case an allowed reflection is used as normalization intensity (subtract all imprecision due to the beam and the surface under study), it is important also to take into account that in the case of allow reflections the effect of dynamical diffraction processes is much important affecting the normalization of the ψ scan for the forbidden reflection, where diffraction is mostly kinematical. The second procedure is based in performing different "θ scans" for different ψ positions [33]; the information is subtracted from the shape and the total area under the curve (Alternatively, one

can measure the integrated intensity from a crystal analyzer). For both methods it is always important to keep the beam hitting the same region on the surface of the sample, for this one must always to focus the beam in the centre of rotation of the diffractometer.

3.3 Polarization Analysis

In our days the high degree of polarization enjoyed at x-ray synchrotron sources can be used to separate two resonant contributions which are quite close in energy (about 1 or 2 eV) and that will appear to be a single peak in an energy scan, when using X-ray polarization analysis. The use of phase plates to change the incoming beam and crystal analyzers to define the final state of polarization of the signal measured are important tools in the atomic multipole definition.

To describe the polarization of a beam are commonly used the Stokes parameters [38, 48], $\boldsymbol{P} = (P_1, P_2, P_3)$ that are related to the Pauli matrix as presented in the appendix E. We will define the primary polarization with the parameters P_i and the secondary by $P_i{}'$. A linear polarized primary beam has a null value for the circular polarization, defined by stokes parameter P_2, while the other two linear parameters P_1 and P_3 will be defined by the angle η between the polarization and the z axis (defining $\eta = 0$ as σ polarization) , $P_1 = \sin(2\eta)$ and $P_3 = \cos(2\eta)$, respectively. In the case of a completely polarized beam, the degree of circular polarization is defined using the relation (3.3) as explained in Mazzoli *et al.* [70].

$$(P_2)^2 = 1 - (P_1)^2 - (P_3)^2 \qquad (3.3)$$

Using the Stokes parameters the intensity I_0 of the scatter beam can be defined as in equation (3.4) using the coefficient $G_{\mu'\nu}$, where μ' and ν define the polarization channels σ and π for the secondary and primary beam, respectibely. These coefficients can be expressed in terms of the structure form factors for the different events, described in section 2.4.2 and 2.4.3, as $G_{\mu'\nu} = \rho_{E1E1}(E)F_{\mu'\nu}$.

$$I_0 = \frac{1}{2}(1 + P_3)(|G_{\sigma'\sigma}|^2 + |G_{\pi'\sigma}|^2)$$

$$+\frac{1}{2}(1 - P_3)(|G_{\pi'\pi}|^2 + |G_{\sigma'\pi}|^2)$$

$$+P_2 Im\left(G^*_{\sigma'\pi}G_{\sigma'\sigma} + G^*_{\pi'\pi}G_{\pi'\sigma}\right)$$

$$+P_1 Re(G^*_{\sigma'\sigma}G_{\sigma'\pi} + G^*_{\pi'\pi}G_{\pi'\sigma}). \quad (3.4)$$

In our analysis of the experimental data, we have to consider a model with single oscillator amplitudes for the E1E1, E2E2, E1E2 and E1M1 event resonances centred at different energies Δ_i with different widths Γ_i. The total amplitude *G* is now taken to be

$$G = G(E1E1) + G(E2E2) + G(E1E2) + G(E1M1)$$

$$= \rho_{E1E1}F(E1E1) + \rho_{E2E2}F(E2E2) + \rho_{E1E2}F(E1E2) + \rho_{E1M1}F(E1M1). \quad (3.5)$$

here, $\rho_{E1E1}(E)$ are complex numbers given by the resonant denominators $\frac{\Delta}{E-\Delta+i\Gamma/2}$. The structure factors are defined using the atomic tensors $\langle T^K_Q \rangle$, $\langle G^K_Q \rangle$ and $\langle U^K_Q \rangle$ as presented in section 2.4.2 and 2.4.1.

From (3.3) we can infer the circular contribution to the total intensity as

$$I_c = P_2 Im\left(G^*_{\sigma'\pi}G_{\sigma'\sigma} + G^*_{\pi'\pi}G_{\pi'\sigma}\right) \quad (3.6)$$

that can be measured in a polarized x-ray beam as a difference between the completely circular left and completely circular right intensities at the detector ones known the values for P_1 and P_3 and the relation (3.3).

3.4 Multiple Diffraction

Of vital importance while studying the signal coming from weak reflections is to take into account the possibility of multiple scattering, also known as the Renninger effect. This contribution to scattering is related to the fulfilment of the Laue condition of scattering by second reflections not expected, due to a process of multiple scattering or a spread of energy in the primary beam. As presented in Figure 3.6, this behaviour that can be used to observe the quality of the crystal as done while doing Renninger scans [71], can be also a really tricky problem in the case of performing Templeton and Templeton scans, due to the fact that the signal coming from multibeam reflections is not related to electron valence band and can distort this information.

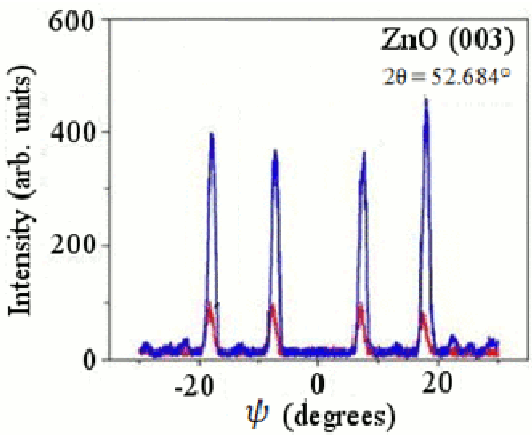

Figure 3.6 Renninger scans of ZnO (003) reflection. The Bragg angle is kept constant for the forbidden ZnO(0003) Bragg reflection at 2θ = 52.684°. [71].

In addition to the primary reflection, $\boldsymbol{\tau}$, the Ewald sphere will be satisfied by more reflections that will contribute to scattering. Let's denote by $\boldsymbol{\tau}'$ a second reciprocal lattice vector that satisfy the Laue condition for a specific azimuthal angle when rotating about $\boldsymbol{\tau}$, as done in an azimuthal scan. This is shown in Figure 3.7. Under these circumstances is common to say that we are working in a 3-beam case system. The contribution of this second reflection (that usually are produced by allow reflections) contribute strongly to the amplitude of scattering, distorting the signal detected.

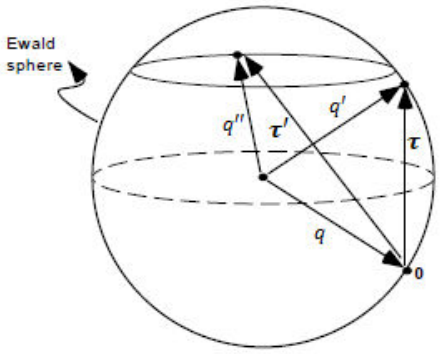

Figure 3.7. Ewald sphere representation of the 3-beam condition showing the primary $\boldsymbol{\tau}$ and secondary $\boldsymbol{\tau}'$ reflections.

The conditions under which double diffraction overlaps with an allowed or forbidden single diffraction peak are shown in Figure 3.7 and can be understood as follows. In the case of single scattering, as it is described in equation (2.8) the difference between the primary and secondary beams must be equal to the

reflection τ. For double diffraction, it is useful to pretend that the two processes occur consecutively, so after one reflection

$$\tau'' = q - \tau' = q - (q' - q''), \tag{3.7}$$

where τ' and τ'' are reciprocal lattice points. The condition why two reflections, one from a single interaction and a second with to interactions, overlap is simply described by eq (3.7), where the final direction of τ coincide with the sum of the two other processes.

$$\tau = \tau' + \tau''. \tag{3.8}$$

Finally, writing $\tau = ha^* + kb^* + lc^*$, where h, k, l are integers and the vectors a^*, b^*, c^* define the reciprocal lattice, the single and double diffraction indices must be related by $h = h' + h''$, $k = k' + k''$, $l = l' + l''$. Consequently, a forbidden reflection (h, k, l) may be overlapped by a double diffraction peak if there exist two allowed reflections (h', k', l') and (h'', k'', l'') which satisfy the above equations.

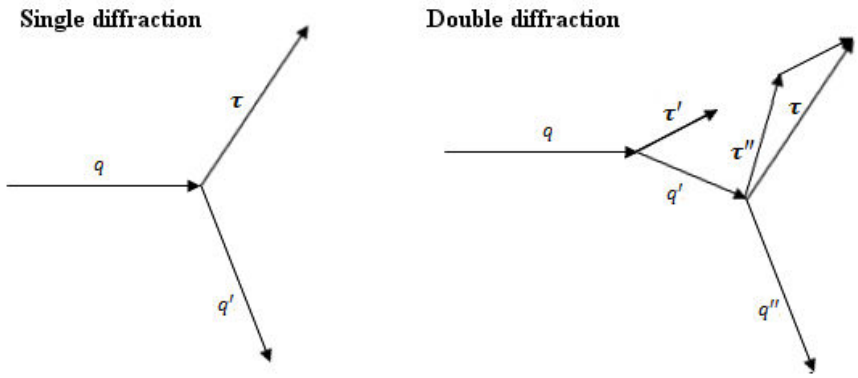

Figure 3.8. The wave vectors and momentum transfer for single and double.

Fortunately, any particular multiple diffraction peak requires a specific wavelength and sample alignment in three directions. By rotating the crystal about the scattering vector, the multiple diffraction conditions vary rapidly, while single diffraction is largely unaffected.

It is also important to remember that no beam is fully monochromatic, there is a small range of wavelengths that produce a widen effect to the boundary of the Ewald sphere, broaden the number reflections that can satisfy the Laue condition due to single or multiple beam reflections.

CHAPTER 4

Neptunium Oxide, NpO_2

Article I

Article in press in Journal of the Physics: Condensed Matter: "Neptunium multipoles and resonant x-ray Bragg diffraction by neptunium dioxide (NpO_2)".

Abstract

Recent experimental findings suggests a new symmetry for the low phase of neptunium dioxide (NpO_2) below the transition temperature $T_0 \approx 25{,}5$ K. Resonant x-ray scattering data obtained at Np $M_{4,5}$ edge from a crystal of NpO_2 were re-examining using the crystallographic point group ($\bar{3}$m) from the #224 space group instead of (m$\bar{3}$m) from the #225. From these results a derivation of the possible higher-order multipoles, such as magnetic octupolar moments, was done for the M_2, M_3 and L_2, L_3 resonant edges via E2E2 events, which might be evidenced in future experiments.

4.1 Results and Summary

NpO_2 is a member of the $Fm\bar{3}m$ (#225) space group, neptunium as an actinide atom can carry local multipole moments. These moments can order at low temperatures due to intermediate interactions such as exchange interactions. In the case of neptunium dioxide, NpO_2, when cooling below $T_0 \approx 25.5$ K there is possible to observe a single phase transition [72], similar to that of the well known antiferromagnet compound UO_2 [23]. Previous experiment done with neutron diffraction and Mössbauer spectroscopy do not reveal any magnetic order [73, 24]. This is not congruent with the fact that in NpO_2 Np^{4+} ions are Kramers system ($5f^3$). And due to this, and not depending on the crystalline environment, in the absence of interactions that break time-reversal symmetry the ground state has to carry a magnetic moment.

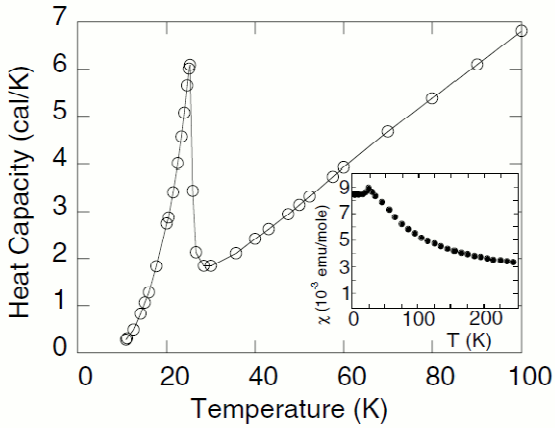

Figure 4.1. Heat Capacity [72] and magnetic susceptibility [74] of NpO_2 as a function of temperature.

The first heat capacity measurements for NpO_2 were reported in 1953 [72] and showed a large λ-like anomaly at T_0 =25 K, very similar to the one observed for UO_2 at T_N = 30.8 K, Figure 4.1. Muon spin relaxation experiments (μsR) showed a precession signal below T_0 [25], this precession is related to the magnetic field generated by the Np^{4+} ions at the muon stopping site and provides

evidence that the order parameter breaks invariance under time reversal. The magnetic moment, using muon probes, has been calculated as $0.01\mu_B$ much smaller than the paramagnetic one that is 2.95 μ_B. The measurement of the susceptibility reaches a constant value of 8.4×10^{-3} emu mol^{-1} at 4 K, figure 4.1 inset. REXS experiment performed at the Np $M_{4,5}$ absorption edges for super-lattice reflections also gave evidence of a long-range ordering in NpO_2 below T_0. These experiments showed some common features with the case of UO_2, due to the fact that the superstructure Bragg peaks occur at $\vec{Q} = \vec{G} + \langle 001 \rangle$ positions (figure 4.2), the same as in the case of the antiferromagnetic UO_2. This increases the possibility of describing the behaviour inside NpO2 as a longitudinal tripe-$\vec{q}$ antiferromagnetic order.

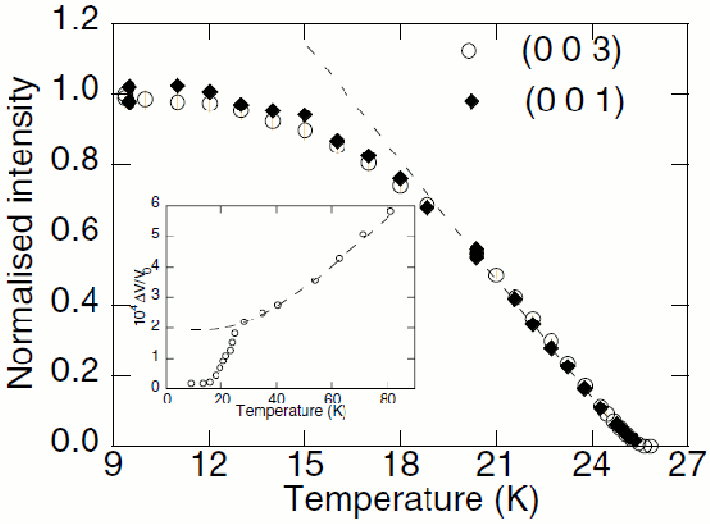

Figure 4.2. Normalized intensity of the (001) and (003) Bragg peals as a function of temperature. The inset shows the volume of the cubic unit cell as a function of temperature. Taken from [75].

Santini and Amoretti [76] first described the whole experimental evidences by the presence of a magnetic-octupolar ordering, this ordering lift a degeneracy of the Γ_8 Np ground state and generates an interstitial magnetic field, which agrees with the neutron and μsR experimental results. However, octupolar ordering only appears in the case of parity even events in pure E2E2 events ($3d_{3/2,5/2} \rightarrow 6g$), while the resonances observed in the work by Magnani et al. [75] just presented the evidence of E1 resonances ($3d_{3/2,5/2} \rightarrow 5f$) [75]. Paixao et al. performed Templeton and Templeton scans near the Np $M_{4,5}$ absorption edges [26], for this experiment they also used a polarization analyser crystal, which helped to do an unambiguous

determination of the origin of the resonance [28]. They conclude that the super-lattice peak is related to an asphericity of the Np 5f electron density leading to an anomalous tensor component in the atomic scattering factor, not arise from a magnetic ordering as previously supported by Magnani et al. [75], this conclusion is incompatible with the particular octupolar model given in Ref. [76], which predicts an undistorted density for the 5f ground states.

Later on, Lovesey and co-workers presented new evidences of the possible magnetic contribution to the scattering [52]. The crystalline structure of NpO_2 can be indexed below T_0 using both #225 and #224, Figure 4.3, space groups; this last one is a reduction of the symmetry of the one above T_0. Assuming this, they were able to adjust the azimuthal scans obtained by Paixao et al. [26] using octupoles and hexadecapoles, multipoles of rank 3 and 4 respectively, enhanced from a pure E1E1 event.

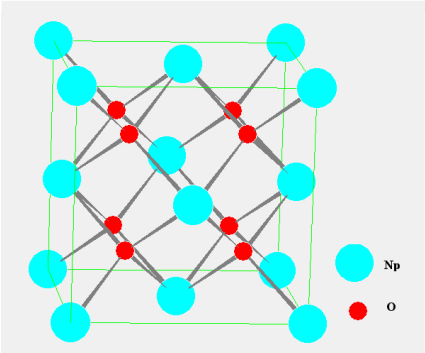

Figure 4.3. Crystal structure of Neptunium Dioxide (NpO_2) below 25 K (Pn-3m, #224), red atoms denote Oxygen in two inequivalent sites (2a) and (6e), while blue ones define Np in 4(b) Wyckoff positions.

Recent results from Nuclear Magnetic Resonance (NMR) for ^{17}O show that below T_0 there is a distortion in the crystal related to a shift on the Oxygen 2p positions (8e for #225) to a two non-equivalent sites (2a and 6d for #224) [27]. The new local symmetry of the Np ions becomes $\bar{3}m$, which permit triple-K octupoles and also the magnetic nature of the behaviour with the spherical electronic cloud around the 5f ions. In the work done during this thesis was re-derived the calculation taking into account the new point group for the Np and the new knowledge about the neptunium wave-functions that has emerged from the recent investigations in this material [52, 77, 78]. It is also presented a fully model for future dichroic experiments and possible resonant x-ray diffraction at other edges.

4.2 Article I

IOPscience iopscience.iop.org

Home Search Collections Journals About Contact us My IOPscience

Neptunium multipoles and resonant x-ray Bragg diffraction by neptunium dioxide (NpO_2)

This content has been downloaded from IOPscience. Please scroll down to see the full text.

2012 J. Phys.: Condens. Matter 24 256009

(http://iopscience.iop.org/0953-8984/24/25/256009)

View the table of contents for this issue, or go to the journal homepage for more

Download details:

IP Address: 156.35.192.2
This content was downloaded on 26/09/2013 at 16:15

Please note that terms and conditions apply.

J. Phys.: Condens. Matter **24** (2012) 256009 (7pp) doi:10.1088/0953-8984/24/25/256009

Neptunium multipoles and resonant x-ray Bragg diffraction by neptunium dioxide (NpO_2)

S W Lovesey[1,2], C Detlefs[3] and A Rodríguez-Fernández[4]

[1] ISIS Facility, STFC, Oxfordshire OX11 0QX, UK
[2] Diamond Light Source Ltd, Oxfordshire OX11 0DE, UK
[3] European Synchrotron Radiation Facility, BP 220, F-38043 Grenoble, France
[4] Department of Physics, University of Oviedo, E-33007 Oviedo, Spain

Received 21 February 2012
Published 31 May 2012
Online at stacks.iop.org/JPhysCM/24/256009

Abstract
The low-temperature ordered state of neptunium dioxide (NpO_2) remains enigmatic. After decades of experimental and theoretical efforts, long-range order of a time-odd (magnetic) high-order atomic multipole moment is now generally considered to be the fundamental order parameter, the most likely candidate being a magnetic triakontadipole (rank 5). To date, however, direct experimental observation of the primary order parameter remains outstanding. In the light of new experimental findings, we re-examine the effect of crystal symmetry on the atomic multipoles and the resulting x-ray resonant scattering signature. Our simulations use the crystallographic point group $\bar{3}m$ (D_{3d}), because corresponding magnetic groups $\bar{3}m'$, $\bar{3}'m'$ and $\bar{3}'m$ are shown by us to be at odds with a wealth of experimental results. In addition to the previously observed (secondary) quadrupole order, we derive expressions for higher-order multipoles that might be observed in future experiments. In particular, magnetic octupole moments are predicted to contribute to Np $M_{2,3}$ and $L_{2,3}$ resonant scattering via $E2$–$E2$ events. The Lorentzian-squared lineshape observed at the M_4 resonance is shown to be the result of the anisotropy of the $3p_{3/2}$ core levels. Quantitative comparison of our calculations to the measured data yields a core–hole width $\Gamma = 2.60(7)$ eV and a core-state exchange energy $|\varepsilon(\frac{1}{2})| = 0.76(2)$ eV.

(Some figures may appear in colour only in the online journal)

1. Introduction

Following an experimental investigation using Bragg diffraction by Paixão *et al* [1], neptunium dioxide (NpO_2) is now understood to undergo an uncommon form of electronic phase transition at $T \sim 25.5$ K. At the phase transition, the fluorite structure with space group $Fm\bar{3}m$ (#225) is reduced in symmetry to $Pn\bar{3}m$ (#224). Extinction rules for these two space groups are identical and, thus, they are indistinguishable with conventional Bragg diffraction. Nevertheless, the two space groups can be distinguished in a diffraction experiment exploiting Templeton–Templeton scattering. The extinction rules for Bragg reflections (HKL) with Miller indices $H + K + L$ odd arise in $Fm\bar{3}m$ from simple translations, whereas in $Pn\bar{3}m$ they arise from glide planes and screw axes. As demonstrated in [1], such reflections are visible in x-ray diffraction enhanced by an atomic resonance. Further work by Magnani *et al* [2] and Santini *et al* [3] elucidates and reviews the implications and properties of the electronic phase transition. We explore more thoroughly what electronic structure of neptunium dioxide is visible in resonant Bragg diffraction at a class of space-group forbidden reflections.

In an atomic picture of x-ray scattering used here electronic degrees of freedom are expressed in terms of multipoles that are ground-state expectation values of appropriate spherical tensor operators. Properties of a crystal, such as scattering amplitudes, must be invariant with respect to all elements of symmetry that are present (Neumann's Principle). Enforcement of symmetry generates selection rules that limit the number of multipole components that can be observed in an experiment.

Our simulations use the point group $\bar{3}m$ (D_{3d}). Implications for multipoles of symmetry operations in magnetic groups $\bar{3}m'$, $\bar{3}'m'$ and $\bar{3}'m$ are discussed in an

 © 2012 IOP Publishing Ltd Printed in the UK & the USA

appendix, and the groups are discarded in favour of $\bar{3}m$ on the grounds that corresponding multipoles do not match experimental findings [1, 3].

Appropriate selection rules were not properly implemented in a previous simulation of resonant x-ray Bragg diffraction by the low-temperature phase of NpO_2, based on an atomic picture [4]. In the present paper, we re-visit the simulation with a rigorous derivation and enforcement of selection rules, derived from both the point group and the space group. Thereby we correct misleading conclusions [4] and, in addition, provide fresh insight into the electronic properties of the low-temperature phase. Most importantly, we take full account of knowledge about the neptunium wavefunction that has emerged from investigations made after our previous paper [3, 5, 6]. Moreover, our present work could well prove a useful example for resonant Bragg diffraction studies and dichroic signals of other materials.

The next section records implications for atomic multipoles of local (point group $\bar{3}m$, D_{3d}) and global ($Pn\bar{3}m$) symmetry in the low-temperature phase of neptunium dioxide. Thereafter, in section 3, are unit-cell structure factors suitable for resonant Bragg diffraction enhanced by $E1$–$E1$ and $E2$–$E2$ resonant events at reflections $(00L)$ with Miller index L odd [1], including dependence on the azimuthal angle. Our atomic theory—using spherical tensors and atomic multipoles—is sketched in section 4. Section 5 is given over to a calculation of the energy profile and the Np multipoles therein (quadrupole and hexadecapole). Calculation of atomic multipoles makes use of a Np Γ_5 wavefunction that is fixed by spatial symmetry, D_{3d}, and Np electron configuration, $^4I_{9/2}$, alone [5]. A discussion of findings and related works appears in section 6. An appendix is devoted to implications for multipoles of symmetry operations in the magnetic point groups.

2. Implications of crystal symmetry

An atomic multipole is denoted by $\langle T^K_Q\rangle$ with rank K a positive integer and projection Q ($-K \le Q \le K$). Angular brackets denote the ground-state expectation value of the enclosed spherical tensor operator, in this case calculated for the ground-state configuration $5f^3$ (Np^{4+}, $^4I_{9/2}$). We use only parity-even multipoles because the resonant ion, Np, is at a centre of inversion symmetry in $Pn\bar{3}m$ (#224). With origin choice 2 site symmetry $\bar{3}m$ (D_{3d}) is at the origin. Multipoles possess a time signature $(-1)^K$ and the complex conjugate $\langle T^K_Q\rangle^* = (-1)^Q\langle T^K_{-Q}\rangle = \langle T^K_Q\rangle' - \mathrm{i}\langle T^K_Q\rangle''$ with $\langle T^K_0\rangle$ purely real.

We choose the origin as our reference site, with a triad axis of rotation symmetry along the crystal axis [111] and a diad axis of rotation symmetry along the diagonal [1, −1, 0]. To implement a triad axis of symmetry along an oblique axis it is convenient to use local, principal axes $\boldsymbol{\xi} = [-1, -1, 2]/\sqrt{6}$, $\boldsymbol{\eta} = [1, -1, 0]/\sqrt{2}$, and $\boldsymbol{\zeta} = [1, 1, 1]/\sqrt{3}$ with corresponding multipoles $\langle O^K_q\rangle$ that also possess a time signature $(-1)^K$. Multipoles $\langle T^K_Q\rangle$ are referred to the crystal unit cell and

$$\langle T^K_Q\rangle = \exp(-\mathrm{i}3\pi Q/4)\sum_q d^K_{q,Q}(\beta)\langle O^K_q\rangle, \qquad (2.1)$$

and $d^K_{q,Q}(\beta)$ an element of the Wigner rotation matrix using $\cos\beta = 1/\sqrt{3}$ and $\sin\beta = \sqrt{(2/3)}$. The triad axis of rotation symmetry requires $C_{3\zeta}\langle O^K_q\rangle = \langle O^K_q\rangle = \exp(\mathrm{i}2\pi q/3)\langle O^K_q\rangle$ which is satisfied by $q = \pm 3m$. A diad axis of rotation symmetry in D_{3d} parallel to the $\boldsymbol{\eta}$ axis imposes the identity $C_{2\eta}\langle O^K_q\rangle = \langle O^K_q\rangle = (-1)^{K+q}\langle O^K_{-q}\rangle$. Using the latter property of $\langle O^K_q\rangle$ and $q = \pm 3m$ in (2.1) it is easy to confirm that $\langle T^K_Q\rangle$ is indeed unchanged by the diad operations $C_2[1\bar{1}0]$ and $C_2[01\bar{1}]$.

Since $\langle O^K_q\rangle = (-1)^K\langle O^K_q\rangle^*$ it follows that $\langle O^K_0\rangle = 0$ for K odd (magnetic), and $\langle O^K_q\rangle$ is purely real (imaginary) for K even (odd). The result $\langle T^1_Q\rangle = 0$ follows from (2.1) and $\langle O^1_0\rangle = 0$. Directly from (2.1)

$$\langle T^K_Q\rangle^* = \exp(\mathrm{i}3\pi Q/2)(-1)^K\langle T^K_Q\rangle, \qquad (2.2)$$

which tells us that $\langle T^K_0\rangle = 0$ for K odd, in keeping with $\langle O^K_0\rangle$. For later use

$$\langle T^K_{+2}\rangle^* = (-1)^{K+1}\langle T^K_{+2}\rangle, \qquad (2.3)$$

and multipoles $\langle T^K_{+2}\rangle$ with K odd purely real and K even purely imaginary. Taking $K = 3$ (octupole) and 5 (triakontadipole) in (2.1) leads to the results $\langle T^3_{+2}\rangle = -\mathrm{i}\langle O^3_{+3}\rangle/\sqrt{3}$ and $\langle T^5_{+2}\rangle = \mathrm{i}\langle O^5_{+3}\rangle/\sqrt{3}$, and indeed these multipoles are purely real given $\langle O^K_q\rangle$ is purely imaginary for K odd. Results $d^2_{0,0}(\beta) = 0$ and $d^5_{3,4}(\beta) + d^5_{-3,4}(\beta) = 0$ yield $\langle T^2_0\rangle = 0$ and $\langle T^5_{\pm 4}\rangle = 0$.

The four Np ions are at sites 4b in the space group (#224, origin choice 2). Positions in a unit cell are $\mathbf{d} = (0, 0, 0)$, $(\frac{1}{2}, \frac{1}{2}, 0)$, $(\frac{1}{2}, 0, \frac{1}{2})$, $(0, \frac{1}{2}, \frac{1}{2})$ with environments related by operations $C_2[001]$, $C_2[010]$ and $C_2[100]$ with respect to (0, 0, 0). For a super-lattice reflection $(00L)$ with Miller index L an odd integer, our structure factor is

$$\Psi_{K,Q} = \sum_d \exp(\mathrm{i}\mathbf{d}\cdot\mathbf{k})\langle T^K_Q\rangle_d$$
$$= [1 + (-1)^Q][\langle T^K_Q\rangle - (-1)^K\langle T^K_{-Q}\rangle], \qquad (2.4)$$

where $\mathbf{k} \equiv$ $(00L)$ is the Bragg wavevector. Evidently, $\Psi_{K,Q}$ can only be different from zero for Q even. The motif of magnetic (time-odd) multipoles coincides with the chemical structure and it is identical to portraits of Np multipoles displayed by Magnani *et al* [2] and Santini *et al* [3] with Γ_5 symmetry. Note that $\Psi_{K,0} = 0$ for all K. The result $\Psi_{K,0} = 0$ for K even is anticipated, because L odd is a space-group forbidden reflection, while $\Psi_{K,0} = 0$ for K odd follows from the identity $\langle T^K_0\rangle = 0$ for K odd. Bulk properties of Np ions, including dichroic signals, are calculated from a structure factor with $\mathbf{k} \equiv$ (000) that can be different from zero for K even and $Q = 0$, namely

$$\Psi_{K,Q} = [1 + (-1)^Q][\langle T^K_Q\rangle + (-1)^K\langle T^K_{-Q}\rangle].$$

Although, like (2.4), only pure rotations, C_2, are used in its construction parity-odd dichroic signals for neptunium—natural circular and magneto-chiral signals—are forbidden because the appropriate point group contains a centre of inversion symmetry, which renders all parity-odd multipoles zero.

An $E1$–$E1$ resonant event contains tensors $K = 0$, 1 and 2. For these K all $\Psi_{K,Q}$ are zero other than $\Psi_{2,\pm2} = \pm4\mathrm{i}\langle T^2_{+2}\rangle''$, which creates Templeton–Templeton scattering. With absorption at $M_{4,5}$ edges ($3d_{3/2}$ and $3d_{5/2}$) and an $E1$–$E1$ event, multipoles contain electronic degrees of freedom within p and f states. All experimental data taken at the actinide $M_{4,5}$ edges indicate a very strong dominance of $3d_{3/2}$, $3d_{5/2} \leftrightarrow 5f$ processes [3]. Let us note for completeness that an $E2$–$E2$ event, for which $K = 0, \ldots, 4$, occurring at $M_{4,5}$ edges may sample electronic degrees of freedom within s, d and g states. Larger $E2$–$E2$ resonant contributions, however, are expected at the $M_{2,3}$ and $L_{2,3}$ edges where the quadrupole operator $E2$ directly couples to 5f states.

3. Unit-cell structure factors for resonant Bragg diffraction

A unit-cell structure factor is denoted by $F_{\mu'\nu}$, where μ' and ν label secondary and primary states of polarization. For an $E1$–$E1$ resonant event and a space-group forbidden reflection $(00L)$ with L odd only $\langle T^2_{+2}\rangle''$ contribute, so that

$$\begin{aligned} F(E1\text{–}E1)_{\mu'\nu} &= \sum_K \mathbf{X}_K(\mu'\nu)\cdot\boldsymbol{\Psi}_K \\ &= X_{2,2}(\mu'\nu)\Psi_{2,-2} + X_{2,-2}(\mu'\nu)\Psi_{2,2}, \end{aligned} \tag{3.1}$$

and the second equality follows because all $\Psi_{K,Q}$ are zero apart from $\Psi_{2,\pm2}$. Using appropriate values for $X_{2,\pm2}(\mu'\nu)$ we find [7, 8]

$$\begin{aligned} F(E1\text{–}E1)_{\sigma'\sigma} &= 4\langle T^2_{+2}\rangle'' \sin(2\psi), \\ F(E1\text{–}E1)_{\pi'\sigma} &= 4\langle T^2_{+2}\rangle'' \sin\theta\cos(2\psi), \end{aligned} \tag{3.2}$$

where θ is the Bragg angle and ψ the azimuthal angle, i.e. the angle of rotation of the crystal about the Bragg wavevector. For $\psi = 0$ the crystal **a** axis is in the plane of scattering and normal to σ polarization. Dependences on θ and ψ displayed in (3.2) are the same as in corresponding expressions used successfully by Paixão *et al* [1] to analyse their data. Identification of the strength of observed signals with a quadrupole, $\langle T^2_{+2}\rangle''$, was made later [4].

Two features of structure factors for an $E2$–$E2$ event merit comment. First, dependence of structure factors on ψ in both $E1$–$E1$ and $E2$–$E2$ are the same. The second feature is a magnetic (time-odd) contribution, $\langle T^3_{+2}\rangle'$, in the rotated channel of scattering. As in the calculation of structure factors for an $E1$–$E1$ event, the identity $\Psi_{K,Q} = -(-1)^K\Psi_{K,-Q}$ derived from (2.4) with Q even is a crucial factor in determining explicit $E2$–$E2$ structure factors. In general, there are many contributions to $E2$–$E2$ structure factors and there is a good case to exploit universal forms that include the dependence on azimuthal angle [8]. We go on to find

$$\begin{aligned} F(E2\text{–}E2)_{\sigma'\sigma} &= (2/\sqrt{7})\sin^2\theta\sin(2\psi) \\ &\quad\times[\sqrt{3}\langle T^2_{+2}\rangle'' - 2\langle T^4_{+2}\rangle''], \\ F(E2\text{–}E2)_{\pi'\sigma} &= (2/\sqrt{7})\sin\theta\cos(2\psi) \\ &\quad\times[-\sqrt{3}(1+2\cos2\theta)\langle T^2_{+2}\rangle'' + \mathrm{i}\sqrt{21}\cos^2\theta\langle T^3_{+2}\rangle' \\ &\quad-(1+\sin^2\theta)\langle T^4_{+2}\rangle'']. \end{aligned} \tag{3.3}$$

Note the very different dependences on the Bragg angle in (3.2) and (3.3). Paixão *et al* [1] make the remark that their data shows no evidence of an $E2$–$E2$ event, which if present would likely contribute at a photon energy less than the $E1$–$E1$ event.

A magnetic octupole ($K = 3$) was proposed as the primary order parameter [3, 5] as $K = 3$ is the lowest allowed rank after the (apparently forbidden) dipole. This is contested, however, by numerical estimates using a first-principles theory that includes spin–orbit coupling and hybridization with oxygen ions [6]. Instead, the authors of [6] favour a Γ_5 triakontadipole ($K = 5$) on the grounds of its relatively large magnitude in their theory.

4. Multipoles

In this section we outline how atomic multipoles arise in resonant scattering, without recourse to rigorous proofs of statements that require extensive (Racah) algebra [9–11]. We use an $E1$–$E1$ event for this purpose.

In the present discussion, the resonant part of the x-ray scattering length may be taken to be

$$G_{\mu'\nu} = \sum_\eta \langle R_{\mu'}|\eta\rangle\,\langle\eta|R_\nu\rangle(\Delta_\eta/[E - \Delta_\eta + \mathrm{i}\Gamma_\eta]). \tag{4.1}$$

Here, **R** is the dipole operator, E the primary photon energy, $\Delta_\eta \geq 0$ the energy of a resonance and $\hbar/\Gamma_\eta$ the lifetime of a virtual, intermediate core-state.

The quantum label η in (4.1) includes the total angular momentum and projection of the intermediate core-state, J_c, M_c. The expectation value $\langle R_{\mu'}|\eta\rangle\,\langle\eta|R_\nu\rangle$ is constructed with matrix elements of the type $\langle J_\mathrm{c},\ M_\mathrm{c}|R_\nu|J, M\rangle$ proportional to a Clebsch–Gordan coefficient $(J_\mathrm{c}\ M_\mathrm{c}\ J\ M|1\nu)$ with $\nu = 0, \pm1$ (Wigner–Eckart theorem). The coefficient of proportionality, called a reduced matrix element (RME), is complex and depends on all quantum numbers apart from projections M_c, M. The Clebsch–Gordan coefficient $(J_\mathrm{c}\ M_\mathrm{c}\ J\ M\ |1\nu)$ is the signature of a spherical tensor, in this case a spherical component of **R**. Evidently, the numerator $\langle R_{\mu'}|\eta\rangle\,\langle\eta|R_\nu\rangle$ in (4.1) contains products $(J_\mathrm{c}\ M_\mathrm{c}\ J'\ M'|1\mu')(J_\mathrm{c}\ M_\mathrm{c}\ J\ M|1\nu)$. This product can be shown to be equal to a sum on integer x of Clebsch–Gordan coefficients $(J\,M\,J'\,M'|xq)$; see, for example, section 9.6 [12], i.e. a product of two suitable Clebsch–Gordan coefficients can be represented by a sum of spherical tensors of rank x, which we denote by Υ^x_q. In the final analysis $\langle R_{\mu'}|\eta\rangle\,\langle\eta|R_\nu\rangle$ is a sum of multipoles $\langle\Upsilon^x_q\rangle$. These multipoles are equivalent to $\langle T^K_q\rangle$ used in section 2, by which we mean that the two types of multipoles, $\langle T^K_q\rangle$ and $\langle\Upsilon^x_q\rangle$, only differ by virtue of RMEs that depend on J_c. In particular, (2.1) applies to both types of multipole.

There are generally many values of x, more than the three values of K in the tensor product:

$$\sum_{\mu',\nu}\langle R_{\mu'}|\eta\rangle\,\langle\eta|R_\nu\rangle(1\mu'1\nu|Kq) = \sum_x \Phi_\eta(K,x)\langle\Upsilon^x_q\rangle, \tag{4.2}$$

where $\Phi_\eta(K,x)$ is purely real and it stands for a lengthy quantity which contains, among other things, M_c and various

RMEs [10, 11]. Hence, the scattering length for resonant Bragg diffraction, and dichroic signals, may contain atomic multipoles, $\langle \Upsilon^x_q \rangle$, with rank x larger than the rank K in unit-cell structure factors, meaning the scope of resonant scattering to investigate ground-state electronic structure is actually greater than meets the eye.

An important property of $\Phi_\eta(K, x)$ is that the sum $\sum_{Mc} \Phi_\eta(K, x)$ vanishes unless $x = K$. Such a sum is justified when angular anisotropy of the core-state is negligible. In this instance, the scattering length (4.1) reduces to oscillators labelled by J_c, and the expression is adequate for a successful analysis of data, in most cases.

We end the section, intentionally bereft of algebraic detail, with a reminder that foregoing statements can be proved and that there are explicit expressions for all quantities [9–11]. For example, in section 5 we give specific values of $\langle \Upsilon^x_q \rangle$ which enter $E1$–$E1$ structure factors. The values are obtained using a neptunium wavefunction derived in independent investigations. In other cases, multipoles can be estimated by fitting expressions to experimental data.

5. Energy profile

As noted in section 4, structure factors (3.2) are appropriate if the observed energy profile is adequately represented by a Lorentzian function of the primary energy—derived from a simple oscillator. But Paixão *et al* [1] emphasize that, at the M_4 edge of Np, the observed energy profile is far better represented by the square of a Lorentzian function. Such an energy profile is found to be a natural outcome of the angular anisotropy of a 3d core-state. By which we mean that the M_4 core-state must be labelled by the full set of quantum labels, $J_c = \frac{3}{2}$ and $M_c (-J_c \le M_c \le J_c)$, and, consequently, four oscillators.

Following (4.1), the $E1$–$E1$ scattering length in the vicinity of a resonance at energy Δ is

$$G(E1\text{–}E1) = \frac{\sum_{Mc} \left[\sum_x \Phi_\eta(2, x) \langle \Upsilon^x_{+2} \rangle'' \right]}{[E - \Delta - \varepsilon(M_c) + i\Gamma]}, \qquad (5.1)$$

and the corresponding energy profile:

$$I = |G(E1\text{–}E1)|^2. \qquad (5.2)$$

In (5.1), $\varepsilon(M_c) = M_c(g - 1)H_s$, where $g = 4/5$ is the Landé factor and H_s simulates a magnetic exchange field [18]. Independent evidence for the pivotal importance of an intra-atomic, magnetic exchange interaction between 3d core and 5f valence shells, in the form of *ab initio* calculations of the Np x-ray absorption spectra that include non-zero integrals G_1, G_3 and G_5, is reported in [4]. Also significant in the question of a magnetic exchange field is net spin polarization in the 5f electrons on a Np ion along the [111] axis obtained in a first-principles theory of magnetic multipolar order in neptunium dioxide; [6] and figure 3(b) therein. A case for Zeeman, $M_c g H_o$, in place of exchange energy is made in work on dysprosium borocarbide [13, 14]. While it is argued that an exchange field is correct, actually the two forms of energy are not distinguishable in an analysis at a single edge, here M_4 ($J_c = \frac{3}{2}$), although they do lead to different findings in a comparative study of two edges, say, $M_{4,5}$ [13, 14]. Returning to (5.1), when the exchange energy $\varepsilon(M_c)$ is set aside the sum on M_c can be accomplished and, using the aforementioned property of $\Phi_\eta(K, x)$, the numerator is proportional to $\langle \Upsilon^2_{+2} \rangle'' \equiv \langle T^2_{+2} \rangle''$.

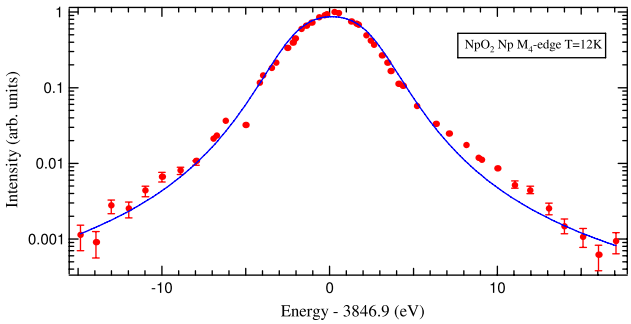

Figure 1. Intensity $I = |G(E1\text{–}E1)|^2$ for $J_c = \frac{3}{2}$ as a function of energy. Parameters in the scattering length $G(E1\text{–}E1)$ equation (5.1), the width in energy and exchange energy, are inferred from a fit to data [1] with the results $\Gamma = 2.60 \pm 0.07$ eV and $|\varepsilon(\frac{1}{2})| = 0.76 \pm 0.02$ eV. Multipoles in the scattering length, $\langle \Upsilon^2_{+2} \rangle''$ and $\langle \Upsilon^4_{+2} \rangle''$, are completely determined by a calculated Γ_5 wavefunction [5] that is fixed by the spatial symmetry D_{3d} and Np electron configuration, $^4I_{9/2}$, alone.

The sum of $\langle \Upsilon^x_{+2} \rangle''$ in (5.1) has the maximum rank $x = 2J_c + K = 5$. Of these multipoles those with x odd (magnetic) do not contribute because they are purely real, and $x = 0$ is excluded because the required projection >0. Thus the numerator is a simple linear combination of an octupole ($x = 2$) and a hexadecapole ($x = 4$) and, also, it is an even function of M_c. We find, apart from an unimportant scale factor,

$$\sum_x \Phi_\eta(2, x) \langle \Upsilon^x_{+2} \rangle'' = [-(9/5) \langle \Upsilon^2_{+2} \rangle'' + (258/\sqrt{65}) \langle \Upsilon^4_{+2} \rangle''], \qquad (5.3)$$

for $M_c = \pm\frac{1}{2}$ and

$$\sum_x \Phi_\eta(2, x) \langle \Upsilon^x_{+2} \rangle'' = -[\langle \Upsilon^2_{+2} \rangle'' + (258/\sqrt{65}) \langle \Upsilon^4_{+2} \rangle''], \qquad (5.4)$$

for $M_c = \pm\frac{3}{2}$. Use is made of entries in table 1 of [4] in arriving at these results, which are valid for $J_c = \frac{3}{2}$. As promised, the sum of the two numerators, (5.3) and (5.4), does not contain $\langle \Upsilon^4_{+2} \rangle''$.

Opposite signs attached to $\langle \Upsilon^4_{+2} \rangle''$ in (5.3) and (5.4) enable an energy profile that is close to the square of a Lorentzian and an excellent match to the observed energy profile, as can be seen in figure 1 which displays our calculated I and published data [1]. To see how this comes about, note that relative contributions to the amplitude from denominators $[E - \Delta \pm \varepsilon(\frac{1}{2}) + i\Gamma]^{-1}$ and $[E - \Delta \pm \varepsilon(\frac{3}{2}) + i\Gamma]^{-1}$ are controlled by $\Re = [1 + (258/\sqrt{65}) \langle \Upsilon^4_{+2} \rangle'' / \langle \Upsilon^2_{+2} \rangle'']/[(9/5) - (258/\sqrt{65}) \langle \Upsilon^4_{+2} \rangle'' / \langle \Upsilon^2_{+2} \rangle'']$. For $|(E - \Delta)| \gg \varepsilon(M_c), \Gamma$ the scattering length (5.1) is proportional to $(1 + \Re)/(E - \Delta)$ and for $\Re = -1$ the energy profile (5.2) departs from a Lorentzian

centred around Δ, being a much narrower function of E for given $\varepsilon(M_c)$, Γ. This conclusion is independent of the specific form of $\varepsilon(M_c)$ other than $\varepsilon(\frac{1}{2}) \neq \varepsilon(\frac{3}{2})$.

Values of $\langle \Upsilon^2_{+2} \rangle''$ and $\langle \Upsilon^4_{+2} \rangle''$ are calculated using expressions obtained from (2.1) with $\langle O^K_q \rangle$ derived from an appropriate wavefunction. First

$$\begin{aligned} \langle \Upsilon^2_{+2} \rangle &= (\mathrm{i}/\sqrt{6}) \langle O^2_0 \rangle, \qquad \text{and} \\ \langle \Upsilon^4_{+2} \rangle &= (\mathrm{i}/9)[\sqrt{10} \langle O^4_0 \rangle - \sqrt{7} \langle O^4_{+3} \rangle]. \end{aligned} \tag{5.5}$$

We make use of the Γ_5 wavefunction provided by Di Matteo *et al* [5] to calculate $\langle O^K_q \rangle$ (equation (1) in [5]). The precise form of the normalized wavefunction is determined by symmetry alone and there are no adjustable parameters. To be successful in this exercise it is vitally important that we adopt the same principal axes as these authors [5], and we go on to find

$$\begin{aligned} \langle O^2_0 \rangle = \tfrac{3}{2}\sqrt{(3/55)}, \qquad \langle O^4_0 \rangle = (5/3)\sqrt{(1/715)}, \\ \langle O^4_{+3} \rangle = -(2/15)\sqrt{(14/143)}. \end{aligned} \tag{5.6}$$

With these results $(258/\sqrt{65})\langle \Upsilon^4_{+2} \rangle'' / \langle \Upsilon^2_{+2} \rangle'' = 172/3$ and $\mathfrak{R} = -1.050$.

The energy profile (5.2) evaluated with $\mathfrak{R} = -1.050$ has been successfully confronted with data reported by Paixão *et al* [1]. In the fit to data shown in figure 1 we find $\Gamma = 2.60 \pm 0.07$ eV and $|\varepsilon(\frac{1}{2})| = 0.76 \pm 0.02$ eV, and these values for the width in energy and exchange energy are satisfactorily close to the values reported by Lovesey *et al* [4]. Moreover, Nagao and Igarashi estimate $\Gamma \approx 2$ eV [17].

6. Discussion

We re-visited a previous interpretation of observations, made with resonant Bragg diffraction of x-rays, of an unusual phase transition in the actinide compound NpO_2 [1]. Shortcomings in our original work [4] are removed and more recent knowledge about the neptunium wavefunction included, which culminates in a successful confrontation between our simulation and published data on the energy profile at the Np M_4 edge. Whereas previously the wavefunction was modelled in the current work a Γ_5 wavefunction is completely specified [5]. As a consequence, all atomic multipoles are fully determined. Our success in describing the observed energy profile adds confidence to the merit of the wavefunction. Two unknowns in the energy dependence, the width in energy and exchange energy, are inferred from data and they are found to be entirely reasonable and satisfactorily close to previous estimates [4, 17]. Our attention to the departure of the energy profile from a usual Lorentzian centred on the absorption edge, and identification of the departure with the Np hexadecapole, contrasts with the stance of Nagao and Igarashi who deem the departure unimportant [17].

A ratio of multipoles controls the shape of the energy profile, in particular its departure from a Lorentzian. This ratio is a rational number derived from the Γ_5 wavefunction, while irrational numbers abound at intermediate stages of the calculations of the controlling multipoles. This finding implies that all aspects of our calculation, which include fractional parentage coefficients for f^3 (Np^{4+}) and the Γ_5 wavefunction, are correct and the ratio is ultimately fixed by underlying symmetries.

The same basic atomic theory of resonant scattering of x-rays, used here to interpret diffraction data gathered on the low-temperature phase of neptunium dioxide at the Np M_4 edge (3846.9 eV), has been applied with equal success to interpretations of diffraction data gathered on rare-earth compounds with combined magnetic and orbitally ordered phases. Mulders and collaborators [13–15] report three studies of soft x-ray resonant Bragg diffraction at $M_{4,5}$ edges of Dy and Ho in borocarbides (DyB_2C_2 and HoB_2C_2) and extract good estimates of high-order rare-earth multipoles, e.g. the Dy triakontadipole [14]. These studies include intra-atomic magnetic and also quadrupolar interactions between 3d core and 4f valence shells. Confirmation of the contribution of these interactions to absorption spectra of rare-earth ions is given by Fernández-Rodríguez *et al* [16] using *ab initio* calculations.

Acknowledgments

One of us (SWL) has benefited from correspondence and discussions with E Balcar, J Jensen, K S Knight, A M Mulders, U Staub and G van der Laan. AR-F received financial support from the Gobierno del Principado de Asturias from Plan de Ciencia, Tecnología e innovación (PTCI) de Asturias, program 'Severo Ochoa', as well as, from the Spanish FEDER-MiCiNN grant no. MAT2011-27573-C04-02.

Appendix

We examine implications for neptunium multipoles of symmetry operations in the possible magnetic space groups of neptunium dioxide. Specific examples of multipoles are chosen by their relevance to the main text, i.e. the maximum rank is $K = 5$. Previous studies of multipoles of a similar nature include dysprosium borocarbide (DyB_2C_2) [19] and strontium iridate (Sr_2IrO_4) [20].

Three magnetic groups are constructed by the addition of the time reversal operator, θ, to the non-magnetic, crystallographic point group $\bar{3}m$ (D_{3d}), namely $\bar{3}m'$, $\bar{3}'m'$ and $\bar{3}'m$. Principal axes (ξ, η, ζ) are defined in section 2. Operators needed here and not found in section 2 are the identity, E, inversion, I, rotation–inversion (improper rotation), $\bar{3} \equiv S_6$, and a mirror normal to the η axis, $m_\eta = IC_{2\eta}$:

$$\begin{aligned} \bar{3}m &= \mathrm{D_{3d}}\colon \{E, 2C_{3\zeta}, 3C_{2\eta}, I, 2S_{6\zeta}, 3m_\eta\}, \\ \bar{3}m' &= \mathrm{D_{3d}(S_6)}\colon \{E, 2C_{3\zeta}, 3\theta C_{2\eta}, I, 2S_{6\zeta}, 3\theta m_\eta\}, \\ \bar{3}'m' &= \mathrm{D_{3d}(D_3)}\colon \{E, 2C_{3\zeta}, 3C_{2\eta}, \theta I, 2\theta S_{6\zeta}, 3\theta m_\eta\}, \\ \bar{3}'m &= \mathrm{D_{3d}(C_{3v})}\colon \{E, 2C_{3\zeta}, 3\theta C_{2\eta}, \theta I, 2\theta S_{6\zeta}, 3m_\eta\}. \end{aligned} \tag{A.1}$$

Since the point group can be generated by three symmetry operations, chosen in (A.1) to be I, $C_{2\eta}$ and $C_{3\zeta}$, all selection rules on multipoles can be derived by application of the

chosen operators or the corresponding composite operators $(\theta I, \theta C_{2\eta})$. The generic parity-even multipole is denoted by $\langle O_q^K \rangle$, which is prevalent in the text, and it has a time signature $(-1)^K$. (The corresponding multipole referred to crystal axes is denoted in the text by $\langle T_Q^K \rangle$.) In addition, we need a magnetoelectric multipole, $\langle G_q^K \rangle$, that is defined to be time-odd and parity-odd, and thus unchanged (even or gerade) by the composite operator θI.

$\bar{3}\mathbf{m}$; By definition the multipole $\langle O_q^K \rangle$ satisfies the identity $I\langle O_q^K \rangle = \langle O_q^K \rangle$. The triad axis of rotation symmetry imposes an identity

$$C_{3\zeta}\langle O_q^K \rangle = \exp(\mathrm{i}2\pi q/3)\langle O_q^K \rangle = \langle O_q^K \rangle, \qquad (A.2)$$

satisfied by $q = \pm 3m$ with m and integer, i.e. $|q|$ can take even and odd integer values that are multiples of 3. Lastly, to satisfy the diad axis of rotation symmetry

$$C_{2\eta}\langle O_q^K \rangle = (-1)^{K+q}\langle O_{-q}^K \rangle = (-1)^K \langle O_q^K \rangle^* = \langle O_q^K \rangle, \qquad (A.3)$$

where the second equality uses our definition of the complex conjugate of a multipole, $\langle O_q^K \rangle^* = (-1)^q \langle O_{-q}^K \rangle$. Evidently $\langle O_0^K \rangle = 0$ for K odd, while $\langle O_q^K \rangle$ is purely real (imaginary) for K even (odd).

In view of the time signature $(-1)^K$ the multipole $\langle O_q^1 \rangle$ represents a magnetic dipole. We find $\langle O_0^1 \rangle = 0$ and the projection $q = 0$ is the only allowed value for $K = 1$. All possible components of a magnetic dipole are therefore forbidden, $\langle T_Q^1 \rangle = 0$ for all Q. Continuing with time-odd multipoles, allowed octupoles ($K = 3$) are $\langle O_{-3}^3 \rangle = \langle O_3^3 \rangle$ which are purely imaginary; next, triakontadipoles ($K = 5$) $\langle O_{-3}^5 \rangle = \langle O_3^5 \rangle$ also purely imaginary. Regarding time-even multipoles, K even, a monopole $\langle O_0^0 \rangle$, quadrupole $\langle O_0^2 \rangle$ and hexadecapoles with components $\langle O_0^4 \rangle$ and $\langle O_3^4 \rangle = -\langle O_{-3}^4 \rangle$ are all purely real. The triakontadipole shown by Magnani *et al* [2] in figure 1 is invariant under $C_{2\eta}$ and thus clearly belongs to the magnetic group $\bar{3}m$.

$\bar{3}\mathbf{m}'$; All multipoles are parity even, with time signature $(-1)^K$, and must satisfy (A.2). In place of (A.3), a new identity arises from time reversal in union with a diad on the η axis, namely

$$\theta C_{2\eta}\langle O_q^K \rangle = (-1)^q \langle O_{-q}^K \rangle = \langle O_q^K \rangle^* = \langle O_q^K \rangle, \qquad (A.4)$$

and all allowed multipoles are purely real. In particular, a magnetic dipole $\langle O_0^1 \rangle$ is allowed in $\bar{3}m'$, while it is forbidden in $\bar{3}m$, and similar comments hold for the diagonal, magnetic multipoles $\langle O_0^3 \rangle$ and $\langle O_0^5 \rangle$, while $\langle O_{-3}^3 \rangle = -\langle O_3^3 \rangle$ and $\langle O_{-3}^5 \rangle = -\langle O_3^5 \rangle$.

To date, there is no empirical evidence in favour of magnetic dipoles in neptunium dioxide. As a consequence, we reject $\bar{3}m'$ as a candidate magnetic space group for the compound.

The remaining two magnetic point groups, $\bar{3}'m'$ and $\bar{3}'m$, are distinguished from previous point groups by the admittance of time reversal in union with the inversion of space coordinates, θI, under which magnetoelectric multipoles $\langle G_q^K \rangle$ are invariant. Finite magnetoelectric multipoles $\langle G_q^K \rangle$ for neptunium dioxide are non-commonsensical, of course. While in subsequent working we discover that they are allowed in magnetic groups $\bar{3}'m'$ and $\bar{3}'m$ all $\langle G_q^K \rangle$ are nominally zero because associated matrix elements are zero. We expand on this latter statement before proposing a mechanism that may break the embargo. Our notation is that used in section 4.

Operator equivalents for the magnetoelectric scalar (magnetic charge) and dipole (anapole) are $\mathbf{S}\cdot\mathbf{R}$ and $\mathbf{S}\times\mathbf{R}$, respectively. Here, $\mathbf{S}$ and $\mathbf{R}$ are, respectively, commuting spin and dipole (position) operators. Consider multipoles $\langle \boldsymbol{G}^0 \rangle = \langle \mathbf{S}\cdot\mathbf{R} \rangle$ and $\langle \boldsymbol{G}^1 \rangle = \langle \mathbf{S}\times\mathbf{R} \rangle$. An expectation value $\langle \cdots \rangle$ is made with matrix elements of respective operator equivalents using $S-L$ states $|s, \sigma\rangle$ and $|l, m\rangle$, where $\sigma = \pm\frac{1}{2}$ and $-l \le m \le l$. Consider a typical matrix element:

$$(\langle s, \sigma'|\langle l', m'|)S_p R_q(|s, \sigma\rangle\,|l, m\rangle) = \langle s, \sigma'|S_p|s, \sigma\rangle \times \langle l', m'|R_q|l, m\rangle,$$

where spherical components of the dipole operators are $p, q = 0, \pm 1$. The matrix element $\langle l', m'|R_q|l, m\rangle$ can be different from zero for $l + l'$ odd, since the RME is proportional to a Clebsch–Gordan coefficient $= (l'010|l0)$. But states with $l+l'$ odd are forbidden in a centrosymmetric environment. Such is the case for the example in hand, D_{3d}.

In conclusion, parity-odd multipoles can be different from zero in a parity-odd environment that supports an admixture of states with opposing parities, $l \neq l'$. Thus, when the environment is centrosymmetric, e.g. D_{3d}, and some $\langle \boldsymbol{G}^K \rangle$ are found non-zero a mechanism is afoot that negates the selection rule imposed by spatial inversion symmetry.

A scenario is a boot-strap mechanism on the lines of Trammell's model of magnetic dipoles in rare-earth ions possessed of a ground state that is nominally magnetically inert [21, 22]. Thereby a dipole moment is generated in a self-consistent theory via intervention of a Heisenberg exchange interaction in the Hamiltonian, which creates an admixture of states capable of supporting magnetism. In a similar situation, should the magnetic group permit $\langle \boldsymbol{G}^K \rangle$ then an interaction in the Hamiltonian proportional to $\boldsymbol{G}^K$ is invoked.

For the moment, the nature of a suitable symmetry-breaking interaction is unknown. Furthermore, breaking inversion symmetry at the Np site would either break cubic symmetry or reduce the space group from $Pn\bar{3}m$ to $P23$ (#195) or $P4_232$ (#208). Such a lowering of symmetry is not supported by any experimental observations—there are no signs of any lattice distortion, nor of conventional Bragg diffraction at reflections (HKL) with Miller indices $H+K+L$ odd. Therefore, it is reasonable to assume that inversion symmetry prevails and all magnetoelectric multipoles vanish, $\langle \boldsymbol{G}^K \rangle = 0$. Even so, desire for completeness compels us to list conditions on $\langle \boldsymbol{G}^K \rangle$ in $\bar{3}'m'$ and $\bar{3}'m$.

$\bar{3}'\mathbf{m}'$; Reference to (A.1) shows that (A.2) remains in force with $q = \pm 3m$. A conventional interpretation of the group, using parity-even multipoles, yields $\theta I\langle O_q^K \rangle = (-1)^K \langle O_q^K \rangle = \langle O_q^K \rangle$ which is satisfied by K even (non-magnetic), and the diad operation (A.3) is satisfied by $\langle O_q^K \rangle$ purely real. Turning to an interpretation using magnetoelectric multipoles $\langle G_q^K \rangle$, one has $q = \pm 3m$:

$$\theta I\langle G_q^K \rangle = -I\langle G_q^K \rangle = \langle G_q^K \rangle, \qquad (A.5)$$

that can be regarded as a definition and imposes no additional conditions, and in place of (A.3)

$$C_{2\eta}\langle G_q^K\rangle = (-1)^{K+q}\langle G_{-q}^K\rangle = (-1)^K\langle G_q^K\rangle^* = \langle G_q^K\rangle. \quad \text{(A.6)}$$

The last identity tells us that $\langle G_0^K\rangle = 0$ for K odd and $\langle G_q^K\rangle$ is purely real (imaginary) for K even (odd).

$\bar{3}'\mathbf{m}$; Parity-even multipoles, $\langle O_q^K\rangle$, must obey $(-1)^K = 1$, and hence conditions for these multipoles are identical to those in $\bar{3}'m'$. For magnetoelectric multipoles, $q = \pm 3m$, and invariance with respect to $\theta C_{2\eta}$ results in the identity

$$\theta C_{2\eta}\langle G_q^K\rangle = -(-1)^{K+q}\langle G_{-q}^K\rangle = -(-1)^K\langle G_q^K\rangle^* = \langle G_q^K\rangle. \quad \text{(A.7)}$$

The identity (A.7) tells us that $\langle G_0^K\rangle = 0$ for K even and $\langle G_q^K\rangle$ is purely real (imaginary) for K odd (even). Thus the anapole parallel to the ζ axis, $\langle G_0^1\rangle$, can be different from zero but $\langle G_{\pm 1}^1\rangle = 0$ because of the triad axis of rotation symmetry.

References

[1] Paixão J A *et al* 2002 *Phys. Rev. Lett.* **89** 187202
[2] Magnani N *et al* 2008 *Phys. Rev.* B **78** 104425
[3] Santini P *et al* 2009 *Rev. Mod. Phys.* **81** 807
[4] Lovesey S W *et al* 2003 *J. Phys.: Condens. Matter* **15** 4511
[5] Di Matteo S *et al* 2007 *J. Alloys Compounds* **444/445** 278
[6] Suzuki M-T *et al* 2010 *Phys. Rev.* B **82** 241103(R)
[7] Lovesey S W *et al* 2005 *Phys. Rep.* **411** 233
[8] Scagnoli V and Lovesey S W 2009 *Phys. Rev.* B **79** 035111
[9] Lovesey S W and Balcar E 1997 *J. Phys.: Condens. Matter* **9** 4237
[10] Lovesey S W 1997 *J. Phys.: Condens. Matter* **9** 7501
[11] Lovesey S W and Balcar E 2012 *J. Phys. Soc. Japan* **81** 014710
[12] Balcar E and Lovesey S W 2009 *Introduction to the Graphical Theory of Angular Momentum Springer Tracts in Modern Physics* vol 234 (Berlin: Springer)
[13] Mulders A M *et al* 2006 *J. Phys.: Condens. Matter* **18** 11195
[14] Princep A J *et al* 2011 *J. Phys.: Condens. Matter* **23** 266002
[15] Princep A J *et al* 2012 *J. Phys.: Condens. Matter* **24** 075602
[16] Fernández-Rodríguez J *et al* 2010 *J. Phys.: Condens. Matter* **22** 016001
[17] Nagao T and Igarashi J 2005 *Phys. Rev.* B **72** 174421
[18] van der Laan G 1997 *Phys. Rev.* B **55** 8086
[19] Lovesey S and Knight K S 2001 *Phys. Rev.* B **64** 094401
[20] Chapon L C and Lovesey S W 2011 *J. Phys.: Condens. Matter* **23** 252201
[21] Trammell G T 1963 *Phys. Rev.* **131** 932
[22] Houmann J G *et al* 1979 *Phys. Rev.* B **20** 1105

CHAPTER 5

Hematite, α-Fe_2O_3

Article II

Article in press in Physical Review B: "Parity-odd multipoles, magnetic charges and chirality in haematite (α–Fe_2O_3)".

Article III

Article in press in Physical Review B: "Chiral properties of haematite (α-Fe_2O_3) inferred from resonant Bragg diffraction using circularly polarized x-rays".

Abstract

The canted and collinear antiferromagnetic phases of Hematite (α–Fe_2O_3), were studied with linear polarization Resonant X-ray Diffraction near the iron K-edge. The experimental data collected at two forbidden reflections from the $(0,0,l)_H$ family in the R$\bar{3}$c space group, with l odd, were used to infer the values of the multipoles behind these orderings, showing a coupling between two processes, E1E2 and E2E2, for the linear polarization case. This mixture was theoretically demonstrated to be distinguishable by the use of circular polarized X-rays in the primary beam leading to an experiment that corroborated the values inferred in the previous studies together with the demonstration that the helicity from the X-rays can couple with the chiral properties of materials.

5.1 Results and Summary

The iron sesquioxide (α–Fe_2O_3) or Hematite, from the Greek "$\alpha\iota\mu\alpha\tau\iota\tau\eta\varsigma$", has been studied since old Greek times. Its structure from the Corundum family ($R\bar{3}c$, #167), allows an antiferromagnetic behaviour below a Néel temperature, T_N, of 950 K. It shows two different phases, one of each (above the temperature of Morin, $T_M \approx 250$ K) has the magnetic moments in a canted ordering in the ab-plane producing a weak ferromagnetic signal along the c-axis, this effect is due to the so-called Dzyaloshinskii-Moriya (DM) interaction, introduced in Appendix A. This interaction was first described by Dzyaloshinskii in 1958 [30] and Moriya [31] and it has been observed in many multiferroic materials as $BiFeO_3$ [12], $BFeO_3$ [11] and $Ba_{0.5}Sr_{1.5}Zn_2Fe_{12}O_{22}$ [79].

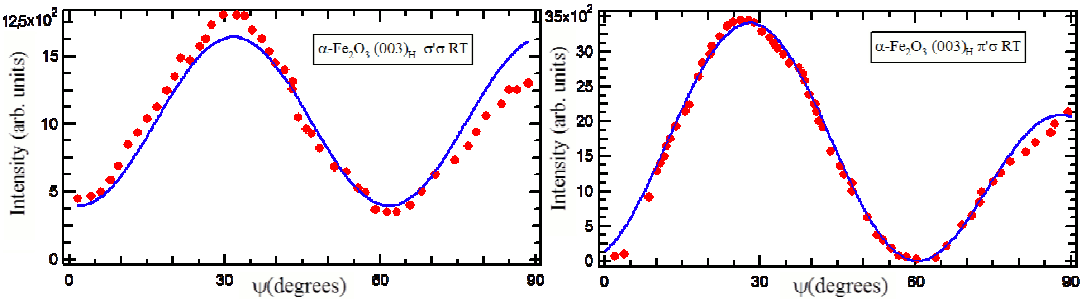

Figure 5.1. Azimuthal angle scan near the Fe K-edge at the forbidden reflection $(0,0,3)_H$. (Red dots) Experimental data presented by Finkelstein et al. [33] for the unrotated $(\sigma'\sigma)$ and rotated $(\pi'\sigma)$ polarization channels. (Blue line) Fitting to data obtained using the spherical tensor formalism presented in article II [80].

The first studies carried out in hematite using Resonant X-ray Scattering near the K-edge were performed by Finkelstein and co-workers in 1992 [33], this group investigated the forbidden reflection $(0,0,3)_H$ at 9 eV below the K-edge using a Si(311) polarization analyser to extract the σ and π contributions to scattering. The experimental data obtained in this experiment is presented in figure 5.1, where the blue line represent the fitting done using the formalism presented in section 2.4, in this case the value of the multipoles inferred are the same as the ones presented in the Article II [80].

Later on, Kokubun and collaborators [32] follow the steps and performed a more complete experiment to a single crystal of Hematite together with another analysis to a compound of the same space group chromium sesquioxide

(presented in Appendix G). Unfortunately, the azimuthal scans where gathered in this case without a polarization analyzer crystal for measuring the different contributions from the σ and π channels in the secondary beam. They collected the data at 7.112 keV just below the K-edge for two forbidden reflections $(0,0,3)_H$ and $(0,0,9)_H$ and treat the data using a theoretical approach based in an abridged amplitude by de Bergevin and Brunel [81], which is a sum of the exact expression and the high-energy limit of two contributions to scattering that involve intermediate states. This approximation is valid near the limit of high energy but not for the investigated interval of energy below the K-edge. The spherical multipole model presented in section 2.4 and in article II [80], is valid for the energy studied in the experiment done by Kokubun et al. [32] and in particular for the case were the energy profile can be approached by a single oscillator.

Kokubun and co-authors introduced a possible contribution of an E1M1 event to scattering in hematite as explanation of the non-resonant case; this event was also used by Scagnoli et al. [7] as the possible mechanism to describe superconductivity in the CuO family. In the case of Hematite the contribution of the E1M1 was shown not to be necessary for explaining the dependence with the azimuthal angle as presented in article II.

The linear polarized data showed a mixture of the two contributions E1E2 and E2E2, this lead us to question our self, if it was possible to differentiate between them using circular polarized light in the primary beam, as presented in $GaFeO_3$ by Collins and co-workers [3]. From this the theoretical calculations of the contribution to scattering were done for the two events (E1E2 and E2E2), and it was found a different dependence with the azimuthal angle, ψ.

In collaboration with the group from the beamline P09 at Petra III, Hamburg, a circular polarization x-ray resonant experiment for the two forbidden reflections, $(0,0,3)_H$ and $(0,0,9)_H$, was carried out in a large single crystal of hematite. Which was polished after the data collection, had the family of the $(0,0,l)_H$reflections perpendicular to the surface. The control of the beam polarization was done defining the Stokes parameters P_1 and P_3, for a set of diamond crystals that were playing a role of phase plates, for pure circular left and circular right primary beams (as defined in Appendix F) for both polarizations.

Figures 4 and 5 of the article III present the azimuthal dependence of the dichroic signal (C_R-C_L) for the two forbidden reflections studied below and above T_M. The values of the average multipoles fitting coincide with the ones obtained from applying the non-reducible tensor formalism described by spherical tensors to the data gathered by Kokubun et al. [32] but it is possible to observe how the canted phases can be fully described by the parity-even processes (E1E2) multipole, the Magnetoelectric contribution being the stronger event. While in the phase below T_M there is still a mixture between the pure and mixed events multipoles, E2E2 and E1E2 respectively.

5.2 Article II

Parity-odd multipoles, magnetic charges, and chirality in hematite α-Fe_2O_3

S. W. Lovesey
ISIS Facility & Diamond Light Source, Ltd., Oxfordshire OX11 0QX, United Kingdom

A. Rodríguez-Fernández and J. A. Blanco
Departamento de Física, Universidad de Oviedo, E–33007 Oviedo, Spain

(Received 8 October 2010; published 23 February 2011)

Collinear and canted magnetic motifs in hematite were investigated by J. Kokubun *et al.* [Phys. Rev. B **78**, 115112 (2008)] using x-ray Bragg diffraction magnified at the iron K-edge, and analyses of observations led to various potentially interesting conclusions. We demonstrate that the reported analyses for both nonresonant and resonant magnetic diffraction at low energies near the absorption K-edge are not appropriate. In its place, we apply a radically different formulation, thoroughly tried and tested, that incorporates all magnetic contributions to resonant x-ray diffraction allowed by the established chemical and magnetic structures. Essential to a correct formulation of diffraction by a magnetic crystal with resonant ions at sites that are not centers of inversion symmetry are parity-odd atomic multipoles, time-even (polar) and time-odd (magneto-electric), that arise from enhancement by the electric-dipole ($E1$)–electric-quadrupole ($E2$) event. Analyses of azimuthal-angle scans on two space-group forbidden reflections, hexagonal $(0,0,3)_h$ and $(0,0,9)_h$, collected by Kokubun *et al.* [Phys. Rev. B 78, 115112 (2008)] above and below the Morin temperature ($T_M = 250$ K), allow us to obtain good estimates of contributing polar and magnetoelectric multipoles, including the iron anapole. We show, beyond reasonable doubt, that available data are inconsistent with parity-even events only ($E1$-$E1$ and $E2$-$E2$). For future experiments, we show that chiral states of hematite couple to circular polarization and differentiate $E1$-$E2$ and $E2$-$E2$ events, while the collinear motif supports magnetic charges.

DOI: 10.1103/PhysRevB.83.054427 PACS number(s): 75.50.Ee, 78.70.Ck, 78.20.Ek, 75.47.Lx

I. INTRODUCTION

Enigmas about ichor-like hematite (α-Fe_2O_3) and famed lodestone, both true and some embroidered, have been worried and written about from the time of Greek texts in 315 BC to William Gilbert of Colchester, the father of magnetism, in the 16th century, to Dzyaloshinsky in 1958 who gave a phenomenological theory of weak ferromagnetism. Hematite is the iron sesquioxide that crystallizes into the corundum structure (centrosymmetric space group 167, $R\bar{3}c$) in which ferric (Fe^{3+}, $3d^5$) ions occupy sites 4(c) on the trigonal c axis that are not centers of inversion symmetry. For an extensive review of the history and properties of hematite see, for example, Morrish[1] and Catti *et al.*[2]

At room temperature, the motif of magnetic moments is canted antiferromagnetism with moments in a (basal) plane normal to the c axis. Weak ferromagnetism parallel to a diad axis of rotation symmetry, normal to a mirror plane of symmetry that contains the c axis, is created by a Dzyaloshinsky[3]–Moriya[4] antisymetric interaction $\mathbf{D} \cdot (\mathbf{S_1} \times \mathbf{S_2})$ between spins $\mathbf{S_1}$ and $\mathbf{S_2}$ and the vector $\mathbf{D}$ is parallel to the c axis. The Morin temperature 250 K, at which moments rotate out of the the basal plane to the c axis, may be determined from the temperature dependence of magnetic Bragg peaks observed by neutron diffraction. Rotation of the moments takes place in a range of 10 K in pure crystals but the interval can be much larger, ≈150 K, in mixed materials.[5] Ultimately, moments align with the c axis and create a fully compensating, collinear antiferromagnet with an iron magnetic moment of 4.9 μ_B at 77 K. We follow Dzyaloshinsky[3] and label collinear (low-temperature phase) and canted (room-temperature phase) antiferromagnetism as phases I and II, respectively (see Fig. 1). In phase I hematite is not magnetoelectric unlike eskolaite (Cr_2O_3), which also possesses the corundum structure and collinear antiferromagnetism.

Finkelstein *et al.*[6] and Kokubun *et al.*[7] studied hematite by x-ray Bragg diffraction, with Bragg intensities enhanced by tuning the energy of the primary x-rays to the iron K-absorption edge. In these experiments, attention is given to Bragg reflections that are forbidden by extinction rules for the space group. Often called Templeton and Templeton reflections,[8] the reflections in question are relatively weak and arise from angular anisotropy of valence states that accept the photoejected electron. Following rotation of the crystal about a Bragg wave-vector aligned with the c axis, Finkelstein *et al.*[6] observed a near sixfold periodicity of the intensity that is traced to a triad axis of rotation symmetry that passes through sites occupied by resonant, ferric ions. In general by measuring intensities, collected at space-forbidden reflections, we can obtain information of high-order multipoles existing in the materials such as magnetic charge (or magnetic monopole),[9] electric dipole,[10] anapole,[11,12] quadropole,[13] octupole,[14,15] and hexadecapole.[16,17] Therefore, these weak reflections are extremely sensitive to charge, orbital, and spin electron degrees of freedom and hematite is no exception.[18]

We apply an atomic theory of resonant Bragg diffraction formulated for the corundum structure[19] to data gathered by Kokubun *et al.*[7] at forbidden reflections $(0,0,l)_h$ with $l = 3(2n + 1)$ and infer from available data relative values of atomic multipoles of the resonant ion. A successful story emerges with scattering represented by a mixture of parity-even and parity-odd (even or odd with respect to the inversion of space) multipoles at sites in the structure

 ©2011 American Physical Society

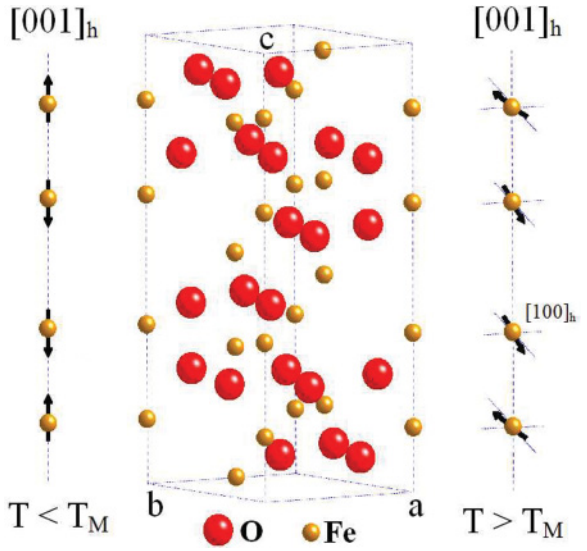

FIG. 1. (Color online) Magnetic and chemical structure of hematite, space group $R\bar{3}c$. The red (large) and the yellow (small) dots represent oxygen and iron sites, respectively. The left line denotes the magnetic motif along the c axis below the Morin temperature (phase I). The right line denotes the motif above the Morin temperature, where iron moments are contained in the a-b plane (phase II).

occupied by resonant iron ions, which are not centers of inversion symmetry. Parity-odd multipoles arise in a resonant event using the electric dipole ($E1$) and electric quadrupole ($E2$)—corresponding multipoles are labeled polar (time-even) or magnetoelectric (time-odd)—while parity-even multipoles arise from $E1$-$E1$ and $E2$-$E2$ events. A chiral state of hematite is demonstrated by a predicted coupling of resonant intensity to circular polarization (helicity) in the primary beam, and the effect also differentiates between $E1$-$E2$ and $E2$-$E2$ events. The two parity-odd multipoles of rank zero correspond to chirality and magnetic charge[20,21] and both pseudoscalar monopoles are present in the electric dipole–magnetic dipole ($E1$-$M1$) amplitude for resonant scattering by hematite in phase I.

Our article is arranged as follows. Section II contains essential information and definitions. Unit-cell structure factors for Bragg diffraction enhanced by $E1$-$E1$, $E1$-$E2$, and $E2$-$E2$ listed in the Appendix are exploited in Secs. III and IV, which report the successful analysis of Bragg diffraction data gathered on hematite at room temperature and at 150 K, well below the Morin transition. Thereafter, in Sec. V, there are simulations of resonant intensity induced by circular polarization in the primary x-ray beam which signals the existence of a chiral state. Section VI addresses the magnetic charge found in the $E1$-$M1$ structure factor and not visible in a dichroic signal. A discussion of findings in Sec. VII concludes the article.

II. BASICS

There are four contributions to the amplitude of photons scattered by electrons calculated in the first level of approximation in the small quantity (E/mc^2), where E is the energy of the primary photon, namely, Thomson scattering, spin scattering, and two contributions with virtual intermediate states, one of which may become large when E coincides with an atomic resonance. Of particular interest with magnetic samples is a celebrated reduction of the amplitude, derived by De Bergevin and Brunel,[22] which occurs at large E. In this limit, all three contributions excluding Thomson scattering add to give so-called magnetic, nonresonant scattering made up simply of spin and orbital magnetic moments. De Bergevin and Brunel's result is not valid at low energies, and certainly not below an atomic resonance, as is at once obvious from the steps in its derivation.[23]

In an analysis of x-ray Bragg diffraction data for hematite collected at space-group forbidden reflections we use the spin and resonant contributions to the scattering amplitude. The spin contribution $G^s = i(E/mc^2)(\mathbf{e}\times\mathbf{e}')\cdot F_s(k)$ with $\mathbf{k} = \mathbf{q}-\mathbf{q}'$, where $\mathbf{e}$ and $\mathbf{q}$ ($\mathbf{e}'$ and $\mathbf{q}'$) are, respectively, the polarization vector and the wave vector of the primary (secondary) photon, and the Bragg angle θ that appears in structure factors for resonant scattering is defined by $\mathbf{q}\cdot\mathbf{q}' = q^2\cos(2\theta)$. $F_s(k)$ is the unit-cell structure factor for spin magnetic moments. The measured energy profiles of reflections $(0,0,3)_h$ and $(0,0,9)_h$ show a single resonance in the pre-edge region, devoid of secondary structure, which is modeled by a single oscillator centered at an energy $\Delta = 7.105$ keV with a width Γ, to an excellent approximation.[7] In this instance, the resonant contribution to scattering is represented by $d(E)F_{\mu'\nu}$, where $d(E) = \Delta/[E-\Delta+i\Gamma]$ and $F_{\mu'\nu}$ is a unit-cell structure factor for states of polarization μ' (secondary) and ν (primary). We follow the standard convention for orthogonal polarization labels σ and π: σ normal to the plane of scattering and, consequently, π in the plane. Unit-cell structure factors listed in the Appendix are derived following steps for the corundum structure found in Lovesey *et al.*[19] The generic form of our Bragg scattering amplitude for hematite at a space-group forbidden reflection (no Thomson scattering) is

$$G_{\mu'\nu}(E) = G^s_{\mu'\nu} + \rho\, d(E)\, F_{\mu'\nu}, \tag{1}$$

where ρ is a collection of factors, which include radial integrals for particular resonance events, which are provided in the Appendix.

Atomic multipoles $\langle T^K_Q\rangle$ in parity-even structure factors, for $E1$-$E1$ and $E2$-$E2$ events, have the property that even rank K are time-even (charge) and odd rank K are time-odd (magnetic). For enhancement at the K-absorption edge, all parity-even atomic multipoles relate to orbital degrees of freedom in the valence shell - spin degrees of freedom are absent.[24] Thus, for enhancement at the K-absorption edge, multipoles $\langle T^K_Q\rangle$ with odd K are zero if the ferric, $3d^5$ (electron configuration ^{6}S) of the iron ion is fully preserved in hematite. The measured iron magnetic moment of 4.9 μ_B at 77 K indicates that the orbital magnetic moment is small and likely no more than $\approx$2% of the measured moment.[2,5]

It is worth noting that we have used a single-domain approach for calculating the intensities, as is mentioned in the penultimate paragraph in Sec. IV D of Kokubun *et al.*[7] The justification is that the x-ray beam was sufficiently small to illuminate only one crystal domain of hematite.

III. PHASE I

We report first our analyses of data gathered by Kokubun *et al.*[7] on hematite at 150 K. With 100% incident σ polarization and no analysis of polarization in the secondary beam, the measured intensity of a Bragg reflection is proportional to

$$I = |G_{\sigma'\sigma}(E)|^2 + |G_{\pi'\sigma}(E)|^2. \quad (2)$$

For a collinear antiferromagnet, in expression (1) for $G_{\mu'\nu}(E)$ one has $G^s_{\sigma'\sigma} = 0$ and in the channel with rotated polarization

$$G^s_{\pi'\sigma} = 4\sin(\theta)\sin(\varphi l)(E/mc^2) f_s(k)\langle S^z\rangle, \quad (3)$$

where $\varphi = -37.91^\circ$, the Bragg angle $\theta = 10.96^\circ$ (34.77°) for a Miller index $l = 3$ (9), $\langle S^z\rangle \leqslant 5/2$ is the spin moment, and $f_s(k)$ is the spin form factor with $f_s(0) = 1$. Note that $|G^s_{\pi'\sigma}|^2 \propto \sin^2(\theta)$ above is not the expression in Eq. (20) in Ref. 7, which is derived by the use of an abridged scattering amplitude that is not valid in the experiment.[22]

At resonance, the spin contribution $G^s_{\pi'\sigma}$ is suppressed compared to the resonant contribution by a factor $\Gamma/\Delta \approx 10^{-4}$ and it may safely be neglected.

Confrontations between our theoretical expressions for the azimuthal-angle dependence of Bragg intensity with the corresponding experimental data reported in Ref. 7 reveal a 30° mismatch of origins in the azimuthal angle. Our origin $\psi = 0$ has the a axis normal to the plane of scattering,[19] whereas Kokubun *et al.*[7] specify an origin such that the a axis is parallel to $\mathbf{q} + \mathbf{q}'$, giving a nominal mismatch in the origin of ψ, between theory and experiment, of 90°. The actual mismatch, 30°, revealed by our analysis of data is likely to arise in the experiments by mistakenly using for reference a basal plane Bragg reflection offset by 60°. In this and the following section we reproduce data as a function of ψ offset by 30° compared to data reported in Figs. 5 and 10 in Ref. 7.

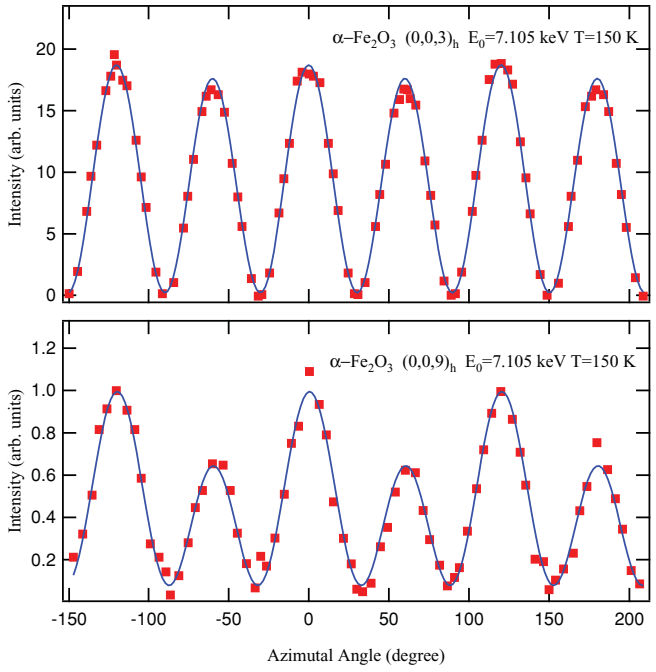

FIG. 2. (Color online) Azimuthal-angle dependence of intensity of Bragg reflections $(0,0,l)_h$ with $l = 3$ and $l = 9$ for phase I (150 K). Continuous curves are fits to structure factors for $E1$-$E2$ and $E2$-$E2$ events with magnetic (time-odd) parity-even multipoles set to zero. Inferred relative atomic multipoles are listed in Table I. Experimental data are taken from Kokubun *et al.*[7]

In light of the established negligible orbital magnetism in hematite, parity-even, time-odd atomic multipoles ($K = 1$ and 3) are set equal to zero. Looking in the Appendix one finds $F_{\mu'\nu}(E1\text{-}E1) = 0$. Additionally, $F_{\sigma'\sigma}(E2\text{-}E2) = 0$ and $F_{\pi'\sigma}(E2\text{-}E2)$ produce Templeton–Templeton scattering proportional to $[\langle T^4_{+3}\rangle' \cos(3\psi)]$, where ψ is the azimuthal angle. Inspection of data for phase I reproduced in Fig. 2 shows that an $E2$-$E2$ event on its own is not an adequate representation. The missing modulation is produced by the $E1$-$E2$ event that introduces a polar quadrupole $\langle U^2_0\rangle$ in phase with the parity-even hexadecapole.[25] Figure 2 displays satisfactory fits of $\{|F_{\sigma'\sigma}|^2 + |F_{\pi'\sigma}|^2\}$, using equal measures of $E1$-$E2$ and $E2$-$E2$ events, to data from azimuthal-angle scans performed at reflections $(0,0,l)_h$ with $l = 3$ and 9. The influence of the polar quadrupole is very notable for $l = 9$ because for this Miller index the hexadecapole is suppressed, with the ratio at $l = 9$ to $l = 3$ of $\tan(\varphi l)$ equal to 0.15. Relative values of multipoles inferred from fits to the low-temperature data are gathered in Table I. Values of $\langle T^4_{+3}\rangle'$ and $\langle U^2_0\rangle$ in phase I are found to be of one sign and in the ratio 20 : 1, with near equal magnitudes of the polar quadrupole and magnetoelectric octupole, $\langle G^3_{+3}\rangle'$. If $|\rho(E2\text{-}E2)/\rho(E1\text{-}E2)| \approx 1.0$, as suggested by our estimate, magnetoelectric multipoles are $\approx$5% of the dominant parity-even hexadecapole, $\langle T^4_{+3}\rangle'$.

Without polarization analysis, it does not seem possible from azimuthal-angle scans to distinguish between $E1$-$E2$ and $E2$-$E2$ events.However, as shown in Sec. V, the two events can be distinguished with circularly polarized x rays.

TABLE I. Relative values of atomic multipoles for collinear antiferromagnetism in phase I (at $\approx$100 K below the Morin transition) and canted antiferromagnetism in phase II (room temperature). Apart from a scale factor, the magnitude of the dominant hexadecapole, $\langle T^4_{+3}\rangle'$, is set to $+10.00$. The estimate $\langle U^2_0\rangle = +0.50$ inferred by fits to data for phase I is also used in the analysis of data for phase II. Values for other multipoles are inferred by fitting to data equal measures of $E1$-$E2$ and $E2$-$E2$ structure factors listed in the Appendix, with time-odd figures (magnetic) multipoles in $E2$-$E2$ set to zero. Fits are displayed in Figs. 2 and 4. With our definition, real $\langle\cdots\rangle'$ and imaginary $\langle\cdots\rangle''$ parts of a multipole are defined through $\langle G^K_Q\rangle = \langle G^K_Q\rangle' + i\langle G^K_Q\rangle''$ with $\langle G^K_Q\rangle^* = (-1)^Q\langle G^K_{-Q}\rangle$, and identical relations for the other two multipoles, $\langle T^K_Q\rangle$ and $\langle U^K_Q\rangle$. All multipoles with projection $Q = 0$ are purely real. Using radial integrals from an atomic code factors in Eq. (1) are in the ratio $\rho(E2\text{-}E2)/\rho(E1\text{-}E2) \approx -0.98$, which is no more than a guide to the actual value in hematite. This ratio is not eliminated in the listed values of the multipoles.

Multipole	Phase I	Phase II
$\langle G^1_{+1}\rangle'$		0.50(2)
$\langle G^2_0\rangle$	0.11(2)	
$\langle G^2_{+1}\rangle''$		−0.38(3)
$\langle G^3_{+1}\rangle'$		1.07(6)
$\langle G^3_{+3}\rangle'$	0.41(2)	2.45(5)

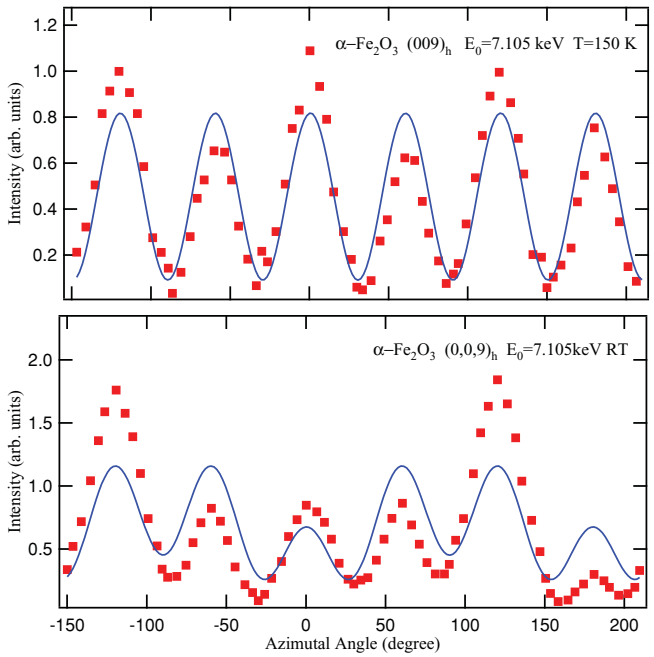

FIG. 3. (Color online) Azimuthal-angle dependence of intensity of the Bragg reflection $(0,0,9)_h$ for phases I (150 K) and II (room temperature). Continuous curves are fits to parity-even structure factors $E1$-$E1$ and $E2$-$E2$ including all magnetic multipoles. Experimental data taken from Kokubun *et al.*[7] appear also in Figs. 2 and 4.

The failure of pure parity-even structure factors $E1$-$E1$ plus $E2$-$E2$ to explain the data is most pronounced for $l = 9$. To illustrate the extent of the failure, Fig. 3 displays a fit to intensity at $l = 9$ with an amplitude made of equal amounts of $E1$-$E1$ and $E2$-$E2$ unit-cell structure factors, and the quality of the fit is clearly inferior to the one shown in Fig. 2.

IV. PHASE II

In this phase, above the Morin transition, iron magnetic moments lie in a plane normal to the c axis. We choose orthonormal principal axes (x, y, z) with the x and z axes parallel to the crystal a and c axes, respectively. The crystal a axis is parallel to a diad axis of rotation symmetry, normal to the mirror plane that contains the trigonal c axis.

The spin contribution $G^s_{\sigma'\sigma} = 0$, while the corresponding $\pi'\sigma$ scattering amplitude can be different from zero and, notably, it depends on the azimuthal angle. We find that

$$G^s_{\pi'\sigma} = 4\cos(\psi)\cos(\theta)\sin(\varphi l)\,(E/mc^2)\,f_s(k)\,\langle S^y\rangle, \quad (4)$$

and $|G^s_{\pi'\sigma}|^2 \propto \cos^2(\theta)$ from Eq. (4) is not the same as the corresponding result, Eq. (19) in Ref. 7 for reasons spelled out in Sec. III.

Away from a resonance, the result (4) predicts a twofold periodicity of intensity as a function of the azimuthal angle, which is in accord with observations in Ref. 7. The spin moment in the mirror plane $\langle S^y\rangle$ is close to 5/2 while spontaneous magnetization, directed along a diad axis, is ≈0.02% of the nominal value. From Eqs. (3) and (4) we see that the ratio of $|G^s_{\pi'\sigma}|^2$ for phases I and II depends on $\tan^2(\theta)$ which takes the value 0.04 (0.48) for $l = 3$ ($l = 9$). For $l = 3$, Kokubun *et al.*[7] report intensity between 150 K (phase I) and 300 K (phase II). Starting from ≈210 K a large increase of intensity is observed over an interval of ≈40 K. Rotation of magnetic moments from the c axis to the basal plane, between phases I and II, takes place in a range of 10 K in pure crystals but the interval can be larger in mixed materials as commented above.

Slightly away from the resonance, interference between the nonresonant, spin contribution (4) and $d(E)F_{\pi'\sigma}$ may enhance intensity in a Bragg peak if $(E-\Delta)[G^s_{\pi'\sigma}/(F_{\pi'\sigma})'] > 0$. We find $[G^s_{\pi'\sigma}/(F_{\pi'\sigma})']$ is of one sign for $l = 3$ and $l = 9$ provided that $f_s(k)$, the spin form factor, is of one sign. At face value this finding is not at one with Kokubun *et al.*[7] who discuss a sighting of slight enhancement of the intensity on the low-energy side of the resonance for $l = 9$ that is apparently absent, or completely negligible, for $l = 3$.

Figure 4 shows fits of $E1$-$E2$ and $E2$-$E2$ structure factors to data gathered at $l = 3$ and $l = 9$ in phase II (room temperature). As before, in our analysis of data gathered on phase I, parity-even multipoles with odd K are set to zero. Time-even contributions to structure factors, determined by chemical structure, are taken to be the same in phases I and II. Consistency with this assumption, about chemical structure, implies for phases I and II the same values of $\langle T^4_{+3}\rangle'$ and $\langle U^2_0\rangle$. Inferred relative values of time-odd atomic multipoles for phase II are listed in Table I, with values of $\langle T^4_{+3}\rangle'$ and $\langle U^2_0\rangle$ in the ratio 20:1. Relative to the magnitude of $\langle U^2_0\rangle$, none of the magnetoelectric multipoles are negligible in phase II. Figure 3 contains a fit of pure parity-even structure factors, $E1$-$E1$ and $E2$-$E2$, to data for the reflection $l = 9$, and the quality of the fit is clearly inferior to that reported in Fig. 4 with $E1$-$E2$ and $E2$-$E2$ structure factors.

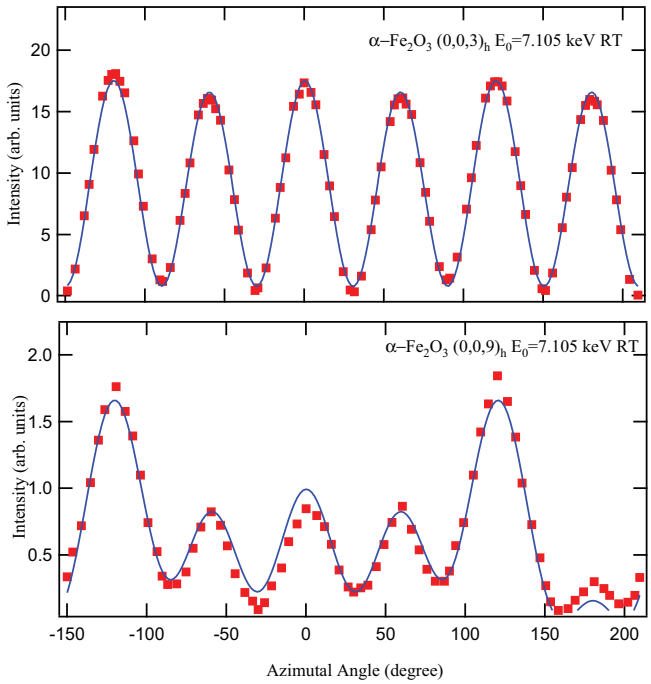

FIG. 4. (Color online) Azimuthal-angle dependence of the intensity of Bragg reflections $(0,0,l)_h$ with $l = 3$ and $l = 9$ for phase II (room temperature). Continuous curves are fits to structure factors for $E1$-$E2$ and $E2$-$E2$ events with magnetic (time-odd) parity-even multipoles set to zero. Inferred relative atomic multipoles are listed in Table I. Experimental data are taken from Kokubun *et al.*[7]

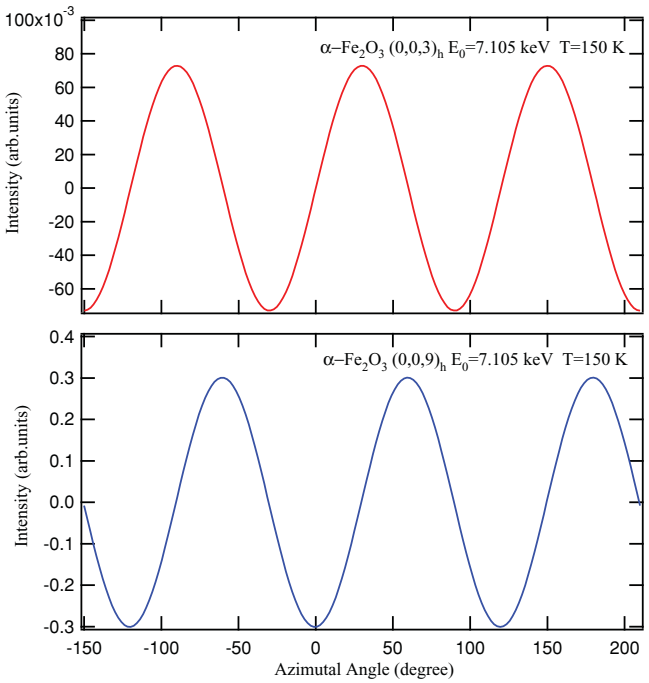

FIG. 5. (Color online) Simulation of the azimuthal-angle dependence from Eq. (6) for a circular polarized light of Bragg reflections $(0,0,l)_h$ with $l = 3$ and $l = 9$ for phase I. Continuous curves are simulations made with the values of the multipoles from the $E1$-$E2$ event gathered in Table I. For the $E2$-$E2$ event I_c is zero because our magnetic (time-odd) parity-even multipoles are zero for a ferric ion. Zero I_c does not mean zero intensity because I_c is only the circular polarization contribution to intensity.[17]

V. CHIRAL STATE

A chiral, or handed, state of a material is permitted to couple to a probe with a like property, in our case circular polarization (helicity) in the primary beam of x rays. In our notation, the pseudoscalar for helicity, P_2, is one of three purely real, time-even Stokes parameters. Intensity induced by helicity in the primary beam is (Ref. 17)

$$I_c = P_2 \mathrm{Im}\{G^*_{\sigma'\pi} G_{\sigma'\sigma} + G^*_{\pi'\pi} G_{\pi'\sigma}\}, \tag{5}$$

where the amplitudes $G_{\mu'\nu}$ are given by Eq. (1) and * denotes complex conjugation. I_c is zero for Thomson scattering since it is proportional to $(\mathbf{e}\cdot\mathbf{e}')$ and diagonal with respect to states of polarization.

Let us consider the fully compensating collinear antiferromagnet (phase I). For both $E1$-$E1$ and $E1$-$M1$ events there are no contributions diagonal with respect to states of polarization and I_c is zero. Using the structure factors listed in the Appendix for the $E1$-$E2$ and $E2$-$E2$ events, we find

$$I_c(E1\text{-}E2) = -P_2\left(\frac{8\sqrt{2}}{5}\right)\rho^2(E1\text{-}E2)\mid d(E)\mid^2 \sin(3\psi) \times \cos^3(\theta)[1+\sin^2(\theta)]\cos^2(\varphi l)\langle G^3_{+3}\rangle'\langle U^2_0\rangle \tag{6}$$

and

$$I_c(E2\text{-}E2) = -P_2 4\rho^2(E2\text{-}E2)\mid d(E)\mid^2 \sin(6\psi) \times \sin(\theta)\cos^6(\theta)\sin^2(\varphi l)\langle T^3_{+3}\rangle''\langle T^4_{+3}\rangle', \tag{7}$$

The predicted intensities are significantly different—notably in dependence on the azimuthal angle—and offer a method by which to distinguish contributions from the two events (see Figs. 5 and 6). Intensities (6) and (7) depend on long-range magnetic order, with $I_c(E2\text{-}E2) = 0$ if the ferric ion is pure ^{6}S. The polar quadrupole in Eq. (6) is a manifestation of local chirality,[19,25] whereas the pseudoscalar $\langle U^0_0\rangle$, discussed in the next section, is a conventional measure of the chirality of a material. While for phase II, we find that I_c is given

$$I_c(E1\text{-}E2) = P_2\left(\frac{8\sqrt{2}}{5}\right)\rho^2(E1\text{-}E2)|d(E)|^2\cos^2(\varphi l)\cos^2(\theta)\langle U^2_0\rangle\left\{\frac{1}{\sqrt{3}}\sin(\psi)\left[\frac{-3}{\sqrt{5}}[\cos(3\theta)+\cos(\theta)]\langle G^1_{+1}\rangle' \times[\cos(3\theta)-\cos(\theta)]\langle G^2_{+1}\rangle'' - \frac{1}{\sqrt{5}}[\cos^3(\theta)+2\cos(\theta)]\langle G^3_{+1}\rangle'\right] - \sin(3\psi)\cos(\theta)[1+\sin^2(\theta)]\langle G^3_{+3}\rangle'\right\}, \tag{8}$$

$$I_c(E2\text{-}E2) = -P_2\left(\frac{1}{\sqrt{2}}\right)\rho^2(E2\text{-}E2)|d(E)|^2\sin^2(\varphi l)\langle T^4_{+3}\rangle'\left\{4\sin(\psi)\cos^4(\theta)\left[\frac{-1}{\sqrt{5}}\sin(\theta)[8\cos^2(\theta)-5]\langle T^1_1\rangle'' + \sqrt{\frac{3}{5}}\sin(\theta)\cos^3(\theta)\langle T^3_{+1}\rangle''\right] - 4\sqrt{2}\sin(\theta)\cos^6(\theta)\sin(6\psi)\langle T^3_{+3}\rangle''\right\}. \tag{9}$$

VI. MAGNETIC CHARGE AND CHIRALITY

The pseudoscalar monopoles $\langle G^0_0\rangle$ and $\langle U^0_0\rangle$ have particularly simple and interesting physical interpretations. Both monopoles are allowed in hematite structure factors for the $E1$-$M1$ event, as we see by inspection of relevant expressions in the Appendix. A conventional measure of the chirality of electrons in a molecule or extended media is $\langle \mathbf{S}\cdot\mathbf{p}\rangle/|\langle\mathbf{p}\rangle|$, where $\mathbf{S}$ and $\mathbf{p}$ are operators for spin and linear momentum and, not unsurprisingly, $\langle U^0_0\rangle$ is proportional to $\langle \mathbf{S}\cdot\mathbf{p}\rangle/|\mathbf{p}|$. It is well-known that $\langle U^0_0\rangle$ contributes to natural circular dichroism.[26] On the other hand, $\langle G^0_0\rangle$, a magnetic charge,

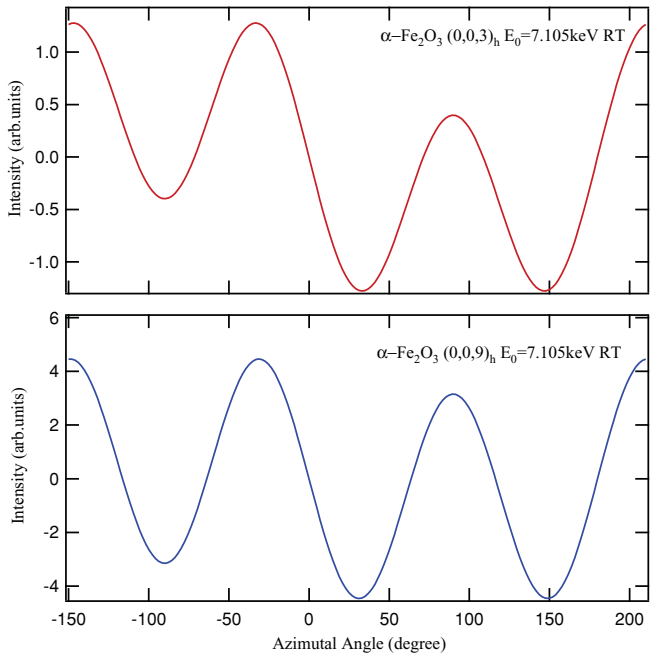

FIG. 6. (Color online) Simulation of the azimuthal-angle dependence from Eq. (8) for a circular polarized light of Bragg reflections $(0,0,l)_h$ with $l = 3$ and $l = 9$ for phase II (room temperature). Continuous curves are simulations made with the values of the multipoles from the $E1$-$E2$ event gathered in Table I. For the $E2$-$E2$ event the I_c is equal to zero because our magnetic (time-odd) parity-even multipoles are zero. Zero I_c does not mean zero intensity since I_c is only the circular polarization contribution.[17]

does not contribute to dichroic signals but it can contribute in scattering. Such is the case for gallium ferrate[27] and phase I of hematite. The magnetic charge and the magnetoelectric quadrupole are present in the amplitude for backscattering with $\mathbf{q} = -\mathbf{q}'$.

VII. DISCUSSION

We report successful analyses of resonant Bragg diffraction data gathered by Kokubun *et al.*[7] on hematite in the collinear (phase I) and canted (phase II) antiferromagnetic phases, with no analysis of diffraction according to polarization of the x rays. We infer good estimates of iron atomic multipoles and find large amounts of parity-odd multipoles. Of particular importance to a successful analysis is a polar quadrupole, a measure of local chirality,[25] and, in phase II, magnetoelectric multipoles that include the anapole. Slight departures between our theory and experiment could be due to a less than ideal crystal, as witnessed in the extended interval of temperature for rotation of magnetic moments between phases I and II.[7]

Future experiments might employ polarization analysis that will allow closer scrutiny of the unit-cell structure factors for hematite that we list in the Appendix, which are derived from the established chemical and magnetic structures of hematite. We predict for phase I that scattering enhanced by the $E1$-$M1$ event contains monopoles that represent chirality and magnetic charge.

Our analyses of data are based on an atomic theory of x-ray Bragg diffraction[19] with unit-cell structure factors that are fundamentally different from the corresponding structure factors employed by Kokubun *et al.*[7] One difference arises in the treatment of nonresonant magnetic scattering. We use the exact expression, due solely to spin moments, while Kokubun *et al.*[7] mistakenly—because it is not valid in the investigated interval of energy—use an abridged amplitude by de Bergevin and Brunel[22] that is a sum of the exact expression and the high-energy limit of two contributions to scattering that involve intermediate states (one of the two is capable of showing a resonance). Treating the resonance as a single oscillator, in accord with the reported energy profile, our structure factors for resonant diffraction are completely determined with no arbitrary phase factors, unlike the analysis in Ref. 7. This difference in the analyses is a likely explanation of our evidence that published data for azimuthal-angle scans are miss-set by 30°. Our treatment of magnetic (time-odd) contributions to scattering is another major difference in the analyses. Whereas Kokubun *et al.*[7] allow only the dipole in the $E1$-$E1$ event we consider all permitted time-odd contributions in both parity-even and parity-odd events. Time-odd multipoles from parity-even events, $\langle T^K_Q \rangle$ with odd K, are related to orbital magnetism when the intermediate state in resonance is an s state, as is the case in the experiments in question with absorption at the iron K-edge. The available evidence is that orbital magnetism of the ferric ion in hematite is negligible, as expected for an s-state ion, and the same can be said of the parity-even, time-odd multipoles, including the dipole which at resonance is the only source of magnetic scattering considered in Ref. 7. From our analysis, we conclude that magnetic scattering at resonance is provided by magnetoelectric multipoles in an $E1$-$E2$ event. We demonstrate beyond reasonable doubt that allowing magnetic $\langle T^K_Q \rangle$ different from zero the available data are not consistent with diffraction enhanced by purely parity-even events, $E1$-$E1$ and $E2$-$E2$.

In summary, we have derived information on the relative magnitude of multipoles for the antiferromagnetic phases of hematite (above and below the Morin temperature). These estimates are obtained from analyses of experimental azimuthal dependence gathered in resonant x-ray Bragg diffraction at space-group forbidden reflections $(0,0,3)_h$ and $(0,0,9)_h$. A chiral electron state is proposed from a predicted coupling of resonant intensity to circular polarization in the primary beam. This effect allows differentiating between contributions of the $E1$-$E2$ and $E2$-$E2$ events. In addition, pseudoscalar monopoles (chirality and magnetic charge) are present in the $E1$-$M1$ amplitude for resonant scattering by hematite below the Morin temperature.

ACKNOWLEDGMENTS

Gerrit van der Laan provided values of atomic radial integrals for a ferric ion. We have benefited from discussions with A. Bombardi and S. P. Collins and correspondence with F. de Bergevin. S.W.L is grateful to E. Balcar for ongoing noetic support. Financial support has been received from Spanish FEDER-MiCiNN Grant No. Mat2008-06542-C04-03. A.R.F is grateful to Gobierno del Principado de Asturias for the financial support from Plan de Ciencia, Tecnología e Innovación (PTCI) de Asturias.

APPENDIX: UNIT-CELL STRUCTURE FACTORS

Some factors in Eq. (1) contain a dimensionless quantity $\aleph = m\Delta a_0^2/\hbar^2 = 260.93$, where a_0 is the Bohr radius and $\Delta = 7.105$ keV. Radial integrals for the $E1$ and $E2$ processes at the K-absorption edge are denoted by $\{R\}_{sp}$ and $\{R^2\}_{sd}$. Estimates from an atomic code are $\{R\}_{1s4p}/a_0 = -0.0035$ and $\{R^2\}_{1s3d}/a_0^2 = 0.00095$, and it is interesting that the magnitudes are smaller than hydrogenic values with $Z = 26$ by a factor of about 3. More appropriate values of the radial integrals will be influenced by ligand ions. The $M1$ process between stationary states of an isolated nonrelativistic ion is forbidden because the radial overlap of initial and final states in the process is zero, on account of orthogonality. For an $M1$ process in a compound the radial integral, denoted here by $\{1\}_{\gamma\gamma}$, is an overlap of two orbitals with common orbital angular momentum, Γ, which may be centered on different ions. The magnitude of $\{1\}_{\gamma\gamma}$ is essentially a measure of configuration interactions and bonding, or covalancy, of a cation and ligands. Factors appearing in Eq. (1) are

$$\rho(E1\text{-}E1) = [\{R\}_{sp}/a_0]^2\aleph, \tag{A1}$$

$$\rho(E1\text{-}M1) = q\{R\}_{sp}\{1\}_{\gamma\gamma}, \tag{A2}$$

$$\rho(E1\text{-}E2) = \left[q\{R^2\}_{sd}R_{sp}/a_0^2\right]\aleph, \tag{A3}$$

$$\rho(E2\text{-}E2) = [q\{R^2\}_{sd}/a_0]^2\aleph. \tag{A4}$$

Hematite structure factors $F_{\mu'\nu}$ for forbidden reflections $(0,0,l)_h$ with $l = 3(2n+1)$ and enhancements by $E1$-$E1$, $E1$-$M1$, $E1$-$E2$, and $E2$-$E2$ events are listed below. In these expressions, the angle $\varphi = -\pi u$, where $u = 2z - 1/2 = 0.2104$ for α-Fe_2O_3, the angle θ is the Bragg angle, and $\langle T_Q^K\rangle$, $\langle G_Q^K\rangle$, and $\langle U_Q^K\rangle$ are the mean values of the atomic tensors involved.

1. Collinear antiferromagnet, phase I

($E1$-$E1$)

$$F_{\sigma'\sigma}(E1\text{-}E1) = 0 \tag{A5}$$

$$F_{\pi'\sigma}(E1\text{-}E1) = -2\sqrt{2}\sin(\varphi l)\sin(\theta)\langle T_0^1\rangle \tag{A6}$$

$$F_{\pi'\pi}(E1\text{-}E1) = 0 \tag{A7}$$

($E1$-$M1$)

$$F_{\sigma'\sigma}(E1\text{-}M1) = 0 \tag{A8}$$

$$F_{\pi'\sigma}(E1\text{-}M1) = \frac{2\sqrt{2}}{\sqrt{3}}\cos(\varphi l)\left\{2\sqrt{2}\left[-\sin^2(\theta)\langle G_0^0\rangle + i\cos^2(\theta)\langle U_0^0\rangle\right] + [2+\cos^2(\theta)]\langle G_0^2\rangle + i\cos^2(\theta)\langle U_0^2\rangle\right\} \tag{A9}$$

$$F_{\pi'\pi}(E1\text{-}M1) = 0 \tag{A10}$$

($E1$-$E2$)

$$F_{\sigma'\sigma}(E1\text{-}E2) = -\frac{4\sqrt{2}}{\sqrt{5}}\sin(3\psi)\cos(\varphi l)\cos(\theta)\langle G_{+3}^3\rangle' \tag{A11}$$

$$F_{\pi'\sigma}(E1\text{-}E2) = \frac{2}{\sqrt{5}}\cos(\varphi l)\left\{-[3\cos^2(\theta)-2]\langle G_0^2\rangle + i\cos^2(\theta)\langle U_0^2\rangle - \sqrt{2}\sin(2\theta)\cos(3\psi)\langle G_{+3}^3\rangle'\right\} \tag{A12}$$

$$F_{\pi'\pi}(E1\text{-}E2) = -\frac{4\sqrt{2}}{\sqrt{5}}\sin(3\psi)\cos(\varphi l)\cos(\theta)\sin^2(\theta)\langle G_{+3}^3\rangle' \tag{A13}$$

($E2$-$E2$)

$$F_{\sigma'\sigma}(E2\text{-}E2) = -\sqrt{2}\sin(3\psi)\sin(\varphi l)\langle T_{+3}^3\rangle'' \tag{A14}$$

$$F_{\pi'\sigma}(E2\text{-}E2) = \sqrt{\frac{2}{5}}\sin(\varphi l)\left\{\sin(3\theta)\langle T_0^1\rangle - \sin(\theta)[3\cos^2(\theta)-2]\langle T_0^3\rangle - \frac{\sqrt{5}}{4}\cos(3\psi)\left[[3\cos(3\theta)+\cos(\theta)]\langle T_{+3}^3\rangle'' - i[\cos(3\theta)+3\cos(\theta)]\langle T_{+3}^4\rangle'\right]\right\} \tag{A15}$$

$$F_{\pi'\pi}(E2\text{-}E2) = -\frac{1}{\sqrt{2}}\sin(3\psi)\sin(\varphi l)\sin(4\theta)\langle T_{+3}^3\rangle'' \tag{A16}$$

2. Canted antiferromagnet, phase II

Time-even contributions to structure factors, determined by chemical structure, are the same in phases I and II. Thus the structure factor with polar multipoles, $F_{\mu'\nu}(u)$, for phase II is identical to the foregoing expression for phase I. For the convenience of the reader, structure factors for parity-even multipoles, $F_{\mu'\nu}(t)$, are given in full, although only contributions with $K = 1$ and 3 differ from foregoing expressions.

($E1$-$E1$)

$$F_{\sigma'\sigma}(E1\text{-}E1) = 0 \tag{A17}$$

$$F_{\pi'\sigma}(E1\text{-}E1) = 4\cos(\psi)\sin(\varphi l)\cos(\theta)\langle T_{+1}^1\rangle'' \tag{A18}$$

$$F_{\pi'\pi}(E1\text{-}E1) = 4\sin(\psi)\sin(\varphi l)\sin(2\theta)\langle T_{+1}^1\rangle'' \tag{A19}$$

($E1$-$M1$)

$$F_{\sigma'\sigma}(E1\text{-}M1) = 8\sin(\psi)\cos(\varphi l)\cos(\theta)\left[-\langle G_{+1}^1\rangle' + \langle G_{+1}^2\rangle''\right] \tag{A20}$$

$$F_{\pi'\sigma}(E1\text{-}M1) = 4\cos(\psi)\cos(\varphi l)\sin(2\theta)\left[\langle G_{+1}^1\rangle\right] \tag{A21}$$

$$F_{\pi'\pi}(E1\text{-}M1) = -8\sin(\psi)\cos(\varphi l)\cos(\theta)\left[\langle G_{+1}^1\rangle' + \langle G_{+1}^2\rangle''\right] \tag{A22}$$

($E1$-$E2$)

$$F_{\sigma'\sigma}(E1\text{-}E2) = \frac{4\sqrt{2}}{\sqrt{5}}\cos(\varphi l)\cos(\theta)\left\{\frac{1}{\sqrt{3}}\sin(\psi)\left[\frac{-3}{\sqrt{5}}\langle G_{+1}^1\rangle' - \langle G_{+1}^2\rangle'' + \frac{1}{\sqrt{5}}\langle G_{+1}^3\rangle'\right] - \sin(3\psi)\langle G_{+3}^3\rangle'\right\} \tag{A23}$$

$$F_{\pi'\sigma}(E1\text{-}E2) = 2\sqrt{\frac{2}{5}}\cos(\varphi l)\sin(2\theta)\left\{\frac{\cos(\psi)}{\sqrt{3}}\left[\frac{3}{\sqrt{5}}\langle G_{+1}^1\rangle' - 2\langle G_{+1}^2\rangle'' - \frac{1}{\sqrt{5}}\langle G_{+1}^3\rangle'\right] - \cos(3\psi)\langle G_{+3}^3\rangle'\right\} \tag{A24}$$

$$F_{\pi'\pi}(E1\text{-}E2) = -\frac{4\sqrt{6}}{5}\cos(\varphi l)\Big\{\sqrt{\frac{5}{3}}\cos(\theta)\sin^2(\theta)\sin(3\psi)\langle G^3_{+3}\rangle' + \sin(\psi)\Big[\cos(3\theta)\Big(\langle G^1_{+1}\rangle' - \frac{\sqrt{5}}{3}\langle G^2_{+1}\rangle''\Big) + \frac{1}{3}\cos(\theta)[\cos^2(\theta)+3]\langle G^3_{+1}\rangle'\Big]\Big\} \quad \text{(A25)}$$

$(E2\text{-}E2)$

$$F_{\sigma'\sigma}(E2\text{-}E2) = \sin(2\theta)\sin(\varphi l)\Big\{\sin(\psi)\Big[\frac{-2}{\sqrt{5}}\langle T^1_{+1}\rangle'' - \sqrt{\frac{6}{5}}\langle T^3_{+1}\rangle''\Big] + \sqrt{2}\sin(3\psi)\langle T^3_{+3}\rangle''\Big\} \quad \text{(A26)}$$

$$F_{\pi'\sigma}(E2\text{-}E2) = -\sin(\varphi l)\Big\{\cos(\psi)\Big[\frac{2}{\sqrt{5}}\cos(3\theta)\langle T^1_{+1}\rangle'' + \sqrt{\frac{6}{5}}\cos(\theta) \times [1+\sin^2(\theta)]\langle T^3_{+1}\rangle''\Big] + \frac{1}{2\sqrt{2}}\cos(3\psi) \times \big[\cos(\theta)[3\cos(3\theta)+\cos(\theta)]\langle T^3_{+3}\rangle''\big]\Big\} \quad \text{(A27)}$$

$$F_{\pi'\pi}(E2\text{-}E2) = \frac{1}{\sqrt{2}}\sin(\varphi l)\sin(4\theta)\Big\{\sin(\psi)\Big[-\frac{4\sqrt{2}}{\sqrt{5}}\langle T^1_{+1}\rangle'' + \sqrt{\frac{3}{5}}\langle T^3_{+1}\rangle''\Big] - \sin(3\psi)\langle T^3_{+3}\rangle''\Big\} \quad \text{(A28)}$$

[1] A. H. Morrish, *Canted Antiferromagnetism: Hematite* (World Scientific, Singapore, 1994).
[2] M. Catti, G. Valerio, and R. Dovesi, Phys. Rev. B **51**, 7441 (1995).
[3] I. Dzyaloshinsky, J. Phys. Chem. Solids **4**, 241 (1958).
[4] T. Moriya, Phys. Rev. **120**, 91 (1960).
[5] E. Krén, P. Szabó, and G. Konczos, Phys. Lett. **19**, 103 (1965).
[6] K. D. Finkelstein, Q. Shen, and S. Shastri, Phys. Rev. Lett. **69**, 1612 (1992).
[7] J. Kokubun, A. Watanabe, M. Uehara, Y. Ninomiya, H. Sawai, N. Momozawa, K. Ishida, and V. E. Dmitrienko, Phys. Rev. B **78**, 115112 (2008).
[8] D. Templeton and L. Templeton, Acta Crystallogr. Sect. A: Cryst. Phys. Diffr. Theor. Gen. Crystallogr. **38**, 62 (1982).
[9] S. W. Lovesey and V. Scagnoli, J. Phys. Condens. Matter **21**, 474214 (2009).
[10] J. Fernández-Rodríguez, J. A. Blanco, P. J. Brown, K. Katsumata, A. Kikkawa, F. Iga, and S. Michimura, Phys. Rev. B **72**, 052407 (2005).
[11] S. W. Lovesey, J. Fernández-Rodríguez, J. A. Blanco, D. S. Sivia, K. S. Knight, and L. Paolasini, Phys. Rev. B **75**, 014409 (2007).
[12] J. Fernández-Rodríguez, V. Scagnoli, C. Mazzoli, F. Fabrizi, S. W. Lovesey, J. A. Blanco, D. S. Sivia, K. S. Knight, F. de Bergevin, and L. Paolasini, Phys. Rev. B **81**, 085107 (2010).
[13] S. B. Wilkins, R. Caciuffo, C. Detlefs, J. Rebizant, E. Colineau, F. Wastin, and G. H. Lander, Phys. Rev. B **73**, 060406 (2006).
[14] J. A. Paixão, C. Detlefs, M. J. Longfield, R. Caciuffo, P. Santini, N. Bernhoeft, J. Rebizant, and G. H. Lander, Phys. Rev. Lett. **89**, 187202 (2002).
[15] S. W. Lovesey and K. S. Knight, J. Phys. Condens. Matter **12**, L367 (2000).
[16] Y. Tanaka, T. Inami, S. W. Lovesey, K. S. Knight, F. Yakhou, D. Mannix, J. Kokubun, M. Kanazawa, K. Ishida, S. Nanao, T. Nakamura, H. Yamauchi, H. Onodera, K. Ohoyama, and Y. Yamaguchi, Phys. Rev. B **69**, 024417 (2004).
[17] J. Fernández-Rodríguez, S. W. Lovesey, and J. A. Blanco, Phys. Rev. B **77**, 094441 (2008).
[18] S. W. Lovesey and K. S. Knight, J. Phys. Condens. Matter **12**, L367 (2000).
[19] S. W. Lovesey, E. Balcar, K. S. Knight, and J. Fernández-Rodríguez, Phys. Rep. **411**, 233 (2005).
[20] S. W. Lovesey and E. Balcar, J. Phys. Soc. Jpn. **79**, 074707 (2010).
[21] S. W. Lovesey and E. Balcar, J. Phys. Soc. Jpn. **79**, 104702 (2010).
[22] F. De Bergevin and M. Brunel, Acta Crystallogr. A **37**, 324 (1981).
[23] S. W. Lovesey, Rep. Prog. Phys. **56**, 257 (1993).
[24] S. W. Lovesey, J. Phys. Condens. Matter **10**, 2505 (1998).
[25] V. E. Dmitrienko and E. N. Ovchinnikova, Acta Crystallogr. A **57**, 642 (2001).
[26] S. P. Collins, S. W. Lovesey, and E. Balcar, J. Phys. Condens. Matter **19**, 213201 (2005).
[27] U. Staub, Y. Bodenthin, C. Piamonteze, M. García-Fernández, V. Scagnoli, M. Garganourakis, S. Koohpayeh, D. Fort, and S. W. Lovesey, Phys. Rev. B **80**, 140410 (2009).

5.3 Article III

Chiral properties of hematite α-Fe_2O_3 inferred from resonant Bragg diffraction using circularly polarized x rays

A. Rodríguez-Fernández,[1] J. A. Blanco,[1] S. W. Lovesey,[2] V. Scagnoli,[3] U. Staub,[3] H. C. Walker,[4] D. K. Shukla,[4,*] and J. Strempfer[4]

[1]*Departamento de Física, Universidad de Oviedo, E-33007 Oviedo, Spain*
[2]*ISIS Facility and Diamond Light Source Ltd, Oxfordshire OX11 0QX, United Kingdom*
[3]*Paul Scherrer Institut, 5232 Villigen, Switzerland*
[4]*Deutsches Elektronen-Synchrotron, 22607 Hamburg, Germany*

(Received 20 June 2013; revised manuscript received 21 August 2013; published 26 September 2013)

Chiral properties of the two phases—collinear motif (below Morin transition temperature, $T_M \approx 250$ K) and canted motif (above T_M)—of magnetically ordered hematite (α-Fe_2O_3) have been identified in single-crystal resonant x-ray Bragg diffraction using circular polarized incident x rays tuned near the iron K edge. Magnetoelectric multipoles, including an anapole, fully characterize the high-temperature canted phase, whereas the low-temperature collinear phase supports both parity-odd and parity-even multipoles that are time odd. Orbital angular momentum accompanies the collinear motif, whereas it is conspicuously absent with the canted motif. Intensities have been successfully confronted with analytic expressions derived from an atomic model fully compliant with chemical and magnetic structures. Values of Fe atomic multipoles previously derived from independent experimental data are shown to be completely trustworthy.

DOI: 10.1103/PhysRevB.88.094437 PACS number(s): 78.70.Ck, 78.20.Ek, 75.50.Ee, 75.47.Lx

I. INTRODUCTION

Alpha ferric oxide (α-Fe_2O_3), also known as hematite, a name deriving from the Greek "$\alpha\iota\mu\alpha\tau\iota\tau\eta\varsigma$" due to its bloodlike shade in powder form, is still today revealing its mysteries.[1,2] Hematite has been present in the scientific literature since the studies performed by the Greek philosopher Theophrastus around 315 B.C. and later was studied by the father of magnetism, William Gilbert of Colchester, in the 16th century. Its magnetic behavior was first studied in the early 20th century by Honda and Soné (1914), but it was not until Dzyaloshinsky in 1958 when it was defined as a canted antiferromagnet, becoming the prototype of the Dzyaloshinsky-Moriya interaction.[3,4]

Hematite is a member of the corundum-structure family (centrosymmetric space group 167, $R\bar{3}c$). The ferric (Fe^{3+}, $3d^5$) ions present in α-Fe_2O_3 are arranged along the c axis occupying 4(c) sites, and they occupy sites deprived of spatial inversion symmetry. The resonant x-ray diffraction data we present in this paper are witness to the absence of local inversion symmetry in the presence of global inversion symmetry. The antiferromagnetic behavior present in this compound below its Néel temperature ($T_N \approx 948$ K) shows two different magnetic orders separated by the Morin transition temperature, $T_M \approx 250$ K. Below this temperature the magnetic moments are all parallel to the hexagonal c axis in a collinear antiferromagnetic G-type configuration (that is, the nearest neighbors have opposite spins while the next-nearest neighbors have parallel spins) with an iron magnetic moment of $4.9\mu_B$ at 77 K, while above T_M the material shows a magnetic motif where the moments are in a (basal) plane normal to the c axis showing a canted antiferromagnetic order, depicted in Fig. 1. As previously, we follow Dzyaloshinsky and label the collinear (low-temperature phase) and canted (room-temperature phase) magnetic motifs as I and II, respectively.[5] The Dzyaloshinsky-Moriya antisymmetric interaction is responsible for the behavior known as weak ferromagnetism that in the case of hematite is parallel to the dyad axis of rotational symmetry.[1,3]

Chiral order in electronic structure is unambiguously detected by a probe with a matching characteristic, as discussed by Rodríguez-Fernández*et al.*,[6] and we have used circularly polarized x rays to verify the existence of such order in a single crystal of hematite. With respect to the chirality, neutrons have perhaps given the clearest indication of such states in the past. However, the method of determining this also involves measuring the polarization of the scattered neutrons,[7] and in this case, where there is a net ferromagnetic contribution in the high-temperature phase of α-Fe_2O_3, the neutron method cannot be used because the ferromagnetic component will depolarize the incident neutrons. In contrast, tuning the x-ray energy to an atomic resonance of a ferric ion, the Fe K edge, means these ions and no others participate in the chiral order observed. In addition, the resonant process enhances the sensitivity of the scattering process to the local environments and angular anisotropy in the electron distribution that appears due to the spin, charge, or multipolar order.[5,6,8–13]

Previous experiments on hematite, using Bragg diffraction of linearly polarized x rays with the primary energy tuned near the iron K absorption edge, were performed by Finkelstein *et al.* and Kokubun *et al.*[14,15] Owing to the important contribution of the Thomson scattering in these types of experiments, attention is given to Bragg reflections that are space-group forbidden by extinction rules. Integer Miller indices obey the extinction rule l odd and $-h + k + l = 3n$ in the case of hematite.

Finkelstein *et al.* observed,[14] while rotating a single crystal about the Bragg wave vector $(003)_H$ in a so-called azimuthal-angle scan, a sixfold periodicity of the intensity that is traced to a triad axis of rotational symmetry that passes through sites occupied by resonant, ferric ions. At a later date, Kokubun *et al.* reported azimuthal-angle scans for $l = 3$ and 9.[15] Unlike these two groups, we exploit the polarization analysis of the diffracted beam to unveil contributions to the

 ©2013 American Physical Society

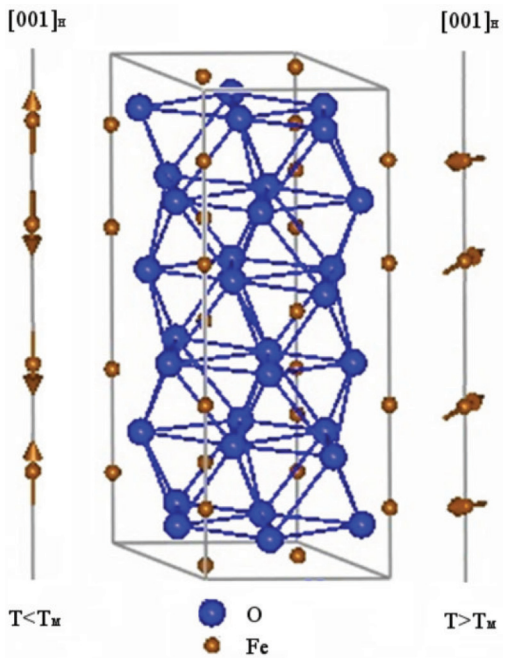

FIG. 1. (Color online) Crystal and magnetic structure of hematite. The small orange dots represent ferric ions while the large blue dots present the oxygen atoms' positions. The vertical line at left denotes the magnetic motif along the c axis below the Morin temperature (phase I). The vertical line at right denotes the motif above the Morin temperature, where iron moments are contained in the a-b plane (phase II).

magnetization with different spatial symmetries. On the way, we confirm our prediction that hematite supports chiral order[5] and gain confidence in our previously reported values of Fe atomic multipoles, because they provide a totally satisfactory description of new azimuthal-angle data for $l = 3$ and 9 gathered in phase I and phase II. A potential uncertainty in our analysis[5] of data reported in Ref. 15 is set to rest. Previously, we were forced to the conclusion that there is an error in Ref. 15 on the reported setting of the crystal in azimuthal-angle scans, and the error is confirmed here by use of our own data.

In this paper, we present data from a circular polarized x-ray diffraction experiment performed at the Fe K edge. Section II contains the description of the crystal and experiment. This is followed by the discussion of the results in Sec. III, where we report a detailed analysis of our azimuthal-angle scans for $l = 3$ and 9, for the hematite sample at 150 K (collinear motif, phase I) and 300 K (canted motif, phase II). In Sec. IV we present our final remarks and conclusions.

II. CRYSTAL AND EXPERIMENTAL METHOD

The synthetic hematite single crystal studied in this experiment was purchased from the Mateck Company. The size of the sample was about 10×10 mm^2 with a thickness of 0.5 mm, showing a polished surface near the $[00l]_H$ direction. In Cartesian coordinates our hexagonal crystal coordinates are $a_H = a(1,0,0)$, $b_H = a(-1/2,\sqrt{3}/2,0)$, and $c_H = c(0,0,1)$, with $a = 5.038$ Å and $c = 13.712$ Å.

The experimental data presented in this work were obtained at the Beamline P09, located in the synchrotron source PETRA

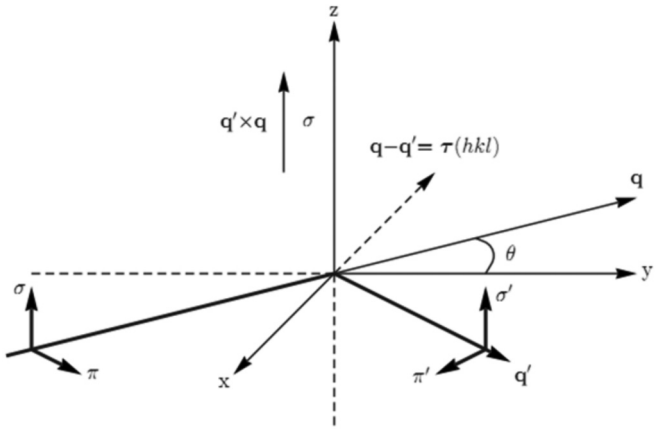

FIG. 2. Cartesian coordinates (x,y,z) and x-ray polarization and wave vectors. The plane of scattering spanned by primary ($\mathbf{q}$) and secondary ($\mathbf{q}'$) wave vectors coincides with the x-y plane. Polarization labeled σ and σ' is normal to the plane and parallel to the z axis, while polarization labeled π and π' lies in the plane of scattering. The beam is deflected through an angle of 2θ.

III (Germany).[16] This beam line covers the energy range from 2.7 to 24 keV. A double-phase-retarder setup is used to obtain the circular and rotated linear polarization for the incident beam. The double-phase-retarder setup corrects for some depolarizing effects and accomplishes a better rotated polarization rate.[17–19] Details of the incident polarization manipulation using diamond phase plates at P09 are described elsewhere.[16,17] The phase plates are followed by a focusing and higher-harmonic rejection system consisting of vertically reflecting mirrors. The plate-shaped crystal, attached to the cold finger of a closed-cycle cryostat, was mounted on a Psi diffractometer such that the $[00l]_H$ direction of the crystal is parallel to the scattering vector, $\mathbf{q} - \mathbf{q}'$, as shown in Fig. 2. Polarization analysis was performed using a Cu(220) analyzer crystal. The states of polarization labeled π (π') and σ (σ') are defined in Fig. 2.

In the case of $R\bar{3}c$, the reflections $(003)_H$ and $(009)_H$ are space-group forbidden, but weak Bragg diffraction occurs near an atomic resonance, as demonstrated by data displayed in Fig. 3. In the experiment performed at Beamline P09, the energy at which the primary x-ray beam was tuned, 7115 eV, is close to the iron K edge. At this energy the forbidden $(003)_H$ and $(009)_H$ reflections were investigated with the sample maintained at two different temperatures, below (150 K) and above (300 K) the Morin temperature.

During the experiment the incident polarization was switched between almost perfect right and left circular polarization. A measure of the high quality of circular polarization of the primary beam is demonstrated by small values of the parameters for linear polarization (following the convention of Pauli matrices as done by Lovesey *et al.*), namely, $P_1 = 0.010 \pm 0.002$ and $P_3 = 0.026 \pm 0.002$ for right handed, and $P_1 = -0.016 \pm 0.002$ and $P_3 = 0.036 \pm 0.002$ for left handed. (Properties of Stokes parameters are mentioned again in Sec. III.[20,21])

We have found an extensive contribution from Renninger reflections, also known as multibeam reflections. The subtraction of this kind of background intensity was done using

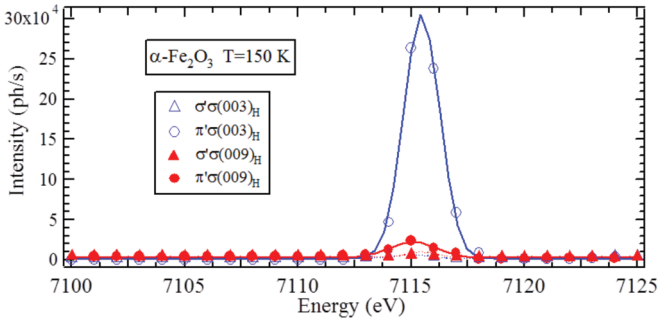

FIG. 3. (Color online) X-ray energy dependence below T_M $T = 150$ K for both reflections $(003)_H$ and $(009)_H$ in the vicinity of the iron K edge. The open blue circles (triangles) show the linear polarized $\pi'\sigma$ ($\sigma'\sigma$) data for the $(003)_H$ reflection, while the red circles (triangles) define the data from the $\pi'\sigma$ ($\sigma'\sigma$) polarized channel for the $(009)_H$ reflection. The solid lines present the fitting to a model of a single oscillator.

a MATLAB program developed by Nisbet as previously done for the extraction of the data presented in Ref. 6. Attention was focused on azimuthal angles either only lightly or not contaminated by Renninger reflections (therefore, measured points in the azimuth dependence are not equidistant).

Circular left (C_L) and circular right (C_R) polarized azimuthal scans were performed at room temperature; the difference between these two polarizations is presented in Fig. 4. Fitting to data above T_M was performed using Eqs. (3) and (4) presented in Sec. III. The multipole values used for these fittings are shown in Table I (phase II) and they agree with the ones derived by Lovesey *et al.*[5]

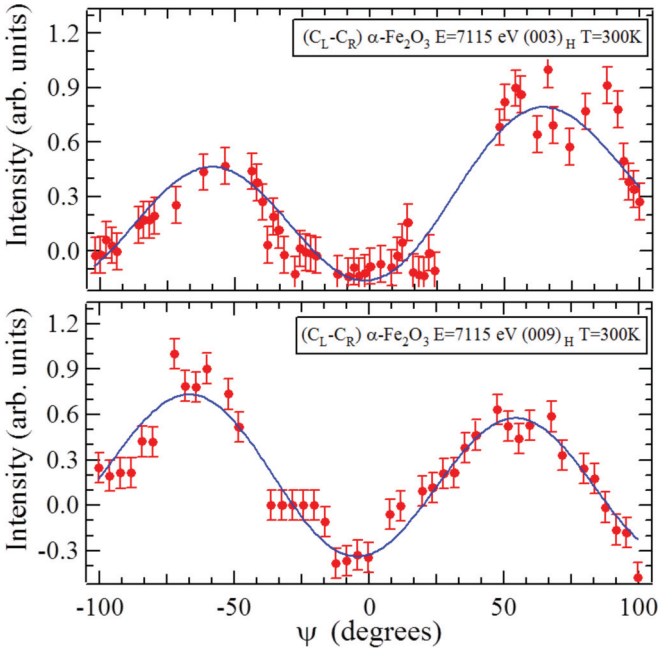

FIG. 4. (Color online) Azimuthal-angle scans for phase II (canted motif) at 300 K. Difference between circular left (C_L) and circular right (C_R) polarization for the $(003)_H$ reflection (top) and the $(009)_H$ reflection (bottom). The red circles represent the experimental data while the blue line shows expression (5) for pure $E1$-$E2$ resonance evaluated with multipoles taken from Ref. 5 and reproduced in Table I.

TABLE I. Numerical values of multipoles reported in Ref. 5 and used here for intensities generated from expressions (3)–(6). As in Ref. 5, $\langle T_3^4\rangle'$ and $\langle U_0^2\rangle$, multipoles which contribute in both phases, are fixed to 10 and 0.5, respectively.

Multipole	Phase I	Phase II
$\langle G_{+1}^1\rangle'$		$5.0(2) \times 10^{-1}$
$\langle G_{+1}^2\rangle''$		$-3.8(3) \times 10^{-1}$
$\langle G_{+1}^3\rangle'$		$10.7(6) \times 10^{-1}$
$\langle G_{+3}^3\rangle'$	$4.1(2) \times 10^{-1}$	$24.5(5) \times 10^{-1}$
$\langle T_3^3\rangle''$	$1.0(1) \times 10^{-4}$	

The azimuthal scan dependence of the $(003)_H$ reflection below T_M is presented in Fig. 5, whereas that for the $(009)_H$ reflection is shown in Fig. 6. As in the case of room temperature, multipole values used in the fitting are those derived by Lovesey *et al.*, collected in Table I (phase I).[5]

III. RESULTS AND DISCUSSION

For an interpretation of the experimental data, shown in Figs. 4, 5, and 6, we proceed as in Ref. 5. The contribution of Thomson scattering is absent at space-group-forbidden reflections, leaving a sum of nonresonant spin and a resonant contribution as ingredients for the appropriate scattering amplitude.[21,22]

The spin contribution, G^s, is explicitly first order in the small quantity E/mc^2, where E is the primary energy and mc^2 the electron rest mass energy. Using notation displayed in Fig. 2, $G^s = i(E/mc^2)(\mathbf{e}\times\mathbf{e}')\cdot\ \mathbf{F_s}(\mathbf{k})$, where $\mathbf{k} = \mathbf{q} - \mathbf{q}' = (h,k,l)$ and $\mathbf{e}$ and $\mathbf{q}$ ($\mathbf{e}'$ and $\mathbf{q}'$) are, respectively, the polarization vector and wave vector of the primary (secondary) photon, while $\mathbf{F_s}(\mathbf{k})$ is the unit-cell structure factor for spin dipoles.[23,24]

The measured energy profiles, displayed in Fig. 3 for the reflections $(003)_H$ and $(009)_H$, show a single resonance in the pre-edge region that can be adequately modeled by a single

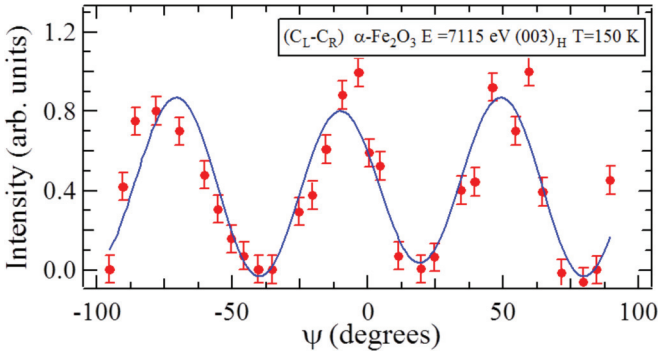

FIG. 5. (Color online) Azimuthal-angle scan for phase I (collinear motif) at 150 K. Difference between circular left (C_L) and circular right (C_R) polarization for $(003)_H$ reflection. The red circles represent the experimental data while the blue line shows expressions (3) and (4) for a mixture of $E1$-$E2$ and $E2$-$E2$ resonances evaluated with multipoles taken from Ref. 5 and reproduced in Table I. In Eq. (4) the parity-even and time-odd octupole $\langle T_3^3\rangle''$ is given a nominal value of $1(\pm 0.1) \times 10^{-4}$.

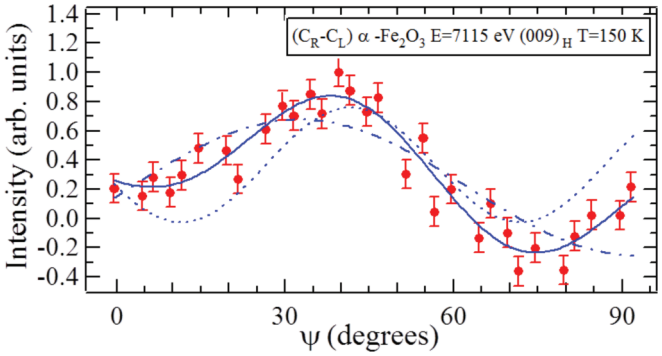

FIG. 6. (Color online) Azimuthal-angle scan for phase I (collinear motif) at 150 K. Difference between circular left (C_L) and circular right (C_R) polarization for the $(009)_H$ reflection. As in Fig. 5, the red circles represent the experimental data while the blue line shows a mixture of $E1$-$E2$ and $E2$-$E2$ resonances. Data are compared to pure $E1$-$E2$ [Eq. (3)] (dashed line) and pure $E2$-$E2$ [Eq. (4)] (dotted line) resonances, with multipoles taken from Ref. 5 and reproduced in Table I. In Eq. (4) the octupole $\langle T_3^3\rangle''$ is given a nominal value of 0.0001.

oscillator centered at an energy $\Delta = 7115$ eV.[5] The resonant contribution to scattering is represented by $d(E)F_{\mu'\nu}$, where $d(E) = \Delta/[E - \Delta + i\Gamma]$ with Γ the width in energy and $F_{\mu'\nu}$ a unit-cell structure factor for states of polarization μ' (secondary) and ν (primary), as in Fig. 2.

The generic form of our Bragg scattering amplitude for hematite at a space-group-forbidden reflection (no Thomson scattering) is

$$G_{\mu'\nu}(E) = G^s_{\mu'\nu} + \rho d(E) F_{\mu'\nu}. \tag{1}$$

In this expression, ρ is a collection of factors, which includes radial integrals for particular resonance events, namely, $\rho(E1\text{-}E1) = [\{R\}_{sp}/a_o]^2\aleph$, $\rho(E1\text{-}E2) = [q\{R^2\}_{sd}\{R\}_{sp}/a_o^2]\aleph$, and $\rho(E2\text{-}E2) = [q\{R^2\}_{sd}/a_o]^2\aleph$. Here, $\aleph$ is a dimensionless quantity related to the Bohr radius a_0 and the resonant energy $\Delta = 7115$ eV, with $\aleph = m\Delta a_o^2/\hbar^2 = 260.93$. The sizes of radial integrals for the $E1$ and $E2$ processes at the K absorption edge, $\{R\}_{sp}$ and $\{R^2\}_{sd}$, are discussed in Ref. 5.

The polarization state of the photons, already briefly discussed in Sec. II, is defined by Stokes parameters that are purely real and time even, namely, ordinary scalars P_1 and P_3 for linear polarization, and a pseudoscalar P_2 that represents the helicity of the beam. The contribution to the total intensity induced by circular polarization (helicity), I_c, is[20]

$$I_c = P_2\,\mathrm{Im}\{G^*_{\sigma'\pi}\,G_{\sigma'\sigma} + G^*_{\pi'\pi}\,G_{\pi'\sigma}\}, \tag{2}$$

where the amplitudes $G_{\mu'\nu}$ are given by Eq. (1) and * denotes complex conjugation. I_c is zero for Thomson scattering since it is proportional to $(\mathbf{e}\cdot\mathbf{e}')$ and diagonal with respect to the polarization states.

We make use of unit-cell structure factors reported in our previous publication.[5] Full use is made of the established chemical and magnetic structures in their construction. Degrees of freedom in the electronic ground state of a ferric ion are captured in atomic multipoles labeled by their rank, K, and projection, $Q(-K \leqslant Q \leqslant K)$.[21,22] Two types of multipoles are required, parity even, $\langle T_Q^K\rangle$, and two flavors of parity-odd multipoles, $\langle G_Q^K\rangle$ and $\langle U_Q^K\rangle$, distinguished by their time signatures. Magnetoelectric multipoles, $\langle G_Q^K\rangle$, are time odd and absent in the paramagnetic phase, and polar multipoles, $\langle U_Q^K\rangle$, are time even, while $(-1)^K$ is the time signature of $\langle T_Q^K\rangle$. Parity-even multipoles arise in $E1$-$E1$ and $E2$-$E2$ resonant events, and parity-odd multipoles are required for $E1$-$E2$ events, where $E1$ denotes an electric-dipole operator and $E2$ denotes an electric-quadrupole operator. All multipoles have the complex conjugate $\langle O_Q^K\rangle^* = (-1)^Q\,\langle O_{-Q}^K\rangle$, with $\langle O_0^K\rangle$ purely real, and the relative phase of real and imaginary components is set by $\langle O_Q^K\rangle = \langle O_Q^K\rangle' + i\langle O_Q^K\rangle''$.

Expressions for I_c given in Ref. 5 are repeated here for the convenience of the reader.

Below T_M (phase I, collinear motif). There is no contribution to I_c from $E1$-$E1$ reflection, due to crystal symmetry, and

$$I_c(E1\text{-}E2) = -P_2\left(\frac{8\sqrt{2}}{5}\right)\rho^2(E1\text{-}E2)|d(E)|^2\sin(3\psi) \times \cos^3(\theta)\,[1+\sin^2(\theta)]\cos^2(\varphi l)\langle G_{+3}^3\rangle'\langle U_0^2\rangle, \tag{3}$$

$$I_c(E2\text{-}E2) = -P_2\,4\rho^2(E2\text{-}E2)|d(E)|^2\sin(6\psi) \times \sin(\theta)\cos^6(\theta)\sin^2(\varphi l)\langle T_{+3}^3\rangle''\langle T_{+3}^4\rangle'. \tag{4}$$

In these expressions, the angle $\varphi = -\pi u$, where $u = 2z - 1/2 = 0.2104$ for α-Fe_2O_3.

At the K edge, when the spin degrees of freedom associated with the resonant ion are absent in the electronic ground state, the parity even multipoles with K odd are function only of the orbital angular momentum.[25] In this case, $\langle T_3^3\rangle''$ in Eq. (4) is zero for the pure ferric ion, because it has a shell that is half filled and spherically symmetric (^{6}S, $3d^5$). In our previous study, where we interpreted data published by Kokubun *et al.*,[15] we took $\langle T_3^3\rangle'' = 0$ on this basis. Our superior data displayed in Figs. 5 and 6, collected with the benefit of polarization analysis, shows that $\langle T_3^3\rangle''$ is different from zero in Eq. (4). As a consequence, the ferric ion possesses unquenched orbital angular momentum.

Dashed and dotted lines in Fig. 6 show our data for the $(009)_H$ reflection compared separately to $E1$-$E2$ and $E2$-$E2$ reflections. Evidently, a single event is not responsible for our observed intensities. However, a combination of the two events, $E1$-$E2$ and $E2$-$E2$, provides a satisfactory account; the fit represented by the continuous line in Fig. 6 confirms that this is so.

Concerning the contribution to the intensity from parity-odd multipoles [Eq. (3)], the requirement to have a value different from zero tells us that $(\langle G_3^3\rangle', \langle U_0^2\rangle)$ is not zero. Notably, $\langle U_0^2\rangle$ is a manifestation of local chirality.[21,22,25,26] The polar quadrupole is the same in the two phases, because it is related to chemical structure, whereas $\langle G_3^3\rangle'$ has a similar, small value in phase I and a much larger value in phase II.

Above T_M (phase II, canted motif). Our data for this phase and two reflections are displayed in Fig. 4. Appropriate expressions for intensities induced by circular polarization in

the primary beam are[5]

$$I_c(E1\text{-}E2) = P_2\left(\frac{8\sqrt{2}}{5}\right)\rho^2(E1\text{-}E2)\,|d(E)|^2\cos^2(\varphi l)\cos^2(\theta)\langle U_0^2\rangle\left\{\frac{1}{\sqrt{3}}\sin(\psi)\left[\frac{-3}{\sqrt{5}}[\cos(3\theta)+\cos(\theta)]\langle G_{+1}^1\rangle' + [\cos(3\theta) - \cos(\theta)]\langle G_{+1}^2\rangle'' - \frac{1}{\sqrt{5}}[\cos^3(\theta)+2\cos(\theta)]\langle G_{+1}^3\rangle'\right] - \sin(3\psi)\cos(\theta)\,[1+\sin^2(\theta)]\langle G_{+3}^3\rangle'\right\}, \quad (5)$$

$$I_c(E2\text{-}E2) = -P_2\left(\frac{1}{\sqrt{2}}\right)\rho^2(E2\text{-}E2)|d(E)|^2\sin^2(\varphi l)\langle T_{+3}^4\rangle'\left\{4\sin(\psi)\cos^4(\theta)\left[\frac{-1}{\sqrt{5}}\sin(\theta)\,[8\cos^2(\theta)-5]\langle T_1^1\rangle'' + \sqrt{\frac{3}{5}}\sin(\theta)\cos^3(\theta)\langle T_{+1}^3\rangle''\right] - 4\sqrt{2}\sin(\theta)\cos^6(\theta)\sin(6\psi)\langle T_{+3}^3\rangle''\right\}. \quad (6)$$

Our data in Fig. 4 agree with the prediction of an $E1$-$E2$ event [Eq. (5)] evaluated with multipoles carried over from our previous work.[5] Correspondingly, magnetoelectric multipoles are large compared to their values in phase I, with an octupole dominant. Treating $\langle T_Q^K\rangle$ with K odd in Eq. (6) as unknowns, it is not possible to find a satisfactory fit to a pure $E2$-$E2$ event, and it has no role in an interpretation of phase II. As the hexadecapole $\langle T_3^4\rangle'$ is the same in the two phases, because it is determined by chemical structure, and likewise local chirality $\langle U_0^2\rangle$, we conclude that orbital angular momentum, manifest through $\langle T_Q^K\rangle$ with K odd, is insignificant in the high-temperature magnetic phase.

IV. CONCLUSION

We report extensive data on magnetically ordered hematite gathered with the experimental technique of x-ray Bragg diffraction augmented by an atomic resonance. The primary energy was tuned close to the iron K edge, and intensities were measured at space-group-forbidden reflections, $(003)_H$ and $(009)_H$, that are exceptionally sensitive to magnetic degrees of freedom in the electronic ground state. The use of polarization analysis improved the quality of our data significantly. We chose circular polarization and reported differences in intensities gathered with left- and right-handed primary polarization.

The existence of intensity induced by circular polarization confirms that magnetically ordered hematite is chiral, as we predicted.[5] Moreover, we confirm that our previous estimates of parity-odd multipoles, using data published by Kokubun *et al.*,[15] are completely trustworthy. Below the Morin transition, the collinear motif contains orbital angular momentum and the ferric ion is not spherically symmetric (e.g., ^{6}S, $3d^5$). However, we find no evidence of orbital angular momentum in the canted motif that exists above the Morin transition. In this phase, diffraction can be interpreted with parity-odd multipoles only, with magnetoelectric octupoles making the dominant contribution. The existence of an orbital magnetic moment is a consequence of the spin-orbit coupling, which is a necessary ingredient of the Dzyaloshinsky-Moriya interaction that is responsible for the noncollinear magnetic structure above T_M. However, the magnitude of the orbital magnetic moment at room temperature is almost negligible compared to that found at 150 K, owing to entropic effects where the orientation of the orbital moment is almost randomized by its thermal energy. Additional experiments at intermediate temperatures could confirm this issue.

ACKNOWLEDGMENTS

Financial support has been received from Spanish FEDER-MiCiNN Grant No. MAT2011-27573-C04-02. One of us (A.R.F.) is grateful to Gobierno del Principado de Asturias for the financial support from Plan de Ciencia, Tecnología e innovación (PTCI) de Asturias. We thank the Deutsches Elektronen-Synchrotron for access to Beamline P09 of the synchrotron PETRA III (I-20110433 EC) that contributed to the results presented here. This work has been supported by National Centre of Competence of Research—Materials with Novel Electrical Properties of the Swiss National Science Foundation.

*Present address: UGC DAE Consortium for Scientific Research, Khandwa Road, Indore 01, India.

[1] A. H. Morrish, *Canted Antiferromagnetism: Hematite* (World Scientific, Singapore, 1994).
[2] M. Catti, G. Valerio, and R. Dovesi, Phys. Rev. B **51**, 7441 (1995).
[3] I. Dzyaloshinsky, J. Phys. Chem. Solids **4**, 241 (1958).
[4] T. Moriya, Phys. Rev. **120**, 91 (1960).
[5] S. W. Lovesey, A. Rodríguez-Fernández, and J. A. Blanco, Phys. Rev. B **83**, 054427 (2011).
[6] A. Rodríguez-Fernández, S. W. Lovesey, S. P. Collins, G. Nisbet, and J. A. Blanco, arXiv:1305.0484 [cond-mat.mtrl-sci].
[7] J. A. Blanco, P. J. Brown, A. Stunault, K. Katsumata, F. Iga, and S. Michimura, Phys. Rev. B **73**, 212411 (2006).
[8] S. W. Lovesey and V. Scagnoli, J. Phys.: Condens. Matter **21**, 474214 (2009).
[9] J. Fernández-Rodríguez, J. A. Blanco, P. J. Brown, K. Katsumata, A. Kikkawa, F. Iga, and S. Michimura, Phys. Rev. B **72**, 052407 (2005).
[10] S. W. Lovesey, J. Fernández-Rodríguez, J. A. Blanco, D. S. Sivia, K. S. Knight, and L. Paolasini, Phys. Rev. B **75**, 014409 (2007).
[11] S. B. Wilkins, R. Caciuffo, C. Detlefs, J. Rebizant, E. Colineau, F. Wastin, and G. H. Lander, Phys. Rev. B **73**, 060406 (2006).

[12]J. A. Paixão, C. Detlefs, M. J. Longfield, R. Caciuffo, P. Santini, N. Bernhoeft, J. Rebizant, and G. H. Lander, Phys. Rev. Lett. **89**, 187202 (2002).
[13]Y. Tanaka, T. Inami, S. W. Lovesey, K. S. Knight, F. Yakhou, D. Mannix, J. Kokubun, M. Kanazawa, K. Ishida, S. Nanao, T. Nakamura, H. Yamauchi, H. Onodera, K. Ohoyama, and Y. Yamaguchi, Phys. Rev. B **69**, 024417 (2004).
[14]K. D. Finkelstein, Q. Shen, and S. Shastri, Phys. Rev. Lett. **69**, 1612 (1992).
[15]J. Kokubun, A. Watanabe, M. Uehara, Y. Ninomiya, H. Sawai, N. Momozawa, K. Ishida, and V. E. Dmitrienko, Phys. Rev. B **78**, 115112 (2008).
[16]J. Strempfer, S. Francoual, D. Reuther, D. K. Shukla, A. Skaugen, H. Schilte-Schrepping, T. Kracht, and H. Franz, J. Synchrotron Rad. **20**, 541 (2013).
[17]S. Francoual, J. Strempfer, D. Reuther, D. K. Shukla, and A. Skaugen, J. Phys. Conf. Ser. **425**, 132010 (2013).
[18]K. Okitsu, Y. Ueji, K. Sato, and Y. Amemiya, J. Synchrotron Radiat. **8**, 33 (2001).
[19]V. Scagnoli, C. Mazzoli, C. Detlefs, P. Bernard, A. Fondacaro, L. Paolasini, F. Fabrizi, and F. de Bergevin, J. Synchrotron Radiat. **16**, 778 (2009).
[20]J. Fernández-Rodríguez, S. W. Lovesey, and J. A. Blanco, Phys. Rev. B **77**, 094441 (2008).
[21]S. W. Lovesey, E. Balcar, K. S. Knight, and J. Fernández-Rodríguez, Phys. Rep. **411**, 233 (2005).
[22]S. W. Lovesey and E. Balcar, J. Phys. Soc. Jpn. **82**, 021008 (2012).
[23]U. Staub, Y. Bodenthin, C. Piamonteze, S. P. Collins, S. Koohpayeh, D. Fort, and S. W. Lovesey, Phys. Rev. B **82**, 104411 (2010).
[24]U. Staub, C. Piamonteze, M. Garganourakis, S. P. Collins, S. M. Koohpayeh, D. Fort, and S. W. Lovesey, Phys. Rev. B **85**, 144421 (2012).
[25]S. W. Lovesey, J. Phys.: Condens. Matter **10**, 2505 (1998).
[26]V. E. Dmitrienko and E. N. Ovchinnikova, Acta Crystallogr. Sect. A **57**, 642 (2001).

CHAPTER 6

Bismuth Ferrite, $BiFeO_3$

Article IV

Article in press in Journal of the Physical Society of Japan: "Chiral Properties of Bismuth Ferrite ($BiFeO_3$) Inferred from Resonant x-ray Bragg Diffraction".

Abstract

Resonant X-ray diffraction data gathered near the Fe K-edge (7.1135 keV) for a single crystal of bismuth ferrite support a new chiral phase, in the only multiferroic material known above room temperature, formed by a circular cycloid propagating along $(1,1,0)_H$. The R3c forbidden reflection $(0,0,9)_H$ was studied as a function of the rotation of the crystal about the Bragg wave-vector in both phases, paramagnetic (700 K) and antiferromagnetic (300 K). Templeton and Templeton (T&T) scattering at 700 K is attributed in part to charge-like quadrupoles absent in a standard model of a cycloid in which a material vector generates all electronic states of the resonant ion. Extensive sets of azimuthal-angle data are used to infer values of three atomic multipoles in a satisfactory minimal model of the iron electronic structure, with a quadrupole (E1E1 event) and a hexadecapole (E2E2 event) contributing T&T scattering, plus a magnetic dipole (E1E1).

6.1 Results and Summary

When in a material appear to types of ordering (magnetic, electric or elastic) at the same phases this material is denominated multiferroic. These materials are of interest for application in devices, being more attractive the ones that present a coupling between the different degrees of freedom as the case of piezoelectric materials (elastic and electric orderings)) or magnetoelectric materials (magnetic and electric orderings), being these last ones of special interest for the field of storage information and spintronics [35]. A paradigmatic or special case of these materials is Bismuth Ferrite ($BiFeO_3$); this compound is the only one that presents both orderings, antiferromagnetism ($T_N \approx 640\,K$) and ferroelectricity ($T_C \approx 1100\,K$) above room temperature, being a key material for the future application of multiferroics in future devices.

In the beginning of the PhD work a large effort was devoted to the syntheses of bismuth ferrite from $Bi(NO_3)_3 5H_2O$ and $Fe(NO_3)_3 9H_2O$ powders using two different techniques,[2] hydrothermal synthesis [82, 83] and Microwave Oven synthesis [84]. The chemical relation used is presented in equation (6.1) and (6.2), respectively.

$$Bi(NO_3)_3 5H_2O(s) + Fe(NO_3)_3 9H_2O(s) + H_2O(l) + KOH(dis) + NNO_3(l) \rightarrow BiFeO_3(s) + liquids \qquad (6.1)$$

The hydrothermal synthesis was performed in a oven with a constant temperature of 200 ºC obtaining the best quality $BiFeO_3$ powder for the following proportions $Bi(NO_3)_3 5H_2O(s)$ 4.85 g, $Fe(NO_3)_3 9H_2O(s)$ 4.05g, $H_2O(l)$ 15ml, 2ml $NNO_3(l)$ and $KOH(dis)$ 20ml, over 72 hours. This powder was not as good as the one produced with the microwave oven system, as presented in Figure 6.1, where the amount of powder was reduced due to the small recipient for this kind of systems ($Bi(NO_3)_3 5H_2O(s)$ 1.25 g, $Fe(NO_3)_3 9H_2O(s)$ 1.05g, 1ml $NNO_3(l)$ and $KOH(dis)$ 10ml for 12 cycles of 30 minutes under 180ºC.

$$Bi(NO_3)_3 5H_2O(s) + Fe(NO_3)_3 9H_2O(s) + KOH(dis) + NNO_3(l) \rightarrow BiFeO_3(s) + liquids \qquad (6.2)$$

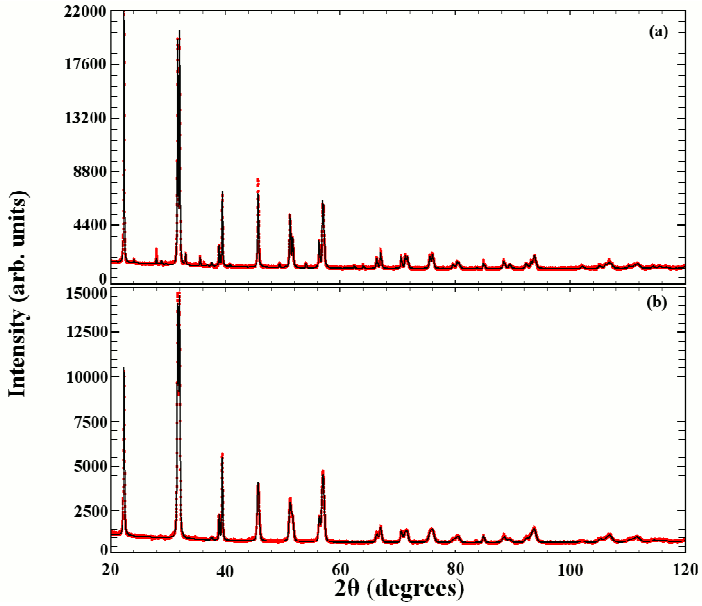

Figure 6.1. Powder diffraction data obtained from (a) $BiFeO_3$ synthesized by hydrothermal technique and (b) $BiFeO_3$ synthesized with a microwave oven.

The structure of the powder obtained by both techniques was obtained by powder X-ray diffraction using the Rietveld method confirmed the presence of Bismuth ferrite, which is a member of the R3c space group family (Figure 1 article IV). Scanning Electron Microscope characterization of the samples was also performed, Figure 6.2, as it is shown in the imagines a nano and micro crystal formation with the right proportions (1:1:3) between the elements. For the hydrothermal synthesis case the percentage is 13.78 for Bi, 14.95 for Fe and 71.27 for O, while for the microwave synthesis the powder was formed by 14.65 of Bi, 14.13 of Fe and 71.22 of O.

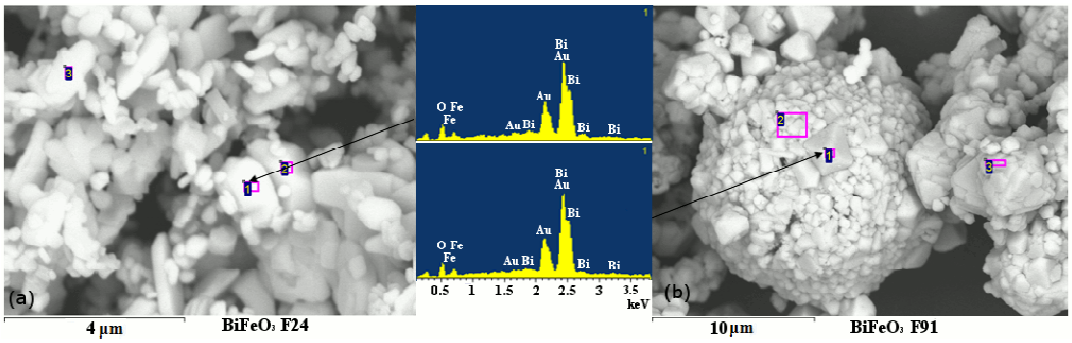

Figure 6.2. Scanning Electronic Microoscope (SEM) images and element characterization of two powder samples synthesis by (a) hydrothermal thecnique and (b) Microwave oven.

$BiFeO_3$ calcium doped powder, synthesis by G. Catalan, was studied under pressure at the Institute Laue-Lagevin (Grenoble).[3] The experiment was done at

the beamlines D1B and D20. The powder of $BiFeO_3$ without any doping goes through three different structures in the range of 10 GPa of a Paris-Edinburgh cell [85], below 6.2 GPa the structure coincide with a R3c, being at this pressure a phase transition to monoclinic C2/m followed by a Orthorhombic Pnma phase above 14 GPa. The presence of Ca^{2+} as a doping in this compound increase the chemical pressure, with it the Monoclinic phases do not appear in the characterization of the scattering data using Rietveld method, as presented in Figure 6.3.

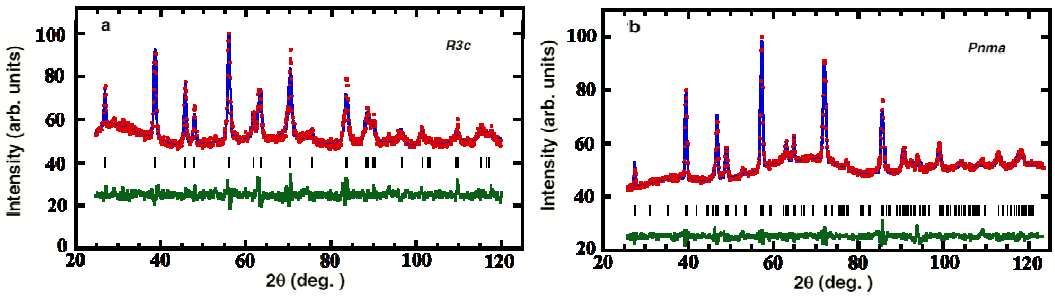

Figure 6.3. (a) Rietveld fitting for $Bi_{1-X}Ca_XFeO_3$ at Room pressure and (b) at 10 GPa.

But the low quality of the crystals obtained by the hydrothermal technique and the difficulties to grow single crystals from the powder obtained by the microwave technique, lead us to contact G. Catalan, who provide us a single crystal of $BiFeO_3$ to perform the REXS experiments we were interested in.

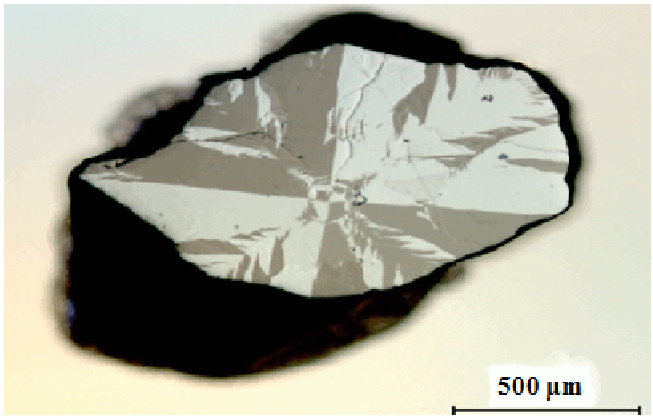

Figure 6.4. Single crystal of $BiFeO_3$ studied under REXS at Diamond Light Source, the direction $(0,0,l)_H$ is specular to the surface.

The high-quality single crystal used for the experiment (sizes $5 \times 5mm^2$ and a thickness of $0.5\ mm$) had a face perpendicular to the $(0,0,l)_H$ direction the experiment was performed with a specular geometry (Figure 6.4). While it is

possible that the sample supports different domains, the very small size of the primary beam gives some confidence that a single domain is illuminated in our experiments. Indeed, we go on to show that, a chiral motif and a single domain are implied by our findings for the magnetically-ordered state.

The experiment took place at beamline I16 of Diamond light source, which works at the energy of 3 GeV in the "top-up" mode; this beamline is equipped with a 6-circle kappa diffractometer and a focusing optical system that gives a photon flux on the sample position of 10^{13} $photon/s$ and a beam size of 180×20 μm^2. The horizontally polarized beam, σ, delivered by a linear undulator was tuned near the Fe K-edge (7.1135 keV).

The reflection studied was the forbidden $(0,0,9)_H$ in the space group #161. As is possible to observe from Figure 3 in article IV, the weak contribution to the intensity by Bragg diffraction due to angular anisotropy is strongly enhanced by an atomic resonance. Two different temperatures were studied for the $(0,0,9)_H$ reflection, below (300 K) and above (700 K) the Néel Temperature. Following the scheme from Figure 3.3, all data collected were obtained in the rotated channel of polarization π'σ.

The symmetry related to these sites does not allow intensity by pure electric dipole (E1E1) events in the case of forbidden reflections of the type $(0,0,l)_H$, with l odd. However, diffraction enhanced by pure electric quadrupole (E2E2) event is allowed and can be produced by an atomic electric, time-even, hexadecapole.

The $R3c$ space group symmetry allows diffraction enhanced by pure electric quadrupole (E2E2) events for forbidden reflections of the type $(0,0,l)_H$, with l odd. This contribution is described by the real part of the hexadecapole $\langle T^4_{+3}\rangle$, denoted by $\langle T^4_{+3}\rangle'$. For the Fe ions in sites $6a$ in $R3c$ structure, diffraction with wavevector $(0,0,l)_H$ is described by an electronic structure factor,

$$\Psi^K_Q = 3\left[\langle T^K_Q\rangle_1 + (-1)^l \langle T^K_Q\rangle_2\right], \qquad (6.3)$$

where the relation between sites 1 and 2 is given by a rotation about the diagonal $\boldsymbol{a_h} + \boldsymbol{b_h}$ by 180^0 plus an inversion. Using the formalism for the calculation of

the amplitude of scattering presented in section 2.4.2 for the pure E2 events, it is obtained the contribution for the $\pi'\sigma$ channel as,

$$Z_{\pi'\sigma}(E2E2) = \left(\frac{q\{R^2\}_{sd}}{a_0}\right)^2 \left(\frac{m\Delta {a_0}^2}{\hbar^2}\right)\frac{3}{\sqrt{2}} cos^3\theta\ cos(3\psi)\langle T^4_{+3}\rangle', \qquad (6.4)$$

And the contribution from the parity-odd E1E2 events in the π'σ channel of immediate interest comes from a purely real polar quadrupole,

$$Z_{\pi'\sigma}(E1E2) = \left(\frac{m\Delta {a_0}^2}{\hbar^2}\right)\left(\frac{\{R\}_{sp} q\{R^2\}_{sd}}{{a_0}^2}\right) i(3/\sqrt{5})\ cos(2\theta)\langle U^2_0\rangle\ . \qquad (6.5)$$

The Templeton-Templeton (T&T) scattering reported in Figure 4 from article IV, (red dots) $700\,K$ and (white dots) $300\,K$ ($T_N \approx 640\,K$), were obtained in the polarization channel π'σ. From the data presented it is possible to observe that E2E2 events together with a contribution from the parity-odd E1E2 resonance due to the fact that the two contributions are in phase quadrature and they cannot interfere to give the pure six-fold periodicity that is lacking in Figure 4 (red dots).

Table 6.1. Values of the parameters used for the fitting for the two temperatures studied. In the case of 700K the parameter v was set to 0, see text for more details.

Parameter	700K	300K
t	1.19 ± 0.07	1.19 ± 0.07
u	- 6.20 ± 0.16	- 6.20 ± 0.16
v	-	0.673 ± 0.014

The presence of long range ordering due to a circular cycloid structure is responsible for a break of the symmetry inside the material that will allow charge-like quadrupoles contribution (K=2) to be observed through an E1E1 event. This motif related to the DM interaction has been showed in many multiferroic materials as presented in the work by Przeniosło et al; see Model 1 in Figure 1 [86]. While electric dipole (E1E1) transitions are normally appreciably stronger than electric quadrupole (E2E2) events, in this case as the diffraction from the quadrupoles is restricted due to crystal symmetry [53] and are expected to be vastly reduced in intensity.

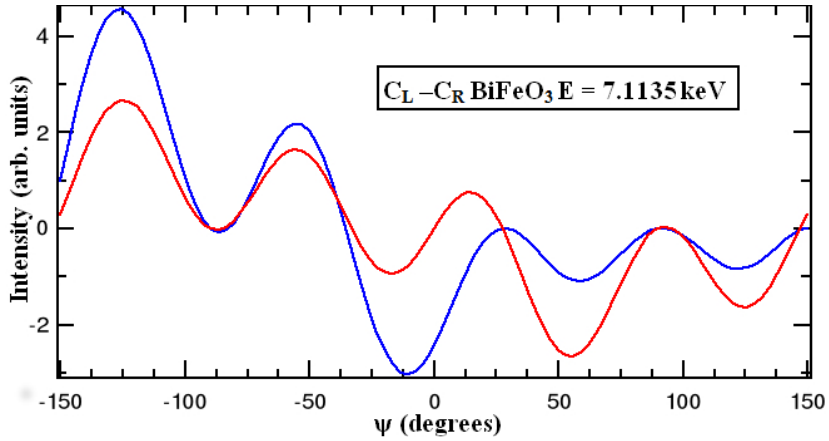

Figure 6.5 Simulation of the dichroic signal from Templeton-Templeton scattering under circular polarized x-rays for the reflection $(0,0,9)_H$ forbidden in $R3c$ at the Fe K-edge. (Red line) Above and (blue line) below T_N $(640K)$.

With the rotated channel contribution $\pi'\sigma$ form equation (6) in article IV the data was fitted obtaining the values displayed in Table 6.1 for the different multipoles present in the calculations. Due to its dependence with the K odd range multipoles the value of v was fixed to zero for the paramagnetic phase. The chiral property of the model that is presented in this work can be confirmed by a predicted contribution to intensity induced by circular polarization in the primary beam; the intensity in question is an outcome of matching chirality (helicity) in electronic structure and photons used in diffraction. The relevant intensity can be expressed in terms of unit-cell structure factors [87],

$$Im[(F_{\sigma'\pi})^* F_{\sigma'\sigma} + (F_{\pi'\pi})^* F_{\pi'\sigma}] = 2\,cos\theta\,cos\psi\,(v\,sin\theta - cos\theta\,sin\psi)$$
$$\times\,(t\,cos\theta\,sin\psi + u\,cos^3\theta\,cos(3\psi) - v\,sin\theta) \qquad (6.6)$$

where the coefficients u, t and v are relations between the different tensors in the calculations $[u = 3Re\langle T^4_{+3}\rangle/(\Psi^2_{+1}\sqrt{2}), t = i\,\Psi^2_{+2}/\Psi^2_{+1}$ and $v = \Psi^1_{+1}/(2\Psi^2_{+1})]$. Note that the expression (6.6) does not vanish for $v = 0$, so resonant reflections have circular polarization dependence above T_N. A simulation of a possible Templeton-Templeton scattering using circular polarized light is shown in Figure 6.5 for both temperatures, above and below, T_N. In a future stage this experiment will be performed at DLS using a single crystal of biFeO$_3$ previously saturated to define a single ferroelectric domain.[4] The values used to simulate these scans are the refined multipoles from Table 6.1.

6.2 Article IV

Reprinted from

JOURNAL OF THE PHYSICAL SOCIETY OF JAPAN

JOURNAL OF THE PHYSICAL SOCIETY OF JAPAN

http://jpsj.jpap.jp/

LETTER

Chiral Properties of $BiFeO_3$ Inferred from Resonant X-ray Bragg Diffraction

Angel RODRIGUEZ-FERNANDEZ, Stephen William LOVESEY, Stephen Patrick COLLINS, Gareth NISBET, and Jesus Angel BLANCO

J. Phys. Soc. Jpn. **83** (2014) 013706

© 2014 The Physical Society of Japan

Person-to-person distribution by the author only. Not permitted for publication for institutional repositories or on personal Web sites.

Journal of the Physical Society of Japan **83**, 013706 (2014) **Letters**
http://dx.doi.org/10.7566/JPSJ.83.013706

Chiral Properties of $BiFeO_3$ Inferred from Resonant X-ray Bragg Diffraction

Angel Rodriguez-Fernandez[1]*, Stephen William Lovesey[2,3], Stephen Patrick Collins[3], Gareth Nisbet[3], and Jesus Angel Blanco[1]

[1]*Physics Department, University of Oviedo, C/ Calvo Sotelo s/n Oviedo, Spain*
[2]*ISIS Facility, STFC, Oxfordshire OX11 0QX, U.K.*
[3]*Diamond Light Source Ltd., Oxfordshire OX11 0DE, U.K.*

(Received October 25, 2013; accepted November 15, 2013; published online December 9, 2013)

A new chiral phase of ferric ions in bismuth ferrite ($BiFeO_3$), the only material known to support multiferroic behaviour at room temperature, is inferred from extensive sets of data gathered by resonant x-ray diffraction. Values of all ferric multipoles participating in a minimal model of Fe electronic structure are deduced from azimuthal-angle scans. Paramagnetic (700 K) and magnetically ordered (300 K) phases of a single crystal of $BiFeO_3$ have been studied with x-rays tuned near to the iron K-edge (7.1135 keV). At both temperatures, intensities at a Bragg spot forbidden in the nominal space-group, $R3c$, are consistent with a chiral motif of ferric ions in a circular cycloid propagating along $(1, 1, 0)_H$. Templeton and Templeton scattering at 700 K is attributed in part to charge-like quadrupoles in a cycloid. The contribution is not present in a standard, simplified model of electronic states of the resonant ion with trivial cylindrical symmetry.

An electronic state in which charge and magnetic polarizations coexist has been at the centre of materials science in the past decade. Such a state exists in bismuth ferrite ($BiFeO_3$) at room temperature, while in all other known cases a multiferroic state emerges upon cooling. This makes bismuth ferrite a unique candidate for potential application in electronic devices, such as sensors or multi-state memory storage-units.[1–4] We have detected a new chiral phase of $BiFeO_3$ in the paramagnetic phase using resonant x-ray Bragg diffraction and, by way of a test for the chirality property, we demonstrate that our proposed electronic structure allows coupling to radiation with a like property, namely, x-rays with circular polarization (helicity). Moreover, our extensive sets of diffraction data enable us to infer values of ferric multipoles in both the paramagnetic and magnetically ordered phases.

Bismuth ferrite forms in a rhombohedrally distorted perovskite crystal structure of $R3c$-type (♯161). Weak ferroelectricity develops below a Curie temperature $T_c \approx 1100$ K, and G-type antiferromagnetic order of ferric (Fe^{3+}) dipole moments is observed below a Néel temperature $T_N \approx 640$ K. The antiferromagnetism coexists with a long-period modulation (≈620 Å) in the hexagonal plane, as shown in Fig. 1.[5,6] This coexistence is a curious property of a quite simple compound, created by the tension between two interactions that favor parallel and orthogonal spin arrangement, respectively.

For studies of electronic magnetism, the experimental technique of resonant x-ray Bragg diffraction we use has advantages over non-resonant diffraction that is difficult to exploit quantitatively, because uncertainty surrounds the deployment of a scattering length asymptotically valid in the Compton region of scattering.[7–11] Resonant x-ray diffraction has proved its worth in many studies, particularly those that focus on one or more of the raft of electronic properties driven by angular anisotropy in valence states.[12,13] Intensities collected at weak, space-group forbidden reflections access directly information about complex electronic structure manifest in atomic multipoles, including, magnetic charge (or magnetic monopole),[14] electric dipole,[15] anapole,[16,17] quadrupole,[18] octupoles,[19,20] and hexadecapoles.[21,22] In consequence, weak reflections are extremely sensitive to charge, orbital and spin electron degrees of freedom and $BiFeO_3$, with a chemical structure similar to haematite, is no exception.[23]

Crystal growth was performed in platinum crucibles with content of about 90 g, using the accelerated rotation technique, and a platinum cover welded tightly to the crucible, leaving only a central hole of 0.1 mm diameter, as explained in reference.[24] The size of the sample was about $5 \times 5\,mm^2$ and a thickness of 0.5 mm, showing a polished surface in the $[0, 0, l]_H$ direction.

Our hexagonal crystal coordinates are $\mathbf{a}_h = a(1, 0, 0)$, $\mathbf{b}_h = a(-1/2, \sqrt{3}/2, 0)$ and $\mathbf{c}_h = c(0, 0, 1)$, with $a = 5.58$ Å and $c = 13.88$ Å.[25] Basis vectors, or principal crystal axes, are $\xi = (1, 0, 0)$, $\eta = (0, 1, 0)$, and $\zeta = (0, 0, 1)$, and they coincide with (x, y, z) in Fig. 2 at the nominal setting of the crystal. The Bragg wavevector $(0, 0, l)_H$ is aligned with $-x$, as shown in Fig. 2. Intensities are measured as a function of rotation of the crystal about the Bragg wavevector through an angle ψ.

The $(0, 0, 9)_H$ reflection is forbidden in the nominal space group $R3c$. Bragg diffraction due to angular anisotropy in available valence states is weak but, none the less, visible in diffraction enhanced by an atomic resonance, as evident in data displayed in Fig. 3. Resonant x-ray diffraction experiments were performed at the Diamond Light Source (UK), on beamline I16. The horizontally polarized beam, σ, was tuned near the iron K-edge (7.1135 keV). We observed intensity at the $(0, 0, 9)_H$ reflection in two studies with the sample held at a temperature below (300 K) and above (700 K) the Néel temperature. The change in intensity that we observed with cooling, between the two temperatures, confirmed the magnetic origin of the difference signal; relevant data are displayed in Fig. 5. All data were collected in the rotated channel of polarization $\pi'\sigma$, where states of polarization labelled π' and σ are defined in Fig. 2. During the experiment we scanned the surface of the sample to determine the size of domains, and selected the appropriate region of the sample where a likely single domain could be involved in the scattering process. While it is possible that the sample supports different domains, the present results were consis-

©2014 The Physical Society of Japan

Person-to-person distribution by the author only. Not permitted for publication for institutional repositories or on personal Web sites.

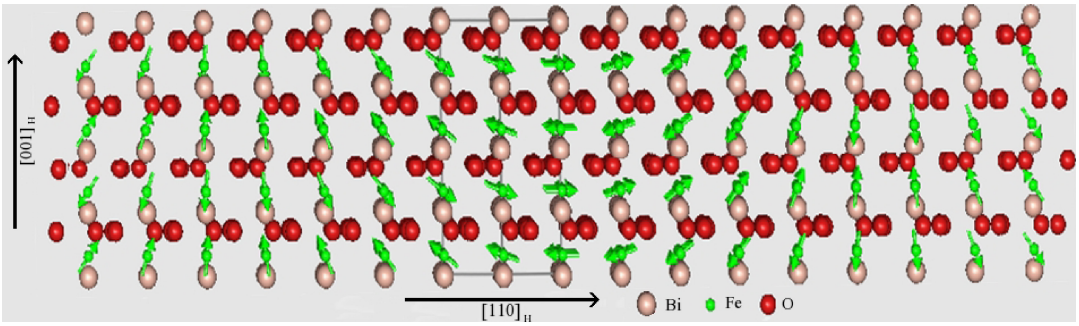

Fig. 1. (Color online) Scheme of the crystal and magnetic structures of bismuth ferrite ($BiFeO_3$), with hexagonal setting. The $[0,0,1]_H$ axis is vertical. Directions of magnetic dipoles of the Fe ions at room temperature are indicated by arrows.

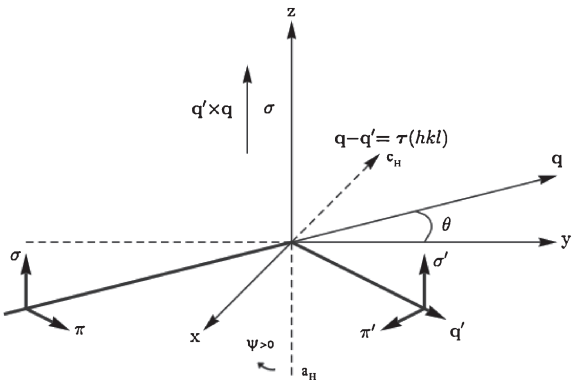

Fig. 2. Cartesian coordinates (x, y, z) and x-ray polarization and wavevectors. The plane of scattering spanned by primary ($\mathbf{q}$) and secondary ($\mathbf{q}'$) wavevectors coincides with the x–y plane. Polarization labelled σ and σ' is normal to the plane and parallel to the z-axis, and polarization labelled π and π' lies in the plane of scattering. The beam is deflected through an angle 2θ. Nominal setting of the crystal is indicated with $\mathbf{a}_h$ antiparallel to σ-polarization, together with the sense of rotation in an azimuthal-angle scan.

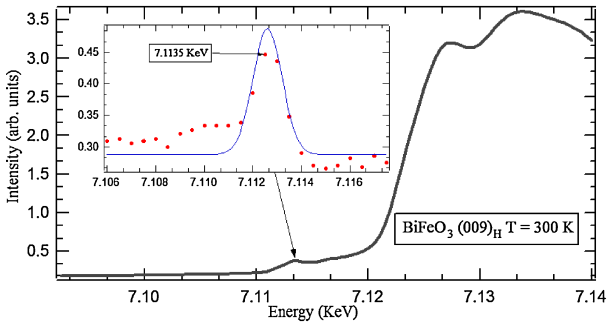

Fig. 3. (Color online) X-ray spectrum in the vicinity of the Fe K-edge for the $(0,0,9)_H$ reflection. Diffraction data reported in Figs. 4 and 5 were collected tuning the primary energy to $E = 7.1135$ keV. Inset: (red dots) Energy scan data and (blue line) approximation to a harmonic oscillator.

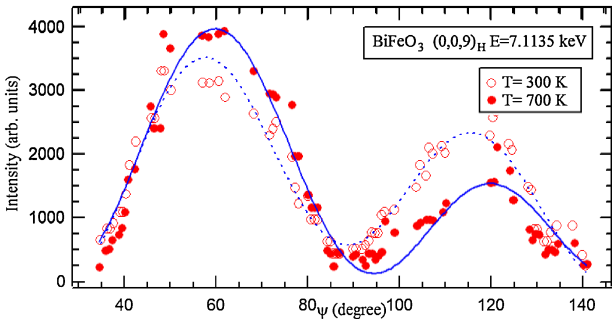

Fig. 4. (Color online) (Full dots) Intensity of the Bragg spot $(0,0,9)_H$ as a function of azimuthal angle, ψ, with a sample temperature of 700 K, forbidden in the $R3c$-type structure and called Templeton and Templeton (TT) scattering. Rotation of the crystal is counter clockwise about the Bragg wavevector, and the origin $\psi = 0$ is $\mathbf{a}_h$ antiparallel to σ-polarization, Fig. 2. (Empty dots) Intensity as a function of azimuthal angle obtained at room temperature, 300 K. Corrections to raw data are described in the text. Solid (dashed) line is a fit to our model of diffraction by a motif of charge-like quadrupoles and hexadecapoles, namely, $|F_{\pi'\sigma}|^2$ and expression (6) with $v = 0$ ($v \neq 0$).

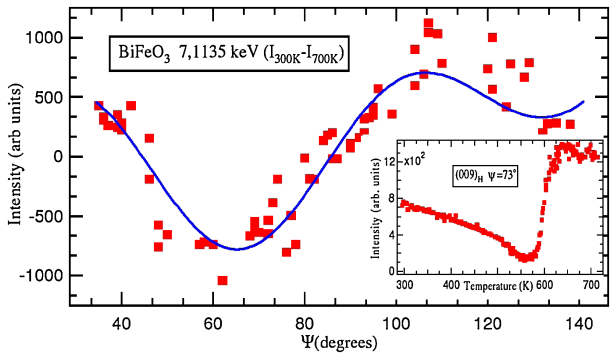

Fig. 5. (Color online) Difference of two sets of data displayed in Fig. 4, $I(v) - I(v = 0)$, together with expression (7) derived from our model of electronic structure in bismuth ferrite. Multipoles t, u, and v in (7) are set to values derived from fits to data in Fig. 4, namely, $t = +1.19 \pm 0.07$, $u = -6.20 \pm 0.16$, and $v = 0.673 \pm 0.014$. Inset: Temperature dependence of the Bragg spot $(0,0,9)_H$ at an azimuthal angle $\psi = 73°$.

tent with a single domain illuminated by the very small size of the primary beam ($180 \times 40\,\mu m^2$).

The azimuthal scans presented in Fig. 4 were obtained performing "θ scans" with the detector around the Bragg condition for different azimuthal angles. This method was used previously by Finkelstein et al.[19] and by Kokubun et al.,[26] among others. The experimental values displayed in Figs. 4 and 5 are the integrated intensity of each of the curves normalized to intensity in the primary x-ray beam. Due to the small penetration depth of an allowed Bragg spot $(0,0,6)_H$, where the diffraction is mostly following a dynamical process, we have not considered to use this kind of reflection to normalize a forbidden Bragg spot $(0,0,9)_H$ that, due to its weakness has a kinematical behaviour a larger penetration depth and less affected by possible defects from the surface.

©2014 The Physical Society of Japan

Person-to-person distribution by the author only. Not permitted for publication for institutional repositories or on personal Web sites.

All reasonable steps have been taken to arrive at sound data. Subtraction of the background intensity due to Renninger reflections (multi-beam peaks), observed in an azimuthal scan, was done using a Matlab program available at the instrument. For the case of room temperature, an azimuthal scan was done to select optimum, flat positions between peaks and avoid the Renninger effect (therefore measured points in the azimuth dependence are not equidistant). Due to the fact that we have collected resonant x-ray data for a certain selected reflection at different parts of the single crystal, we consider that the experimental data shown in Figs. 4 and 5 are related to the resonant event rather than to the tail of the Renninger effect. The high-quality crystal used for the experiment has a face perpendicular to the $(0,0,1)_{\rm H}$ direction, so the experiment was performed with a specular geometry.

We address, first, Templeton and Templeton (TT) scattering reported in Fig. 4 (filled dots) measured with the sample at 700 K ($T_{\rm N} \approx 640$ K).[27] Resonant x-ray diffraction enhanced by an electric dipole–electric dipole (E1–E1) event is forbidden at the $(0,0,9)_{\rm H}$ Bragg spot of a $R3c$-type chemical structure. Diffraction enhanced by an electric quadrupole–electric quadrupole (E2–E2) event is allowed, however, and it is produced by an electric, time-even hexadecapole. This diffraction is part of what we have observed, as we now explain.

Our notation for parity-even atomic multipoles is $\langle T^K_Q\rangle$, with a complex conjugate $\langle T^K_Q\rangle^* = (-1)^Q\langle T^K_{-Q}\rangle$, where the positive integer K is the rank and Q the projection, with $-K \le Q \le K$. Angular brackets $\langle\cdots\rangle$ denote the time average of the enclosed spherical tensor operator, i.e., multipoles are properties of the electronic ground-state, and the time-signature of $\langle T^K_Q\rangle$ is $(-1)^K$.[12,13] The hexadecapole ($K=4$) in question is the real part of $\langle T^4_{+3}\rangle$, denoted by $\langle T^4_{+3}\rangle'$. A triad axis of symmetry, C_{3z}, passes through the iron sites, 6a in $R3c$. Diffraction by these ions using a Bragg wavevector $(0,0,l)_{\rm H}$ is described by an electronic structure factor,

$$\Psi^K_Q = \left\{1 + 2\cos\left(\frac{2\pi l}{3}\right)\right\}[\langle T^K_Q\rangle + (-1)^l(-1)^K\langle T^K_{-Q}\rangle]. \quad (1)$$

Space-group allowed reflection are defined by diagonal elements Ψ^K_0 with K even, and $\Psi^K_0 \neq 0$ is allowed for $l = 6n$. The identity $C_{3z}\langle T^K_Q\rangle = \langle T^K_Q\rangle$ requires $Q = \pm 3m$. As anticipated, E1–E1 is forbidden for l odd, because, of course, $\Psi^K_0 = 0$ for a space-group forbidden reflection, while $Q = \pm 3$ does not contribute to a dipole–dipole event where K does not exceed 2. Using (1) for an E2–E2 event, we find the corresponding unit-cell structure factor is a three-fold periodic function of the azimuthal angle, ψ,[28]

$$F_{\pi'\sigma} = \left(\frac{3}{\sqrt{2}}\right)\cos^3\theta\cos(3\psi)\langle T^4_{+3}\rangle'. \quad (2)$$

In this expression, θ is the Bragg angle, and $\mathbf{a}_{\rm h}$ is antiparallel to σ-polarization, normal to the plane of scattering in Fig. 2, at the origin of an azimuthal-angle scan, $\psi = 0$. Intensity corresponding to (2), $|F_{\pi'\sigma}|^2 \propto \cos^2(3\psi)$, is symmetric about $\psi = 90°$, which does not agree with our data for TT scattering displayed in Fig. 4 (filled dots).

Missing in what has been described thus far, we propose, is TT scattering caused by charge-like quadrupoles ($K=2$) in a circular cycloid, using an E1–E1 event. An electric dipole (E1) is expected to be appreciably stronger than an electric quadrupole (E2) event. But diffraction from the quadrupoles is weak, being the responsibility of components absent in a standard stick-model, in which the electronic state of the resonant ion is restricted to cylindrical symmetry.[29] Whence, the minimal model that explains measurements in Fig. 4 (700 K, filled dots) is a sum of two forms of weak TT scattering. Adding the corresponding magnetic scattering, we achieve a model that explains data displayed in Fig. 4 (300 K, empty dots).

We invoke a (circular) cycloid with the plane of the cycloid parallel to the plane spanned by $\mathbf{c}_{\rm h}$ and $\mathbf{a}_{\rm h} + \mathbf{b}_{\rm h}$. This motif is one candidate considered by Przeniosło et al.; see Model 1 in Fig. 1.[30] We will assume that the cycloid, composed of charge-like multipoles, is constant, independent of temperature, to a good approximation. This is a sound assumption for the paramagnetic phase, and not unreasonable at lower temperatures for multipoles not induced by magnetic order.

Starting with an explanation of TT scattering in Fig. 4, we utilize quadrupoles for a circular cycloid, $\langle C^2_Q\rangle$, introduced by Scagnoli and Lovesey[28] and recently reviewed by Lovesey et al.[31] These quadrupoles, in common with all cycloid multipoles, are not subject to the symmetry operations in the point group for sites 6a in the $R3c$ group. In the general case, one finds $\langle C^2_0\rangle = 0$ for the first harmonic of the cycloid, which is the one of interest. Using orthonormal coordinates (x', y', z') with x' parallel to $\mathbf{a}_{\rm h} + \mathbf{b}_{\rm h}$ and z' parallel to $\mathbf{c}_{\rm h}$,

$$\langle C^2_{+1}\rangle = \left(\frac{1}{4}\right)[\langle T^2_{+1} + T^2_{-1}\rangle + i\langle T^2_{+2} - T^2_{-2}\rangle]$$
$$\equiv -\left(\frac{1}{\sqrt{6}}\right)[i(y'z') + (x'y')], \quad (3)$$

where $(\alpha\beta)$ is a standard, traceless second-rank Cartesian tensor. A representation of the quadrupole, $\langle\mathbf{T}^2\rangle$, in terms of standard operators is available.[32]

By way of an orientation to the result (3) we consider its value for a standard stick-model.[29] In this case, all electronic properties of the resonant ion are manufactured from one material vector. If α and β represent Cartesian coordinates, a general second-rank tensor $(\alpha\beta)$ is to be replaced by a simple product $\langle\alpha\rangle\langle\beta\rangle$, leading to $(y'z') = (x'y') = 0$ for a material vector confined to the x'–z' plane with $\langle y'\rangle = 0$.

Guided by $R3c$, we need the quadrupole (3) and the quadrupole derived from it by rotation about $(\mathbf{a}_{\rm h} + \mathbf{b}_{\rm h})$ by 180°. The sum of the two correctly related quadrupoles is transformed to principal crystal-axes with the result,

$$\Psi^2_{+1} = \sqrt{\frac{3}{2}}\left[\left(\frac{\sqrt{3}}{4}\right)\{(\xi^2 - \eta^2) + 3(\zeta\zeta)\} + (\eta\zeta)\right]. \quad (4)$$

Note that Ψ^2_{+1} is purely real. Turning to data obtained with a sample temperature of 300 K and displayed in Fig. 4 (empty dots), magnetic diffraction by the cycloid is created by a time-odd dipole,

$$\langle C^1_0\rangle = \left(\frac{1}{2}\right)\left[\frac{\langle T^1_0\rangle + i\langle T^1_{+1} - T^1_{-1}\rangle}{\sqrt{2}}\right]. \quad (5)$$

For a reflection $(0,0,l)_{\rm H}$ with l odd, it actually contributes a magnetic dipole parallel to $(\mathbf{a}_{\rm h} + \mathbf{b}_{\rm h})$, namely, $\langle T^1_{-1} - T^1_{+1}\rangle/\sqrt{2}$ calculated with principal crystal axes. At the K-edge, a dipole $\langle\mathbf{T}^1\rangle$ is simply orbital angular momentum.[33]

©2014 The Physical Society of Japan

Person-to-person distribution by the author only. Not permitted for publication for institutional repositories or on personal Web sites.

We use the purely real quadrupole (4), with projections $Q = \pm 1$, as a common factor in the final expression for the unit-cell structure factor. The remaining charge-like quadrupole, $Q = \pm 2$, is accounted for in a ratio $\Psi^2_{+2}/\Psi^2_{+1} = -it$. Calculations using an ideal cycloid show that t is purely real and $t = +1$ (Scagnoli and Lovesey[28]). The contribution from the hexadecapole in (2) is captured by $u = 3\langle T^4_{+3}\rangle'/(\Psi^2_{+1}\sqrt{2})$. In the absorption profile we invoke overlap of the two events, E1–E1 and E2–E2, which occur at different energies with different widths. Lastly, the magnetic contribution to the structure factor is $v = 3\langle T^1_{-1} - T^1_{+1}\rangle/(2\Psi^2_{+1})$. Note that t, u, and v are all treated as purely real quantities to be inferred from our data. Since t and v both relate to an E1–E1 event they are nothing more than ratios of the appropriate multipoles that we have shown. On the other hand, u has to include a ratio of radial integrals for E2 and E1 events, namely, $(f[q\{R^2\}_{sd}]^2/[\{R\}_{sp}]^2)$ where $\{R\}_{sp}$ and $\{R^2\}_{sd}$, respectively, are radial integrals for E1 and E2 events at the K-edge of iron. A multiplicative factor in u, denoted here by f, measures the admixture of E1–E1 and E1–E2 events. While f might depend on energy it can be taken purely real without influencing conclusions, because it accompanies the principal harmonic (2).

Incorporating the two types of TT scattering, expressions (2) and (4), and scattering by magnetic dipoles, we arrive at a unit-cell structure factor that gives an adequate account of all our data,

$$F_{\pi'\sigma} = t\cos\theta\sin\psi + u\cos^3\theta\cos(3\psi) - i\sin\theta\cos(2\psi) - v(\sin\theta - i\cos\theta\sin\psi). \quad (6)$$

Writing $I(v) = |F_{\pi'\sigma}(v)|^2$ the difference in intensity at the two temperatures is,

$$I(v) - I(v=0) = v[v(1 - \cos^2\theta\cos^2\psi) - \sin 2\theta(t\sin\psi + u\cos^2\theta\cos(3\psi) + \cos(2\psi)\sin\psi)]. \quad (7)$$

Fits of $I(0)$ to data for TT scattering displayed in Fig. 4 (700 K, filled dots) yield values $t = +1.19 \pm 0.07$, which is close enough to the ideal value to give great confidence, and $u = -6.20 \pm 0.16$. A fit of $I(v)$ to data gathered at 300 K, Fig. 4 (empty dots), yields $v = 0.673 \pm 0.014$ for the magnetic dipole, with t and u set to aforementioned values. For completeness, we show in Fig. 5 difference data, taken from Fig. 4, together with the appropriate expression for intensity (7) evaluated with our estimates of the three multipoles.

We bring our Letter to a close with a survey of our observations and the interpretation we construct. Above the Néel temperature, $T_N \approx 640$ K, our azimuthal-angle data are adequately explained by a model with minimal complexity. It includes TT scattering from charge-like quadrupoles and hexadecapoles. A contribution by quadrupoles heralds a new chiral phase, in which quadrupoles participate in a circular cycloid. A test of chirality in electronic structure is to see whether or not it couples to circular polarization (helicity) in the x-ray beam. An expression for intensity associated with circular polarization (helicity) in the primary beam, I_c, is derived from our unit-cell structure factors[22] and we arrive at,

$$I_c = \mathrm{Im}[(F_{\sigma'\pi}) * (F_{\sigma'\sigma}) + (F_{\pi'\pi}) * (F_{\pi'\sigma})] = 2\cos\theta\cos\psi[v\sin\theta - \cos\theta\sin\psi] \times (t\cos\theta\sin\psi + u\cos^3\theta\cos(3\psi) - v\sin\theta). \quad (8)$$

In expression (8), t and u are charge-like multipoles, which generate TT scattering, and v is a magnetic dipole absent above T_N. Values of the three multipoles, t, u, and v, are inferred from data displayed in Fig. 4, collected above and below the Néel temperature, that are adequately described by $|F_{\pi'\sigma}|^2$ derived from (6). Note that expression (8) does not vanish for $v = 0$, meaning resonant reflections are affected by circular polarization above T_N with a hitherto unknown phase of the material.

Existence of TT scattering by quadrupoles in a cycloid implies that the actual chemical structure belongs to an enantiomorphic crystal class lacking a centre of symmetry. Space-group $R3$ (♯146), one of 65 members of the Sohncke sub-group of crystal structures, is a maximal non-isomorphic subgroup of the nominal $R3c$-group, and thus a likely candidate for a commensurate chiral motif in bismuth ferrite. In which case, a chiral motif and a single domain are implied for the magnetically-ordered state, and this does appear to be the case.[34] A high-quality crystal, from which satellite peaks can be resolved, should show satellite intensity above T_N. The domain pattern of propagation vectors should be reproduced on temperature cycling above and below T_N since they are driven by the pre-aligned quadrupoles. This issue could be checked using circular polarized x-rays, due to the helicity properties of this kind of x-rays.

Parallel scenarios merit a mention, e.g., the weak itinerant ferromagnet MnSi, and related materials.[35–37] The compounds use a cubic group $P2_13$ (♯198), and exist in both right- and left-handed enantiomorphs. A single-valued handedness persists in the ferromagnetic and paramagnetic phases,[38] with chiral fluctuations in MnSi above the Curie temperature observed by inelastic neutron scattering.[39] Notably, a standard example for spontaneous homochirality, sodium chlorate ($NaClO_3$), forms in the chemical structure described by $P2_13$.[40]

MnSi has a Curie temperature $T_c \approx 29.5$ K, and deep in the paramagnetic phase spin fluctuations are isotropic. Perhaps more relevant to the present discussion of bismuth ferrite is another iron-based chiral magnet. FeGe, iso-structural with MnSi, has a high Curie temperature, $T_c \approx 278.2$ K, and precursor activity is well-established.[37,41] Ferromagnetic spirals have a period ≈180 Å (MnSi) and ≈700 Å (FeGe), to be compared with a period ≈620 Å in bismuth ferrite. On its own, an antisymmetric exchange-interaction (Dzialoshinskii–Moriya) will promote an orthogonal arrangement of spins that can disturb an arrangement of parallel spins, supported by an isotropic Heisenberg exchange plus relatively weak magnetic anisotropy.

Quadrupoles (also higher-order multipoles) as a primary order-parameter is not unusual. However, again, order is achieved at low temperatures, because the underlying mechanism is weak.[21,42–44]

The origin of the charge-like quadrupoles that contribute TT scattering could be related to bismuth 6s–6p lone pairs, known to drive certain structural distortions. Apart from expected direct hybridization of lone pairs, there is scope for admixture through the agency of oxygen 2p states that contribute to angular anisotropy in valence states observed at iron sites.

Lastly, we examine the possibility that our azimuthal-angle scan at 700 K can be explained by the parity-odd event E1–

©2014 The Physical Society of Japan

Person-to-person distribution by the author only. Not permitted for publication for institutional repositories or on personal Web sites.

E2 using the $R3c$-group, in addition to E2–E2.[12,28] We find polar multipoles, $\langle U_Q^K \rangle$, do not contribute intensity to the $(0,0,9)_H$ Bragg spot in channels with unrotated polarization, $\sigma'\sigma$ and $\pi'\pi$. The contribution from E1–E2 in the $\pi'\sigma$ channel of immediate interest comes from a purely real polar quadrupole, namely, $i(3/\sqrt{5})\cos^2\theta\langle U_0^2\rangle$ that is added to the hexadecapole contribution (2). The two contributions to the unit-cell structure factor, E1–E2 plus E2–E2, are in phase quadrature, so there can be no interference between them to lift the pure six-fold periodicity in the E2–E2 contribution to intensity that is lacking in Fig. 4 (filled dots).

In summary, Bragg diffraction intensities at the nominally forbidden reflection $(0,0,9)_H$ of bismuth ferrite, observed below and above the Néel temperature, are consistent with a chiral structure formed by a circular cycloid propagating along $[1,1,0]_H$ not previously detected in the paramagnetic phase. The new chiral phase is responsible for some Templeton and Templeton (TT) scattering at 700 K due to charge fluctuations not contained in the plane of the cycloid. Our extensive sets of azimuthal-angle diffraction data have been used to infer good values of three atomic multipoles involved in the scattering process. A satisfactory minimal model of Fe electronic structure includes a quadrupole (E1–E1 event) and a hexadecapole (E2–E2 event) contributing TT scattering, plus a magnetic dipole (E1–E1).

Acknowledgments We acknowledge the Diamond Light Source for the beam-time allocation on I16. We have benefited from discussions and correspondence on the question of normalization of our data with Dr. K. Finkelstein. One of us (SWL) is grateful to Dr. D. D. Khalyavin and Dr. K. S. Knight for valuable discussion about the explanation of results offered in the communication. We are also grateful with G. Catalan, who has provided the single crystal for performing the experiment. Financial support has been received from Spanish FEDER-MiCiNN Grant No. Mat2011-27573-C04-02. One of us (ARF) is grateful to Gobierno del Principado de Asturias for the financial support from Plan de Ciencia, Tecnología e innovación (PTCI) de Asturias. We thank Diamond Light Source for access to beamline I16 (MT7720) that contributed to the results presented here.

*angelrf86@gmail.com

1) A. M. Kadomtseva, A. K. Zvezdin, Y. F. Popov, A. P. Pyatakov, and G. P. Vorob'ev, JETP Lett. **79**, 571 (2004).
2) G. Catalan and J. F. Scott, Adv. Mater. **21**, 2463 (2009).
3) J. F. Scott, Adv. Mater. **22**, 2106 (2010).
4) D. C. Arnold, K. S. Knight, G. Catalan, S. A. T. Redfern, J. F. Scott, P. Lightfoot, and F. D. Morrison, Adv. Funct. Mater. **20**, 2116 (2010).
5) D. Lebeugle, D. Colson, A. Forget, M. Viret, A. M. Bataille, and A. Gukasov, Phys. Rev. Lett. **100**, 227602 (2008).
6) S. Lee, T. Choi, W. Ratcliff, R. Erwin, S.-W. Cheong, and V. Kiryukhin, Phys. Rev. B **78**, 100101 (2008).
7) F. de Bergevin and M. Brunel, Acta Crystallogr., Sect. A **37**, 314 (1981).
8) D. Gibbs, G. Grübel, D. R. Harshman, E. D. Isaacs, D. B. McWhan, D. Mills, and C. Vettier, Phys. Rev. B **43**, 5663 (1991).
9) S. W. Lovesey, Rep. Prog. Phys. **56**, 257 (1993).
10) H. C. Walker, F. Fabrizi, L. Paolasini, F. de Bergevin, J. Herrero-Martin, A. T. Boothroyd, D. Prabhakaran, and D. F. McMorrow, Science **333**, 1273 (2011).
11) V. E. Dmitrienko, K. Ishida, A. Kirfel, and E. N. Ovchinnikova, Acta Crystallogr., Sect. A **61**, 481 (2005).
12) S. W. Lovesey, E. Balcar, K. S. Knight, and J. Fernández-Rodríguez, Phys. Rep. **411**, 233 (2005).
13) S. W. Lovesey and E. Balcar, J. Phys. Soc. Jpn. **82**, 021008 (2013).
14) S. W. Lovesey and V. Scagnoli, J. Phys.: Condens. Matter **21**, 474214 (2009).
15) J. Fernández-Rodríguez, J. A. Blanco, P. J. Brown, K. Katsumata, A. Kikkawa, F. Iga, and S. Michimura, Phys. Rev. B **72**, 052407 (2005).
16) S. W. Lovesey, J. Fernández-Rodríguez, J. A. Blanco, D. S. Sivia, K. S. Knight, and L. Paolasini, Phys. Rev. B **75**, 014409 (2007).
17) J. Fernández-Rodríguez, V. Scagnoli, C. Mazzoli, F. Fabrizi, S. W. Lovesey, J. A. Blanco, D. S. Sivia, K. S. Knight, F. de Bergevin, and L. Paolasini, Phys. Rev. B **81**, 085107 (2010).
18) S. B. Wilkins, R. Caciuffo, C. Detlefs, J. Rebizant, E. Colineau, F. Wastin, and G. H. Lander, Phys. Rev. B **73**, 060406(R) (2006).
19) K. Finkelstein, Q. Shen, and S. Shastri, Phys. Rev. Lett. **69**, 1612 (1992).
20) S. W. Lovesey and K. S. Knight, J. Phys.: Condens. Matter **12**, L367 (2000).
21) Y. Tanaka, T. Inami, S. W. Lovesey, K. S. Knight, F. Yakhou, D. Mannix, J. Kokubun, M. Kanazawa, K. Ishida, S. Nanao, T. Nakamura, H. Yamauchi, H. Onodera, K. Ohoyama, and Y. Yamaguchi, Phys. Rev. B **69**, 024417 (2004).
22) J. Fernández-Rodríguez, S. W. Lovesey, and J. A. Blanco, Phys. Rev. B **77**, 094441 (2008).
23) S. W. Lovesey, A. Rodríguez-Fernández, and J. A. Blanco, Phys. Rev. B **83**, 054427 (2011).
24) R. Palai, R. S. Katiyar, H. Schmid, P. Tissot, S. J. Clark, J. Robertson, S. A. T. Redfern, G. Catalan, and J. F. Scott, Phys. Rev. B **77**, 014110 (2008).
25) A. Palewicz, I. Sosnowska, R. Przeniosło, and A. Hewat, Acta Phys. Pol. A **117**, 296 (2010).
26) J. Kokubun, A. Watanabe, M. Uehara, Y. Ninomiya, H. Sawai, N. Momozawa, K. Ishida, and V. E. Dmitrienko, Phys. Rev. B **78**, 115112 (2008).
27) D. H. Templeton and L. K. Templeton, Acta Crystallogr., Sect. A **41**, 365 (1985); D. H. Templeton and L. K. Templeton, Acta Crystallogr., Sect. A **42**, 478 (1986).
28) V. Scagnoli and S. W. Lovesey, Phys. Rev. B **79**, 035111 (2009).
29) J. P. Hannon, G. T. Trammell, M. Blume, and D. Gibbs, Phys. Rev. Lett. **61**, 1245 (1988) [Erratum **62** 2644 (1989)].
30) R. Przeniosło, M. Regulski, and I. Sosnowska, J. Phys. Soc. Jpn. **75**, 084718 (2006).
31) S. W. Lovesey, V. Scagnoli, M. Garganourakis, S. M. Koohpayeh, C. Detlefs, and U. Staub, J. Phys.: Condens. Matter **25**, 362202 (2013).
32) S. W. Lovesey and E. Balcar, J. Phys.: Condens. Matter **9**, 8679 (1997).
33) P. Carra, B. T. Thole, M. Altarelli, and X. Wang, Phys. Rev. Lett. **70**, 694 (1993).
34) R. D. Johnson, P. Barone, A. Bombardi, R. J. Bean, S. Picozzi, P. G. Radaelli, Y. S. Oh, S.-W. Cheong, and L. C. Chapon, Phys. Rev. Lett. **110**, 217206 (2013).
35) M. Ishida, Y. Endoh, S. Mitsuda, Y. Ishikawa, and M. Tanaka, J. Phys. Soc. Jpn. **54**, 2975 (1985).
36) V. A. Dyadkin, S. V. Grigoriev, D. Menzel, D. Chernyshov, V. Dmitriev, J. Schoenes, S. V. Maleyev, E. V. Moskvin, and H. Eckerlebe, Phys. Rev. B **84**, 014435 (2011).
37) H. Wilhelm, M. Baenitz, M. Schmidt, C. Naylor, R. Lortz, U. K. Rößler, A. A. Leonov, and A. N. Bogdanov, J. Phys.: Condens. Matter **24**, 294204 (2012).
38) V. Dmitriev, D. Chernyshov, S. Grigoriev, and V. Dyadkin, J. Phys.: Condens. Matter **24**, 366005 (2012).
39) B. Roessli, P. Böni, W. E. Fischer, and Y. Endoh, Phys. Rev. Lett. **88**, 237204 (2002).
40) C. Viedma and P. Cintas, Chem. Commun. **47**, 12786 (2011).
41) E. Moskvin, S. Grigoriev, V. Dyadkin, H. Eckerlebe, M. Baenitz, M. Schmidt, and H. Wilhelm, Phys. Rev. Lett. **110**, 077207 (2013).
42) P. Morin, D. Schmitt, and E. du Tremolet de Lacheisserie, J. Magn. Magn. Mater. **30**, 257 (1982).
43) T. Sakakibara, T. Tayama, T. Onimaru, D. Aoki, Y. Onuki, H. Sugawara, Y. Aoki, and H. Sato, J. Phys.: Condens. Matter **15**, S2055 (2003).
44) Y. Kuramoto, H. Kusunose, and A. Kiss, J. Phys. Soc. Jpn. **78**, 072001 (2009).

©2014 The Physical Society of Japan

Chapter 7

Conclusions

As presented along this thesis work, Resonant X-ray Diffraction has been shown as a magnificent tool in the study of complex electron correlated systems.

- In the case of Neptunium Dioxide, NpO_2, the technique has evidence existence of an antiferromagnetic phase, similar to the one presented in UO_2, below the transition temperature T_0 = 25 K. REXS is capable of observing small distortions in the ordering of the Np ions, predicted by Nuclear Magnetic Resonance (NMR) produced by the displacement of the oxygen atoms to two non-equivalent positions. Proving the power of this technique in these types of cases where other techniques as neutron probes or Mössbauer experiments were not able to observe the magnetic ordering.
- In Hematite, α-Fe_2O_3, it was observed how the non-reducible tensor formalism helps to analyzed the azimuthal dependence of the experimental data gathered near the iron K-edge for both forbidden reflections from the $(0,0,l)_H$ family; together with the demonstration of the coupling between the chiral properties of the material and the circular polarized x-rays in the primary beam, as predicted in the theory due to the Newmann's principle.
- For multiferroic Bismuth Ferrite, $BiFeO_3$, a possible change in the symmetry of the iron ions has been inferred in the paramagnetic phase by performing T&T scans. This new phase related to the action of the charge quadrupoles in a cycloid implies a chemical

structure that belongs to an enantiomorphic crystal class lacking a centre of symmetry. Space-group R3 (#146), one of 65 members of the Sohncke sub-group, is a maximal non-isomorphic subgroup of the nominal R3c-group, and thus a likely candidate for a commensurate chiral motif in bismuth ferrite.

It is clear from the results shown in this thesis that Resonant Elastic X-ray Scattering has much to offer in the investigation of exotic order parameters and particularly in distinguishing different contributions to the scattered intensity as illustrated in α-Fe_2O_3. Although no definitive conclusions may be drawn in some cases, the information provided by resonant X-ray diffraction offers a unique element, site and valence probe to study electronic ordering phenomena in complex materials and furthermore delivers information on the electronic structure of condensed matter.

Conclusiones

Como se ha mostrado a lo largo de este trabajo de tesis, la Dispersión Resonante de rayos X se presenta como una herramienta magnifica para el estudio de sistemas complejos electrónicamente correlacionados.

- En el caso del dióxido de neptunio, NpO_2, la técnica ha confirmado la existencia de una fase antiferromagnética, similar a la presentada por el compuesto UO_2 por debajo de la temperatura de 25 K. Información de esta fase no había sido posible ser inferida por otras técnicas como las sondas de neutrones u otros experimentos convencionales de rayos x. Siendo capaz de observar pequeñas distorsiones en el ordenamiento de los iones de Np, predichas por Resonancia Magnética Nuclear, producidas por desplazamientos de los átomos de oxígenos a dos posiciones no equivalentes.
- En la hematita, α-Fe_2O_3, se observó como el formalismo basado en tensores no reducibles, definido en la sección 2.4, ayuda a mejorar la extracción de la información de los datos experimentales obtenidos cerca del borde K del hierro para ambas reflexiones prohibidas de la familia $(0,0,l)_H$. Además de demostrar el acoplamiento entre las propiedades quirales de los materiales y los rayos x circularmente polarizados en el haz primario, como se predecía en la teoría debido al principio de Newmann.
- En la multiferroica ferrita de bismuto, $BiFeO_3$, se ha detectado un posible cambio en la simetría de los iones de hierro en la fase paramagnética mediante los barridos Templeton & Templeton. Esta nueva fase relacionada con la acción de los quadrupoles debidos a la carga en la cicloide implica una estructura química que pertenece a una clase de cristal enantiomórfico que carece de un centro de simetría. El grupo de espacio R3 (#146), uno de los 65 miembros del subgrupo de Sohncke, es un subgrupo máximo no-isomórfico del

grupo de espacio nominal R3c, y que es un buen candidato para producir este motivo quiral conmensurable en la ferrita de bismuto.

De los resultados mostrado en esta tesis es claro que la dispersión resonante de rayos X tiene mucho que ofrecer en la investigación de parámetros de orden exóticos y en particular en la distinción de diferentes contribuciones a la intensidad de dispersión como se demostró en α-Fe_2O_3. Aunque no se pueden extraer conclusiones definitivas en algunos casos, la información proporcionada por la dispersión resonante de rayos X ofrece una sonda única para estudiar elementos, sitios y valencias de fenómenos de ordenamiento electrónico en compuestos complejos y mas allá dando información de la estructura electrónica de la materia condensada.

Appendix A

Dzyaloshinskii-Moriya interaction

In the last decade one of the focuses in condensed matter physics has been the study of materials that presents magnetoelectric effect or skyrmion states [88, 89]. These materials show a twist in their magnetic moments or spins (see Figure A.1) that can be described using the anisotropic exchange interaction also known as Dzyaloshinskii-Moriya (DM) interaction.

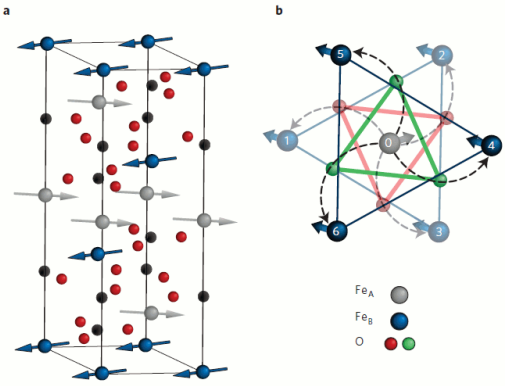

Figure A.1 Atomic and magnetic structure of $FeBO_3$, (a) hexagonal unit cell with magnetic motif, two sublattices of iron are presented in different colors (blue and grey). (b) Top view of the same structure, presenting the two sublattice separated by the oxygen triangles. The figure was taken from Dmitrieko et al. [11].

Dzyaloshinskii and Moriya presented in their works [30, 31] a formalism for describing the interaction between atomic magnetic moments. The coupling between the spin moments, according to Neumann's principle and because is a property of the material, must possess all the symmetries of the material. This coupling can be reduced by shielding [90] or improved due to the action of other ions as oxygen atoms [91].

$$\Delta E = S_i^1 S_j^2 M_{ij} = J S_i^1 S_j^2 \delta_{ij} + S_i^1 S_j^2 M_{ij}^S + S_i^1 S_j^2 M_{ij}^A. \quad (A.1)$$

The coupling between two spins can be described, with Cartesian tensors components, using a second rank tensor M_{ij} in the classical Hamiltonian as in (A.1). This tensor can be divided in three contributions (A.2), an isotropic (scalar) exchange term, an anisotropic exchange term and an antisymmetric term. This last term describes the DM interaction and can be described with a vector $D = M_{ij}^A$ together with the vector product of the two spins.

$$\Delta E = J S_i^1 S_j^2 \delta_{ij} + S_i^1 S_j^2 M_{ij}^S + S_i^1 S_j^2 M_{ij}^A. \quad (A.2)$$

In equation (A.3) the two important contributions for the spin coupling are presented, the isotropic term, JS^1S^2, is the dominant term in the coupling interaction, the one that prefers being a parallel or antiparallel coupling of the spins, while the second term produce a small tilting of the moments creating the canted phases common in the weak ferromagnets or other materials that show the DM interaction.

$$\Delta E = J S^1 S^2 + D[S^1 \times S^2]. \quad (A.3)$$

This DM interaction appears in the case of 3d transition metal oxides because in the case of these compounds the strong interaction between first neighbours, which dominates the exchange interactions. The DM interaction in these cases is around the 1% of the isotropic coupling. Producing a large electric polarization in magnetoelectric materials [92, 93] in the case of spontaneous ordering of the DM ions, leading to a weak ferromagnetic signal that easily couples to an external magnetic field [94].

As previously said, the presence of oxygen atoms can be essential for the DM interaction to take place. In R$\bar{3}$c structures, as Fe_2O_3 or $FeBO_3$ (presented in Figure A.1), the Oxygen atoms break the R$\bar{3}$m symmetry, which do not allow this kind of coupling interaction, so in the case of the absence of this atom or their delocalization to the positions in the middle of the magnetic ions the DM interaction won't be strong to appear. Dmitrienko and co-workers presented a new procedure to define the sign of this interaction [11].

Appendix B

Parity-even Tensors, T^K_Q

Parity even tensors, T^K_Q, are used to described parity even events as pure E1 (charge-dipole) and E2 (charge-quadrupole) processes. The time average value of this tensors, $\langle T^K_Q \rangle = \langle \Psi | T^K_Q | \Psi \rangle$, is a linear combination of elements of the matrix $\langle \mathrm{JM} | T^K_Q | \mathrm{JM}' \rangle$. Like $\left(T^K_Q\right)$ is a spherical tensor its matrix elements satisfy the Wigner-Eckart theorem, as in [56, 57]

$$\langle JM | T^K_Q | JM' \rangle = (-1)^{J-M} \begin{pmatrix} J & K & J' \\ -M & Q & M' \end{pmatrix} \left(J \| T^K_Q \| J'\right), \qquad (B.1)$$

where we can substitute $\left(J \| T^K_Q \| J'\right)$, the reduced matrix element for equivalent electrons in an atomic shell with angular momentum l, for the equivalent electrons as $\sqrt{8\pi}(l \| Y^K \| l) W^{(0K)K}$. This term can be written using a 3j-symbol as

$$(l \| Y^K \| l) = (-1)^l (2l+1) \left[\frac{2K+1}{4\pi}\right]^{1/2} \begin{pmatrix} l & K & l \\ 0 & 0 & 0 \end{pmatrix}, \qquad (B.2)$$

where the unit tensor $W^{(0K)K}$ depends on the quantum numbers SLJ, S'L'J' and it is tabulated for large number of 3d ions, $W^{(0K)K}$ are introduced in more detail in work by Judd et al [57]. The properties from the 3j-symbol only permit even K for allowing the matrix to be different to zero, as presented by Lovesey et al. [95].

The reduced matrix elements have the form $(t\bar{J}j \| V^K \| t'\bar{J}j')$ that using Edmonds's book relation (7.1.7) is proportional with $(t \| V^K \| t')$ with coefficients depending of $\bar{J}$, j and j' [56]. This dependence can be written as

$$(lj\|V^K\|l'j') = \left(\frac{5}{6}\right)^{\frac{1}{2}}(2\bar{J}+1)\begin{Bmatrix} j & t & \bar{J} \\ \bar{l} & s & l \end{Bmatrix}\begin{Bmatrix} j' & t' & \bar{J} \\ \bar{l} & s' & l' \end{Bmatrix}(t\bar{J}j\|V^K\|t'\bar{J}j') \quad (B.3)$$

where the spin s (s') of the electron is ½ and the value for $t(t')$ is 1 (2). It is possible to write the tensor Y_Q^K as a linear combination of atomic quantities that depend on both the spin (that are absent in the reduced matrix element near the K-edge) and orbital variables associated with the resonant ion. As the materials were studied near the K-edge, I will just focus on the orbital part. Marri and Carra develop both the spin and the orbital properties [96].

The general expression for the reduced matrix element for even transitions E1E1 and E2E2 following ref [97] is

$$(J\|T^K\|J') = \mp(2\bar{J}+1)\sum_{ab}(-1)^b\,(2a+1)(2b+1)W^{(ab)K} \times \begin{Bmatrix} \frac{1}{2} & \bar{l} & \bar{J} \\ \bar{l} & \frac{1}{2} & a \end{Bmatrix}\begin{Bmatrix} t & \bar{l} & l \\ t & \bar{l} & l \\ K & a & b \end{Bmatrix}. \quad (B.4)$$

The reduced element from (B.1) is obtained from (B.4) selecting t to be equal to 1. The sign $\mp$ is related to the total angular momentum from the core label $\bar{J} = \bar{l} \pm 1/2$ as $(-1)^{1/2+\bar{l}+\bar{J}}$. The value of the 9j-symbol, as has 2 lines equals is zero if $K + a + b$ is an odd integer [56, 57], and a just can be 0 or 1. The dependence with the quantum numbers from the valence states $|JM\rangle$ and $|J'M'\rangle$ appears through the unit tensor $W^{(ab)K}$.

The expressions for the sum rules of the dichroic signal presented in chapter 2.4 can be derived from (B.4) taking $\bar{J} = \bar{l} - 1/2$ and $\bar{J} = \bar{l} + 1/2$ taking t=1 or t=2 for the parity even events E1 or E2, respectively.

For specific values of a,b and K the unit tensor $W^{(ab)K}$ can be written in terms of R, S and L. As $\langle S\rangle \sim W^{(10)1}$, $\langle L\rangle \sim W^{(01)1}$, $\langle 3R(R\cdot S) - S\rangle \sim W^{(12)1}$ and $\langle 3L_z^2 - L(L+1)\rangle \sim W^{(02)2}$.

When in (B.4) it is sum tow absorption edges $\bar{J} = \bar{l} - 1/2$ and $\bar{J} = \bar{l} + 1/2$ the value for a is restricted to 0, due to this it is not possible to obtain information of the spin angular momentum in a resonant ion. The resulting state as presented by Thole et al [98] is

$$\sum_{\bar{J}}(J\|T^K\|J') = [2(2K+1)]^{1/2} W^{(0K)K} \begin{Bmatrix} t & K & t \\ l & \bar{l} & l \end{Bmatrix} \qquad (B.5)$$

An important application to the Bragg scattering from (b.5) is obtained when $\bar{l} = 0$, this represents the K edge of the resonant ion. When $\bar{l} = 0$ the total angular momentum is $\bar{J} = 1/2$ and $t = l$ giving as a result

$$(J\|T^K\|J') = (-1)^K \frac{\{2(2K+1)\}^{1/2}}{(2l+1)} W^{(0K)K}. \qquad (B.6)$$

This can be applied to the 3d transition elements ions when taking into account non-coupling states, $|SM_S LM_L\rangle = \sum_{\mathrm{JM}}(SM_S LM_L|\mathrm{JM})\,|\mathrm{JM}\rangle$. In this case the Wigner-Eckart theorem is applied to the spin and orbital states separately. For the K edge, as it is only observed the orbital angular moment for the valence states, the elements of $\mathrm{T}^{\mathrm{K}}_{\mathrm{Q}}$ are diagonal with the spin quantum numbers. For $\bar{l} = 0$ and $t = l$

$$\langle SM_S LM_L \left| T^K_Q \right| S'^{M_{S'}} L'^{M_{L'}} \rangle = \delta_{M_S M_{S'}} \delta_{SS'}$$

$$\times \frac{(-1)^K}{(2l+1)} \left\{ \frac{2}{2S+1} \right\}^{1/2} W^{(0K)} (-1)^{L-M_L} \begin{pmatrix} L & K & L \\ -M_L & Q & M_L{}' \end{pmatrix} \qquad (B.7)$$

This result define the expression of the expected values for the parity even tensors $\langle \mathrm{T}^{\mathrm{K}}_{\mathrm{Q}} \rangle$ in terms of $\langle L \rangle$, $\langle Q \rangle$ and $\langle \Lambda \rangle$ (dipole, quadrupole and octupoles), where the quadrupole is defined in terms of $\{3l_0^2 - l(l-1)\}/2$ and the octupoles operator is defined as $\Lambda = 1/2 \sum_j \{l_0(5l_0^2 - 3l(l+1) + 1)\}_j$.

$$\langle T^1_q \rangle = \frac{-\sqrt{3}}{(2l+1)(l\|l\|l)} \langle L_q \rangle, \qquad (B.8)$$

$$\langle T^2_q \rangle = \frac{2\sqrt{5}}{(2l+1)(l\|l\|l)\{(2l-1)(2l+3)\}^{1/2}} \langle Q_q \rangle \qquad (B.9)$$

$$\langle T^3_q \rangle = \frac{-2\sqrt{7}}{(2l+1)(l\|l\|l)\{(l-1)(2l-1)(l+2)(2l+3)\}^{1/2}} \langle \Lambda_q \rangle \qquad (B.10)$$

It is important to note that for a K-edge absorption from a resonant ion $t = l$ and in the case of an ion 3d must be an E2 type.

Appendix C

Parity-odd Tensors, G^K_Q and U^K_Q

For the case of parity-odd events as dipolar-charge quadrupolar-charge (E1E2) and dipolar-charge dipolar-magnetic (E1M1) the reduced matrix elements presented in chapter 2.4, Υ^K_Q can be written as happen in the case of the parity-even case in term of the reduced matrix element $\left(t\bar{J}j\|V^K\|\mathrm{t}'^{\bar{J}j'}\right)$ where V^K only affect the t being possible to write the reduced matrix as $(t\|V^K\|\mathrm{t}')$ and a coefficient proportional to $\bar{J}$, j and j'. With these we obtain the same result as in (B.3)

$$(lj\|Y^K\|l'j') = \left(\frac{5}{6}\right)^{\frac{1}{2}}(2\bar{J}+1)\begin{Bmatrix} j & t & \bar{J} \\ \bar{l} & s & l \end{Bmatrix}\begin{Bmatrix} j' & t' & \bar{J} \\ \bar{l} & s' & l' \end{Bmatrix}(t\bar{J}j\|V^K\|t'\bar{J}j') \quad (C.1)$$

where $t = 1$ and $t' = 2$. Using the algebra methods is possible to develop the reduced matrix element as a linear combination of atomic quantities that depend on both the spin and orbital variables associated with the resonant ions [97]. As in the parity-even processes, the spin variables are absent in the reduced matrix element at the K-edge where $\bar{l} = 0$. Marri and Carra develop both spin and the orbital properties, but in this case will be only interesting the orbital properties of V^K.

The magnetoelectric tensors, G^K_Q, and polar tensors, U^K_Q, used for describing parity odd events as the dipolar-charge quadrupolar-charge (E1E2) and dipolar-charge dipolar-magnetic (E1M1) processes are constructed in terms of the angular momentum operator, $\boldsymbol{L}$, the polar unit vector $\boldsymbol{n}$, and the orbital anapole,

$$\boldsymbol{\Omega} = i\,(\boldsymbol{L}^2\boldsymbol{n} - \boldsymbol{n}\boldsymbol{L}^2). \quad (C.2)$$

Table C.1 Representation of G_Q^K and U_Q^K. The numerical factors are calculated from $(t\|V^K\|\mathrm{t}') = -\mathrm{i}^{\mathrm{K}}(t\|\mathrm{G}^K\|\mathrm{t}') = -\mathrm{i}^{\mathrm{K}}(t\|\mathrm{U}^K\|\mathrm{t}') = (2\mathrm{K}+1)^{1/2}$ with $t = 1, t' = 2$.

K	G_Q^K,	U_Q^K,
1	$\frac{1}{4}\left(\frac{3}{2}\right)^{1/2}\Omega_Q$,	$-\left(\frac{3}{2}\right)^{1/2}\mathrm{n}_Q$,
2	$-\left(\frac{5}{2}\right)^{1/2}\left(\mathrm{L}_Q\otimes\mathrm{n}_Q\right)^2$,	$-\frac{1}{4}\left(\frac{5}{2}\right)^{1/2}\left(\mathrm{L}_Q\otimes\Omega_Q\right)^2$,
3	$-\frac{1}{4}\left(\frac{5}{2}\right)^{1/2}\left(\mathrm{L}_Q\otimes\left(\mathrm{L}_Q\otimes\mathrm{n}_Q\right)^2\right)^3$,	$\left(\frac{5}{2}\right)^{1/2}\left(\mathrm{L}_Q\otimes\left(\mathrm{L}_Q\otimes\mathrm{n}_Q\right)^2\right)^3$,

In this point, it is important remember some of the properties of this operators. The angular momentum, $\boldsymbol{L}$, is diagonal with respect to the angular momentum states and $\langle lm|L_\alpha|l'm'\rangle$, while $\langle lm|n_\alpha|l'm'\rangle$ is different from zero for $l' = l \pm 1$. The basic commutation relations are $[L_\alpha, R_\beta] = i\epsilon_{\alpha\beta\gamma}R_\gamma$ where R_β denotes the one of the operators ($\boldsymbol{L}$, $\boldsymbol{n}$ or $\boldsymbol{\Omega}$) and $\epsilon_{\alpha\beta\gamma}$ is the antisymmetric unit tensor of rank three. Commutation relations for spherical components of $\boldsymbol{L}$, $\boldsymbol{n}$ and $\boldsymbol{\Omega}$ are readily constructed, e.g. $[L_0, \boldsymbol{L}^2] = 0$, $[L_0, n_{\pm1}] = \pm n_{\pm1}$ and $[L_0, \Omega_{\pm1}] = \pm\Omega_{\pm1}$. One finds that $\boldsymbol{L}\cdot\boldsymbol{n} = \boldsymbol{L}\cdot\boldsymbol{\Omega} = 0$, while $-\boldsymbol{\Omega}\cdot\boldsymbol{n} = \boldsymbol{n}\cdot\boldsymbol{\Omega} = 2i$. The operators L_α, n_α and Ω_α are all Hermitian. With relation with the time-reversal, L_α and Ω_α are odd (i.e., $\bar{L}_\alpha = -L_\alpha$ and $\bar{\Omega}_\alpha = -\Omega_\alpha$) and n_α is even (i.e., $\bar{n}_\alpha = -n_\alpha$).

In table C.1 is presented the relations between the G_Q^K and U_Q^K tensors with this operators. Concerning the influence on operator equivalents of the inversion, or parity, operator let us note first that all components of a given tensor operator have the same parity if the parity operator commutes with rotations. Secondly, the parity of a tensor operator built from tensor products, as is the case for G_Q^K amd U_Q^K with K>1, is the product of the parities of the constituent tensor operators. Odd-rank tensors are true tensors and even-rank tensors are axial tensors. Some og the properties of the parity-odd tensor are listed in Table C.2.

Table C.2 Properties of G_Q^K and U_Q^K.

Time-reversal:	
$\bar{G}_Q^K = (-1)^{1+\mathrm{Q}}G_{-Q}^K$,	$\bar{U}_Q^K = (-1)^{\mathrm{Q}}U_{-Q}^K$,
Hermitian conjugation:	
$\left(G_Q^K\right)^+ = (-1)^{\mathrm{Q}}G_{-Q}^K$,	$\left(U_Q^K\right)^+ = (-1)^{\mathrm{Q}}U_{-Q}^K$,

The anapole operator, Ω, is inversion-odd and time-odd. An anapole moment characterizes a system that does not transform into itself under space inversions [99]. A system like this generates a distribution of magnetic fields which is quite different from parity-even multipoles, such as dipole or quadrupole moments. The magnetic field distribution of an anapole looks like the magnetic field created by a current flowing in a toroidal winding, and the field is completely confined inside the winding.

Appendix D

Principal Axes

When doing calculations, sometimes is more convenient in physics to work in a set of Cartesian axes different to the crystal axes or the diffraction geometry axes. It is possible to label another set of Cartesian axes with coordinates (ξ, η, ζ) where the symmetry properties will be easier to handle. This set of coordinates is related to the reference frame (Crystal or Diffraction geometry) by the Euler angles α, β and γ by the Wigner D-functions, [56, 68]

$$\langle T_Q^K \rangle = \sum_q \langle T_q^K \rangle_{(\xi,\eta,\zeta)} D_{Q,q}^K(-\gamma, -\beta, -\alpha) \qquad (C.1)$$

where $\langle T_q^K \rangle_{(\xi,\eta,\zeta)}$ is the value of the spherical tensor in the set of axes defined by (ξ, η, ζ) and $D_{Q,q}^K(-\gamma, -\beta, -\alpha)$ denotes the rotation matrix. The set of axes (ξ, η, ζ) that makes $\langle T_q^K \rangle$ is diagonal is known as principal axes for $\langle T_q^K \rangle$. This set of axis has the property of vanishing for $\langle T_q^K \rangle$ unless q = 0.

The Wigner D-functions have the orthogonality property that can be expressed as $D_{Q,q}^K(-\gamma, -\beta, -\alpha) = \left(D_{q,Q}^K(\alpha, \beta, \gamma)\right)^*$ and can be written in terms of the $d_{q,Q}^K(-\beta)$, the Wigner d-functions as $D_{Q,q}^K(-\gamma, -\beta, -\alpha) = e^{iq\alpha} d_{Q,q}^K(\beta) e^{iQ\gamma}$. With this we can write again (C.1) as

$$\langle T_Q^K \rangle = e^{iQ\gamma} \sum_q e^{iq\alpha} d_{Q,q}^K(\beta) \langle T_q^K \rangle_{(\xi,\eta,\zeta)} \qquad (C.2)$$

The definition of this D-functions can been well followed in the book by Varshalovich et al. [68].

Appendix E

Stokes Parameters

In the case of partial polarized radiation the variations and correlations between components of the electric field can only be described statistically using a coherency matrix

$$\Psi = \langle \varepsilon \cdot \varepsilon^* \rangle \qquad (E.1)$$

where angular brackets denote averaging over many wave cycles.

The coherency matrix contains all second order statistical information about the polarization. This matrix can be decomposed into the sum of two idempotent matrices, corresponding to the eigenvectors of the coherency matrix, each representing a polarization state that is orthogonal to the other. An alternative decomposition is into completely polarized (zero determinant) and unpolarized (scaled identity matrix) components. In either case, the operation of summing the components corresponds to the incoherent superposition of waves from the two components. The latter case gives rise to the concept of the "degree of polarization"; i.e., the fraction of the total intensity contributed by the completely polarized component.

$$P_0 = I$$

$$P_1 = pIsin(2\psi)cos\,(2\chi)$$

$$P_2 = pIsin\,(2\chi)$$

$$P_3 = pIcos(2\psi)cos\,(2\chi) \qquad (E.2)$$

The Stokes parameters are a set of values, first defined by George G. Stokes in 1852 [100], which describe the degree of polarization of a radiation wave. This parameters are a mathematical representation of the intensity (I), the degree of polarization (p) and the shape parameters of the polarization ellipse described by ψ (which described that any polarization ellipse is indistinguishable from one rotated by 180º) and χ (which is related to the indistinguishablility between two polarizations with the semi-axis lengths swapped accompanied by a 90º rotation. Note that the notation for the Stokes parameters used in this work follow the definition of the Pauli matrix as presented in (E.2) [38, 48] and our parameters P_1, P_2, and P_3 correspond to P_2, P_3, and P_1, respectively, in the work of Mazzoli *et al.* [70].

Figure E.1 represent the Poncaré sphere, which is the spherical surface occupied by completely polarized states in the space of the Poincaré vector.

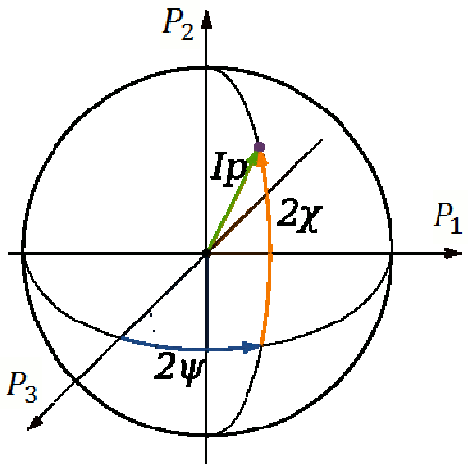

Figure E.1 Poncaré sphere.

The Stokes parameters contain all of the information of the coherency matrix,

$$\Psi = \frac{1}{2}\sum_j P_j \sigma_j \qquad (E.3)$$

where σ_j denote the Pauli matrices,

$$\sigma_0 = \begin{bmatrix} 1 & 0 \\ 0 & 1 \end{bmatrix}, \sigma_1 = \begin{bmatrix} 0 & 1 \\ 1 & 0 \end{bmatrix}, \sigma_2 = \begin{bmatrix} 0 & -i \\ i & 0 \end{bmatrix} \text{ and } \sigma_3 = \begin{bmatrix} 1 & 0 \\ 0 & -1 \end{bmatrix} \qquad (E.4)$$

Appendix F

Cr_2O_3, Magnetoelectricity in $R\bar{3}c$ Compounds

Chromium sesquioxide, Cr_2O_3, presents its antiferromagnetic properties below 310 K, its Néel temperature [101], showing a magnetoelectric behaviour where a magnetic polarization can be induced by a electric field or a electric polarization generated by the application of a magnetic field [102, 103]. Cr_2O_3 is a member of the corundum family ($R\bar{3}c$ space group) with cell parameters a=4,96Å and c=13,599Å; and the Cr ions occupying 12c Wyckoff positions while the oxygen ions are located in 18e, as present in Figure F.1.

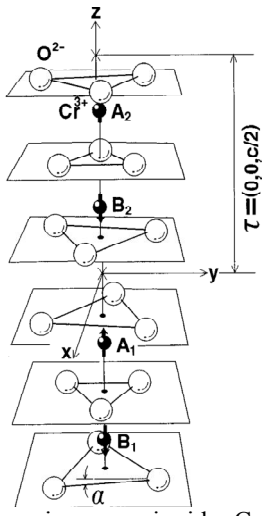

Figure F.1 Atomic structure of the chromium sesquioxide, Cr_2O_3, in the hexagonal setting. Figure obtained from [102].

In this appendix I will apply the formalism presented in section 2.4 to the case of this magnetoelectric compound that was studied with Resonant X-ray Diffraction by Kokubun and co-workers in their work [32]. As it is explained in

this work they performed Templeton and Templeton scans near the K-edge of the Cr (5.9890 keV) for two forbidden reflections $(003)_H$ and $(009)_H$.

$$\Psi_Q^K = (e^{i\varphi l} + (-1)^{K+l} e^{-i\varphi l})\left[\langle T_Q^K\rangle + (-1)^l \langle T_{-Q}^K\rangle\right].$$

$$\Psi_Q^{K,g} = (e^{i\varphi l} + (-1)^{l} e^{-i\varphi l})\left[\langle G_Q^K\rangle + (-1)^{K+l} \langle G_{-Q}^K\rangle\right]$$

$$\Psi_Q^{K,g} = (e^{i\varphi l} - (-1)^{l} e^{-i\varphi l})\left[\langle U_Q^K\rangle - (-1)^{K+l} \langle U_{-Q}^K\rangle\right] \qquad (F.1)$$

As previously was presented in the case of a Germanium crystal (section 2.4.5). It is possible to define the amplitudes to scattering for a forbidden reflection as the $(003)_H$ and $(009)_H$ for the corundum family taking into account the location of the Cr ions in the unit cell, as present in Figure F.1 there are four Cr ions laying along the c-axis. Positions A_1 and B_1 (A_2 and B_2) are related by a spatial inversion while the relations between locations A1 and B2 are related by the presence of a rotation of π at the position denoted as y. Using Table 2.6, it is easy to arrive to the cell structure factor presented in (F.1) for the different tensors.

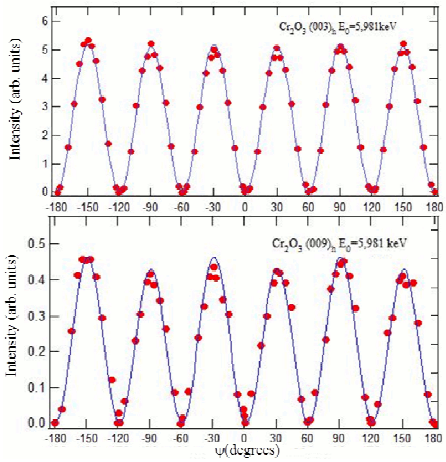

Figure F.2 Azimuthal dependence of two forbidden reflections (top) $(003)_H$ and (bottom) $(009)_H$. The red dots represent the experimental data obtained by Kokubun et al. [32] while the blue line presents the fitting using the formalism presented in the previous sections.

We can then obtain the amplitudes to scattering for the different processes as present in (F.2) for E2E2 and (F.3) for mixed event E1E2. And with it fit the azimuthal dependence Figure F.2 getting the values for the tensors presented in Table F.1.

$$F_{\sigma'\sigma}(E2E2) = i\sqrt{2}\,cos(3\psi)\,sin(2\theta)\,cos(\varphi l)\,Re(\langle T_3^3\rangle)$$

$$F_{\pi'\sigma}(E2E2) = \frac{i}{2\sqrt{2}}\{[3\,cos(3\theta) + cos(\theta)]\,sin(3\psi)\,cos(\varphi l)\,Re(\langle T_3^3\rangle)$$

$$+ [cos(3\theta) + 3\,cos(\theta)]\, sin(\varphi l)\, cos(3\psi)\, Re(\langle T_3^4 \rangle)\}$$

$$F_{\pi'\pi}(E2E2) = -\frac{i}{\sqrt{2}} cos(3\psi)\, sin(4\theta)\, cos(\varphi l)\, Re(\langle T_3^3 \rangle) \qquad (F.2)$$

$$F_{\sigma'\sigma}(E1E2) = -i\frac{4\sqrt{2}}{\sqrt{5}} cos(3\psi)\, cos(\theta)\, sin(\varphi l)\, Im(\langle G_3^3 \rangle)$$

$$F_{\pi'\sigma}(E1E2) = i\frac{2\sqrt{2}}{\sqrt{5}} sin(3\psi)\, sin(2\theta)\, sin(\varphi l)\, Im(\langle G_3^3 \rangle) + \frac{2i}{\sqrt{5}} cos(\varphi l) cos^2\,(\theta) \langle U_0^2 \rangle$$

$$F_{\pi'\pi}(E1E2) = \frac{i}{2\sqrt{10}} cos(3\psi)\, [cos(3\theta) - cos(\theta)]\, sin(\varphi l)\, Im(\langle G_3^3 \rangle) \qquad (F.3)$$

Table F.1 Values for the tensors obtain from the fitting perform to Kokubun et al. [32] data using the formalism of spherical tensors. The value of the tensor $Im\langle G_3^3 \rangle$ was set to 1.

Tensor	Value
$\langle U_0^2 \rangle$	-0.01
$Re\langle T_3^3 \rangle$	1.13
$Re\langle T_3^4 \rangle$	-0.01

Appendix G

Intermediate States

The amplitudes of the channels for resonant X-ray scattering and absorption consist of products of many electron matrix elements. This is related to the two steps process we are considering, where the electron in the fundamental state $|\mu\rangle$ is first excited to the valence shell and immediately decay to the fundamental core state $|\mu'\rangle$ by the re-emission of the x-ray photon. These initial and final states are described by the quantum numbers $SLJM$ and $S'L'J'M'$, respectively.

The intermediate state $|\eta\rangle$ (with quantum numbers $S^\eta L^\eta J^\eta M^\eta$) contains two active shells, where is host the ejected photoelectron that has to be coupled to the SL of the electrons of the initial valence shell. One can define the new spin and orbital quantum numbers for the valence state S^x, L^x assuming a implicitly coupling as $s \oplus S^x \Rightarrow S^\eta$ and $l \oplus L^x \Rightarrow L^\eta$.

The sum over intermediate states denoted by $\sum_{\eta(\Delta)}$ introduced in the formalism for the calculation of the different events, can be calculated leaving intact the dependence of the products of matrix elements on selected quantum numbers as in [49, 50, 104]. To perform this calculation properly, one would have to resort to the graphical methods for n_j-symbols as presented in [95]. Due to the Wigner-Eckart theorem the product of matrix elements for the E1 transition will contain a product of two 3j-symbols,

$$(-1)^{J-M}\begin{pmatrix} J & 1 & J^\eta \\ -M & q & M^\eta \end{pmatrix}(-1)^{J^\eta - M^\eta}\begin{pmatrix} J^\eta & 1 & J' \\ -M^\eta & q & M' \end{pmatrix} \qquad (H.1)$$

and a product of reduced matrix elements [105],

$$\left(SLJM\middle\|\sum R_q^1\middle\|S^\eta L^\eta J^\eta M^\eta\right)\left(S^\eta L^\eta J^\eta M^\eta\middle\|\sum R_q^1\middle\|S'L'J'M'\right) \qquad (H.2)$$

In (H.2) it is necessary to remember that for the values of S^{η} and L^{η} need the fact that the core hole, with quantum number s and $\bar{l}$, must be coupled with the valence electrons, with quantum number S^{η} and L^{η}. The nj-symbols from the products in (H.1) and (H.2) can be rewritten to perform the summations over S^{η}, L^{η} and J^{η} introducing a new additional quantum label K resulting a product of two 3j-symbols

$$(-1)^{J-M}\begin{pmatrix} J & 1 & J' \\ -M & q & M' \end{pmatrix}(-1)^{K-Q}\begin{pmatrix} K & 1 & 1 \\ -Q & q' & q' \end{pmatrix}, \qquad (H.3)$$

and a product of three 6j-symbols,

$$\begin{Bmatrix} J & K & J' \\ L' & S & L \end{Bmatrix}\begin{Bmatrix} L & K & L' \\ l & L^{X} & l \end{Bmatrix}\begin{Bmatrix} l & K & l \\ 1 & \bar{l} & 1 \end{Bmatrix}. \qquad (H.4)$$

The first 3j-symbol in (H.3) is the Wigner-Eckart signature of a matrix element for a tensor of rank K. The first 6j-symbol in (H.4) is the signature of a reduced matrix element for a tensor of rank k that acts only on the orbital part of the wave function. The second 6j-symbol in (H.4) is an important ingredient in the definition of $\left(SL\middle\|\mathrm{V}^{(\mathrm{K})}\middle\|\mathrm{S'J'}\right)$, as defined by Judd [57], which represents the corresponding unit tensor.

For the introduction of the total angular momentum, $\bar{J}$, is necessary to describe a re-coupling between the core hole and the valence electrons. This introduces two 9 j-symbols

$$\left(SLJM\middle\|\sum R_q^1\middle\|\bar{J}J^{\times}J^{\eta}M^{\eta}\right)\left(\bar{J}J^{\times}J^{\eta}M^{\eta}\middle\|\sum R_q^1\middle\|S'L'J'M'\right), \qquad (H.5)$$

This nj-symbols can be summed over $J^{\times}$and J^{η}. For simplifying this sum we can introduce the quantum numbers a, b and K. The 3j-symbols obtained in this way are the same as the ones in (H.3) and three 6j-symbols together with two 9j-symbols

$$\begin{Bmatrix} S & S' & a \\ L & L' & b \\ J & J' & K \end{Bmatrix}\begin{Bmatrix} S & a & S' \\ s & S^{\times} & s \end{Bmatrix}\begin{Bmatrix} L & K & L' \\ l & L^{X} & l \end{Bmatrix}\begin{Bmatrix} 1 & \bar{l} & l \\ 1 & \bar{l} & l \\ K & a & b \end{Bmatrix}\begin{Bmatrix} \bar{l} & K & \bar{l} \\ s & \bar{J} & s \end{Bmatrix}. \qquad (H.6)$$

The first 9j-symbol represents the signature of a coupled tensor operator of rank K acting on both spin and orbital b components. The following two 6j-symbols are related to the construction of the unit tensor $W^{(ab)}$, if summed over S^{η} and L^{η}.

References

[1] U. Staub, Y. Bodenthing, C. Piamonteza, M. García-Fernández, V. Scagnoli, M. Garganourakis, S. Koohpayeh, D. Fort and S. W. Lovesey, *Phys. Rev. B,* vol. 80, p. 140410, 2009.

[2] C. Zeng, T. Li, A. Das, N. L. Rosi and R. Jin, *J. Am. Chem. Soc.,* vol. 135, no. 10011, 2013.

[3] S. P. Collins, S. W. Lovesey and E. Balcar, *J. Phys.: Condens Matter,* vol. 19, p. 213201, 2007.

[4] P. Duke, Syncrotron Radiation, Oxford: Oxford University Press, 2000.

[5] D. H. Templeton and L. K. Templeton, *Phys. Rev. B.,* vol. 49, no. 14580, 1994.

[6] D. H. Templeton and L. K. Templetron, *Acta Crystallogr. Sect. A.,* vol. 53, no. 352, 1997.

[7] V. Scagnoli, U. Staub, Y. Bodenthin, R. A. de Souza, M. García-Fernández, M. Garganourakis, A. T. Boothroyd, D. Prabhakaran and S. W. Lovesey, *Science ,* vol. 332, no. 696, 2011.

[8] H. Wadati, J. Geck, E. Schierle, R. Sutarto, F. He, D. G. Hawthorn, M. Nakamura, M. Kawasaki, Y. Tokura and G. A. Sawatzky, *New J. Phys.,* vol. 16, p. 033006, 2014.

[9] S. W. Lovesey, K. S. Knight and E. Balcar, *J. Phys.: Condens. Matter,* vol. 19, no. 376205, 2007.

[10] H. C. Walker, F. Fabrizi, L. Paolasini, F. de Bergevin, J. Herrero-Martin, A. T. Boothroyd, D. Prabhakaran and D. F. McMorrow, *Science,* vol. 333, no. 1273, 2011.

[11] V. E. Dmitrienko, E. N. Ovchinnikova, S. P. Collins, G. Nisbet, G. Beutier and Y. O. Kvashnin, *Nature Physics,* vol. 10, no. 202, 2014.

[12] R. D. Johnson, P. Barone, A. Bombardi, R. J. Bean, S. Picozzi, P. G. Radelli, Y. S. Oh, S. W. Cheong and L. C. Chapon, *Rev. Phys. Lett.,* vol. 110, p. 217206, 2013.

[13] S. W. Lovesey, J. Fernandez-Rodriguez, J. A. Blanco, D. S. Sivia, K. S. Knight and L. Paolasini, "Lovesey S W, Fernández Rodríguez J, Blanco J A, Sivia D S, Knight K S and Paolasini L," *Phys.Rev.B,* vol. 75, no. 014409, 2007.

[14] G. R. Stewart, *Rev. Mod. Phys.,* vol. 83, p. 1589, 2011.

[15] H. Winick and S. Doniach, "Synchrotron Radiation Research," New York, Plenum Press, 1980, p. 754.

[16] J. Als-Nielsen, M. Altareli, J. Baruchel, R. Currat, B. Faok, A. Fontaine, T. Forstyth, A. Freund, G. Krill, M. Lambert, G. McIntyre, F. Mexei, J. Morse, J. Pannetier, D. Raoux, R. Scherm, M. Schlenker, G. Schmahl, C. Williams

and H. Zabel, Neutron and Synchrotron Radiation for Condensed Matter Studies, Berlin: Springer, 1993.

[17] J. Als-Nielsen and D. McMorrow, "Elements of Modern X-ray Physics," London, John Wiley & Sons, LTd, 2001.

[18] F. de Bergevin and M. Brunel, *Phys. Lett. A,* vol. 39, no. 141, 1972.

[19] T. R. Thurston, G. Helgesen, J. P. Hill, D. Gibbs, B. Gaulin and P. J. Simpson, *Phys. rev. B,* vol. 49, no. 15730, 1994.

[20] D. H. Templeton and L. K. Templeton, *Acta Crystallogr. Sect. A,* vol. 41, no. 133, 1985.

[21] V. E. Dmitrienko, *Acta Crystallogr. Sect. A,* vol. 39, no. 29, 1983.

[22] N. Hampton, G. A. Saunders, J. H. Harding and A. M. Stoneham, *J. Nucl. Mat.,* vol. 149, p. 18, 1987.

[23] R. Caciuffo, G. Amoretti, P. Santini, G. H. Lander, J. Kulda and P. De V. Du Plessis, *Phys. Rev. B,* vol. 59, p. 13892, 1999.

[24] J. M. Friedt, F. J. Litterst and J. Rebizant, *Phys. Rev. B,* vol. 32, p. 257, 1985.

[25] W. Kopmann, F. J. Litterst, H. H. Klauss, M. Hillberg, W. Wagener, G. M. Kalvius, E. Schreier, F. J. Burghart, J. Rebizant and G. H. Lander, *J. Alloys Compd,* vol. 271, p. 463, 1998.

[26] J. A. Paixao, C. Detlefs, M. J. Longfield, R. Caciuffo, P. Santini and N. Bornhoeft, *Phys. Rev. Lett.,* vol. 89, p. 187202, 2002.

[27] Y. Tokunaga, Y. Homma, S. Kambe, D. Aoki, H. Sakai, E. Yamamoto, A. Nakamura, Y. Shiokawa, R. E. Walstedt and H. Yasuoka, *Phys. Rev. Lett,* vol. 94, p. 137209, 2005.

[28] R. Caciuffo, J. A. Paixao, C. Detlefs, M. J. Longfield, P. Santini, N. Bernhoeft, J. Rebizant and G. H. Lander, *J. Phys.: Condens. Matter,* vol. 15, no. S2287, 2003.

[29] S. W. Lovesey, C. Detlefs and A. Rodríguez-Fernández, *J. Phys.: Condens. Matter,* vol. 24, no. 256009, 2012.

[30] I. Dzyaloshinsky, *J. Phys. Chem. Solids,* vol. 4, no. 241, 1958.

[31] T. Moriya, *Phys. Rev.,* vol. 120, no. 91, 1960.

[32] J. Kokubun, A. Watanabe, M. Uehara, Y. Ninomiya, H. Sawai, N. Momozawa, K. Ishida and E. Dmitrienko, "Nobuyuki Momozawa, and Kohtaro Ishida Vladimir E. Dmitrienko," *PHYSICAL REVIEW B,* vol. 78, 2008.

[33] K. D. Finkesltein, Q. Shen and S. Shastri, *Physical Review Letters,* vol. 69, no. 1612, 1992.

[34] A. M. Kadomtseva, A. K. Zvezdin, Y. F. Popov, A. P. Pyatakov and G. P. Vorob'ev, *JETP Lett.,* vol. 79, no. 571, 2004.

[35] G. Catalan and J. F. Scott, *Adv. Matter,* vol. 21, no. 2463, 2009.

[36] J. F. Scott, *Adv. Mater.,* vol. 22, no. 2106, 2010.

[37] D. C. Arnold, K. S. Knight, Catalan, G., S. A. T. Redfern, J. F. Scott, P. Lightfoot and F. D. Morrison, *Adv. Funct. Mater.,* vol. 20, no. 2116, 2010.

[38] S. W. Lovesey and S. P. Collins, "X-Ray Scattering and Absorption by Magnetic Materials," Oxford, Oxford Science Publications, 1996.

[39] "International Tables of Crystallography," Dordrecht, TH. Hahn, 1983.

[40] H. Grotch, E. Kazes, G. Bhatt and D. A. Owen, *Phys. Rev. A,* vol. 27, p. 243, 1983.

[41] G. Bhatt, H. Grotch, E. Kazes and D. A. Owen, *Phys. Rev. A,* vol. 28, p.

2195, 1983.

[42] S. W. Lovesey, K. S. Knight and D. S. Sivia, *Phys. Rev. B,* vol. 65, p. 224402, 2002.

[43] P. Kane, *Phys. Reports,* vol. 218, p. 67, 1992.

[44] F. Bell, J. Felsteiner and L. P. Pitaevskii, *Phys. Rev. A,* vol. 53, p. R1213, 1996.

[45] M. J. Cooper, X-ray Compton Scattering, Oxford: Oxford University Press, 2004.

[46] K. Namikawa, M. Ando, Nakajima, T. and H. Kawata, *J. Phys. Soc. Jpn,* vol. 54, p. 4099, 1985.

[47] D. Gibbs, D. R. Harshman, E. D. Issacs, D. McWhan, D. Mills and C. Vettier, *Phys. Rwv. Lett.,* vol. 61, p. 1241, 1988.

[48] L. D. Landau and E. M. Lifschitz, Quantum Electrodynamics, 2nd ed., vol. 4, Oford: Pergamon Press, 1982.

[49] B. R. Judd, *Phys. Rev.,* vol. 127, p. 750, 1962.

[50] G. S. Osfelt, *J. Chem. Phys.,* vol. 37, p. 511, 1962.

[51] S. W. Lovesey, *J. Phys.: Condens. Matter,* vol. 9, p. 7501, 1997.

[52] S. W. Lovesey, E. Balcar, C. Detlefs, G. Van der Laan, D. S. Sivia and U. Staub, *J. Phys.: Condens. Matter,* vol. 15, p. 4511, 2003.

[53] J. P. Hannon, G. T. Trammell, M. Blume and D. Gibbs, *Phys. Rev. Lett.,* vol. 61, p. 1245, 1988.

[54] J. Luo, G. T. Trammell and J. P. Hannon, *Phys. Rev. Lett.,* vol. 71, p. 287, 1993.

[55] P. Carra and B. T. Thole, *Rev. Mod. Phys.,* vol. 66, p. 1509, 1994.

[56] A. R. Edmonds, Angular Momentum in Quantum Mechanics, Princeton: Princeton University Press, 1960.

[57] B. R. Judd, Operator Techniques in Atomic Spectroscopy, New York: McGraw-Hill, 1963.

[58] A. Abragam and B. Bleaney, Electron Paramagnetic Resonance of Transition Ions, Oxford: Clarendon Press, 1970.

[59] K. Yoshida, Theory of Magnetism, Berlin: Springer, 1996.

[60] I. S. Elfinov, N. A. Skarikov, V. I. Anisimov and G. A. Sawatzky, *Phys. Rev. Lett.,* vol. 88, p. 015504, 2002.

[61] S. Di Matteo, Y. Joly, A. Bombardi, L. Paolasini, F. de Bergevin and C. R. Natoli, *Phys. Rev. Lett.,* vol. 91, p. 257402, 2003.

[62] S. W. Lovesey and V. Scagnoli, *J. Phys.: Condens. Matter,* vol. 21, p. 474214, 2009.

[63] V. Scagnoli and S. W. Lovesey, *Phys. Rev. B,* vol. 79, p. 035111, 2009.

[64] L. Paolasini, C. Detlefs, C. Mazzoli, S. Wilkins, P. P. Deen, A. Bombardi, N. Kernavanois, F. de Bergevin, F. Yakhou, J. P. Valade, I. Breslavetz, A. Fondacaro, G. Pepellin and P. Bernard, *Syncrotron Radiation,* vol. 14, p. 301, 2007.

[65] E. N. Ovchinnikova and V. E. Dmitrienko, *Acta Crystallogr., Sect. A,* vol. 56, p. 2, 2000.

[66] S. W. Lovesey, K. S. Knight and E. Balcar, *Phys. Rev. B,* vol. 64, p. 054405, 2001.

[67] Y. Tanaka, T. Inami, T. Nakamura, H. Yamauchi, H. Onodeta, K. Ohoyama and Y. Yamaguechi, *J. Phys.: Condens. Matter,* vol. 11, p. L505, 1999.

[68] D. A. Varshalovich, A. N. Moskalev and V. K. Khersonskii, Quamtum Theory of Angular Momentum, Singapore: World Scientific, 1988.

[69] H. C. Walker, R. Caciuffo, D. Aoki, F. Bourdarot, G. H. Lander and J. Flouquet, *Phys. Rev. B,* vol. 83, p. 193102, 2011.

[70] C. Mazzoli, S. B. Wilkins, S. Di Matteo, B. Detlefs, C. Detlefs, V. Scagnoli, L. Paolasini and P. Ghigna, *Phys. Rev. B,* vol. 76, p. 195118, 2007.

[71] M. C. Martinez-Tomas, D. N. Montenegro, V. Sallet and V. Muñoz-Sanjosé, *J. Appl. Phys,* vol. 112, p. 014305, 2012.

[72] D. W. Osborne and E. F. Westrum, *J. Chem. Phys.,* vol. 21, p. 1884, 1953.

[73] R. Caciuffo, G. H. Lander, J. C. Spirlet, J. M. Fournier and W. F. Kuhs, *Solid State Commun.,* vol. 64, p. 149, 1987.

[74] J. W. Ross and D. J. Lam, *J. Appl. Phys.,* vol. 38, p. 1454, 1967.

[75] D. Mannix, G. H. Lander, J. Rebizant, R. Caciuffo, N. Bernhoeft, E. Lidström and C. Vettier, *Phys. Rev. B,* vol. 60, p. 15187, 1999.

[76] P. Santini and G. Amoretti, *Phys. Rev. Lett.,* vol. 85, p. 2188, 2000.

[77] P. Santini, S. Carretta, G. Amoretti, R. Caciuffo, N. Magnani and G. H. Lander, *Rev. Mod. Phys.,* vol. 81, p. 807, 2009.

[78] S. Di Matteo, N. Magnani, F. Wastin, J. Rebizant and R. Caciuffo, *J. Alloys Compounds,* vol. 444/445, p. 278, 2007.

[79] Y. Hiraoka, Y. Tanaka, Y. Kojima, Y. Takata, M. Oura, Y. Senba, H. Ohasbi, Y. Wakabayachi, S. Shin and T. Kimura, *Phys. Rev B,* vol. 84, p. 064418, 2011.

[80] S. W. Lovesey, A. Rodriguez-Fernandez and J. A. Blanco, *Phys.Rev.B,* vol. 83, no. 054427, 2011.

[81] F. de Bergivin and M. Brunel, *Acta. Crystallogr. Sect. A,* vol. 37, p. 324, 1981.

[82] M. C. Navarro, M. C. Lagarrigue, J. M. De Paoli, R. E. Carbonia and M. I. Gómez, *J. Therm Anal Calorim,* vol. 102, p. 655, 2010.

[83] J. Peng, M. Hojamberdiev, B. Cao, J. Wang and Y. Xu, *Appl Phys A,* vol. 103, p. 511, 2011.

[84] Y. Zheng, G. Tan, H. Miao, A. Xia and H. Ren, *Mattelials Letters,* vol. 65, p. 1137, 2011.

[85] R. Haumont, P. Bouvier, A. Pachkin, K. Rabia, S. Frank, B. Dkhil, W. A. Crichton, C. A. Kuntscher and J. Kreisel, *Phys. Rev. B,* vol. 79, p. 184110, 2009.

[86] R. Przenioslo, M. Regulski and I. Sosnowska, *J. Phys. Soc. Japan,* vol. 75, p. 084718, 2006.

[87] J. Fernandez-Rodriguez, S. W. Lovesey and J. A. Blanco, *Phys. Rev. B,* vol. 77, p. 094441, 2008.

[88] Y. Tanaka, T. Inami, S. W. Lovesey, K. S. Knight, F. Yakhou, D. Mannix, J. Kokubun, M. Kamauchi, K. Ishida, S. Nanao, i. T. Mala, H. Yamauchi, H. Onodera, O. K. and Y. Yamauchi, *Phys. Rev. B,* vol. 69, p. 024417, 2004.

[89] D. F. McMorrow, K. A. McEwen, U. Steigenberger, H. M. Ronnow and F. Yakhou, *Phys. Rev. Lett.,* vol. 87, p. 057201, 2001.

[90] S. Blundell, Magnetism in Condensed Matter, Oxford: Oxford University Press, 2001.

[91] R. M. White, Theory of Magnetism, Berlin: Springer, 2007.

[92] W. Eerenstein, N. D. Mathur and J. Scott, *Nature,* vol. 442, p. 759, 2006.

[93] S. W. Cheong and M. Mostovoy, *Nature Mater.,* vol. 6, p. 13, 2007.

[94] L. W. Matarrese and F. W. Stout, *Phys. Rev.,* vol. 94, p. 1792, 1954.

[95] E. Balcar and S. W. Lovesey, Introduction To The Graphical Theory Of Angular Momentum, Berlin: Springer, 2010.

[96] I. Marri and P. Carra, *Phys. Rev. B,* vol. 69, p. 113101, 2004.

[97] S. W. Lovesey and E. Balcar, *J. Phys.: Condens. Matter,* vol. 9, p. 8679, 1997.

[98] B. T. Thole, P. Carra, F. Sette and G. Van der Laan, *Phys. Rev. Lett,* vol. 68, p. 1943, 1992.

[99] I. B. Khriplovich, *Uspekhi,* vol. 40, p. 1161, 1997.

[100] S. Chandrasekhar, Radiative Transfer, New York: Dover Publications, 1960.

[101] P. J. Brown, J. B. Forsyth, E. Lelievre-Berna and F. Tasset, *J. Phys.: Condens. Matter,* vol. 14, p. 1957, 2002.

[102] M. Muto, Y. Tanabe, T. Iizuka-Sakano and E. Hanamura, *Phys. Rev. B,* vol. 57, p. 9586, 1998.

[103] F. W. Hehl, Y. N. Obukhov, J. P. Rivera and H. Schmid, *Eur. Phys. J. B,* vol. 71, p. 321, 2009.

[104] C. Görller-Walrand, K. Binnemans, K. A. Gschneidner and L. Eyring, Handbook on the Physics and Chemistry of Rare Earths, Amsterdam: North-Holland Publishers, 1998.

[105] R. D. Cowan, The Theory of Atomic Structure and Spectra, University of California Press: Berkeley, 1981.